
From Single DNA Molecules to an Entire Virus: an Investigation with Quantitative Fluorescence Microscopy and X-Ray Reflectivity

Marion Hochrein



München 2005

From Single DNA Molecules to an Entire Virus: an Investigation with Quantitative Fluorescence Microscopy and X-Ray Reflectivity

Marion Hochrein

Dissertation
im Department für Physik
der Ludwig-Maximilians-Universität
München

vorgelegt von
Marion Hochrein
aus München

München, den 16.09.2005

Erstgutachter: Prof. Dr. J. O. Rädler

Zweitgutachter: Prof. Dr. E. Frey

Tag der mündlichen Prüfung: 25.11.2005

Vielen Dank an ...

Prof. Dr. Joachim Rädler für die Möglichkeit, diese Doktorarbeit an seinem Lehrstuhl durchzuführen, die gute Betreuung und die große experimentelle Freiheit.

Dr. Bert Nickel für die Einführung in die Reflektivität, viele tolle Experimente am Desy und an der ESRF, seine Geduld beim Erklären und die produktive Zusammenarbeit am Membranenpaper.

Prof. Leonardo Golubovic thanks for the great and longlasting cooperation and the interesting theory to the DNA stretching experiments.

Dr. Lucienne Letellier thanks for the fruitful cooperation on the T5 phage ejection project.

Dr. Stephanie Mangenot thanks for the great time we had when we were doing experiments in the dark microscopy room and when cooking noodles ...

Christian Reich die tolle Zeit an den Synchrotrons, viel Spaß und super Experimente. Ich wünsche dir weiterhin Happy Lipids!

Dr. Christine Meyer für die super scharfen REM Bilder, die kein anderer so gut hingebraucht hat. Außerdem danke ich dir für die gemeinsamen Versuche einen idealen Master herzustellen. So habe ich einen Einblick in die Arbeitsmethoden am Halbleiterlehrstuhl erhalten.

Dr. Heribert Lorenz für die strukturierten Siliziumwafer.

Dr. Ulf Rädler dafür, dass du unermüdlich die strukturierte Folie an die Iridiumkammern geklebt hast. Vielen Dank auch dafür, dass du mir in der schweren Anfangsphase oft zur Hand gegangen bist.

Andreas Hohner für seine nette hilfsbereite Art. Es hat Spaß gemacht, mit dir Praktika zu überleben und das Büro zu teilen. Auf dich kann man sich verlassen. Vor allem wenn Igor hängt.

Johannes Bayer seine große Hilfsbereitschaft und seine ruhige Art und Weise. Es war sehr schön, ein sehr produktives letztes Jahr mit dir das Büro zu teilen.

Dr. Simon Keller die unzähligen Kästen Bier, die unvergeßliche Rossler-Erfahrung und die Einblicke ins isometrische Freeciv.

Stefan Beyer weil du mir den Einstieg erleichtert hast, indem wir zusammen an unmöglichen Experimenten herumversuchen konnten. Auch vielen Dank für die AFM Messungen im Reinraum.

Dr. Valentin Kahl für die Einführung in das DNA auf Lipid System.

Judith Leierseder die beste Werkstudentin auf der Welt.

Daniel Hönig und Alex Rapp , die zum Schluss mein Büro teilten, für eine sehr spaßige Zeit beim Zusammenschreiben. Das gemeinsame Joggen mit Daniel hat meine Fitness aufrechterhalten.

Martin Clausen fürs Korrekturlesen der Arbeit und ebenfalls fürs Joggen und fürs gemeinsame Kochen.

Gerlinde Schwake und Susanne Kempter für eine tolle Zeit und den aussichtslosen Kampf gegen das Chaos im Labor.

Madeleine Leisner fürs Korrekturlesen und den gemeinsamen Besuch der Fitnessgymnastik.

Luisa Ambruzzi, Jason DeRouchey, Angelika Hermann, Lana Polero, Kirstin Seidl für die nette Atmosphäre am Lehrstuhl.

Öscan Kaya für Schwarzwälderkirchtorten und McDonalds Menüs.

Andreas Gärtner dafür, dass du mich immer wieder aufgebaut hast, wenn meine Nerven blank lagen.

die Leute von E22 unter anderem für die prima Zeit auf den Winterschulen.

meine Eltern dafür, dass sie immer für mich da sind.

Contents

1	Summary	1
2	Introduction	5
3	The Ongoing Quest to Stretch DNA	9
3.1	Force Applied to the End of a DNA Molecule	10
3.2	Electrophoretic and Hydrodynamic Stretching	12
3.2.1	Tethered DNA in Uniform Flow	13
3.2.2	DNA in Shear Flow	13
3.2.3	2D Polymer in an Electric Field	14
3.3	Molecular Combing	14
3.4	Confinement Elongation	14
4	About Lipids and Membranes	17
4.1	Biomembranes	17
4.2	Lipids	18
4.3	Structural Models of Substrate Supported Membranes	20
5	Preparation Techniques and Experimental Methods	23
5.1	Materials and Preparation Techniques	23
5.2	Methods	27
5.2.1	Fluorescence Microscopy	27
5.2.2	Continuous Bleaching	28
5.2.3	Fluorescence Recovery After Photobleaching	29
5.2.4	X-ray Reflectivity	32
5.2.5	Atomic Force Microscopy	34
5.2.6	Scanning Electron Microscopy	35
6	Real-Time Imaging of DNA Ejection from Single Phage Particles	37
6.1	Introduction to T5 Phage	37
6.2	Setup	38
6.3	Response of the Ejected DNA to a Hydrodynamic Flow of Variable Strength	41

6.4	Phage Ejection Process	42
6.4.1	Stepwise Ejection	42
6.4.2	Length Distribution of the Ejected DNA	44
6.5	Discussion and Conclusion	46
6.6	Outlook	50
7	Structure and Fluidity of Lipid Membranes Supported on the Thermoplastic COC	53
7.1	Introduction	53
7.2	Results	54
7.2.1	Homogeneity and Fluidity of the Lipid Layers	54
7.2.2	Structure of the Lipid Layer	56
7.3	Discussion	60
7.3.1	Homogeneity and Fluidity	60
7.3.2	Structure	62
7.3.3	Details of the Bilayer Structure	62
7.3.4	Further Structural Lipid Membrane Models	66
7.3.5	Water Layer	67
7.4	Conclusion and Outlook	69
8	DNA Localization and Stretching on Periodically Microstructured Lipid Membranes	71
8.1	Introduction	71
8.2	Theory	73
8.3	Experimental Observations	76
8.3.1	Characterization of the Master and the Lipid Membrane	76
8.3.2	DNA Stretching	78
8.4	Conclusion and Outlook	85
9	The Future of Supported Lipid Membranes as a Tool for DNA Manipulation	89
9.1	Localization of DNA with Light Induced Surface Charges	89
9.2	Heat Fields	89

1 Summary

This PhD thesis presents a fluorescence microscopy study about deoxyribose nucleic acid (DNA) in confined geometries. DNA serves as an established model polymer well described by polymer physics. In a first project, the dynamics of the DNA ejection through the tight viral shaft from the highly packed phage capsid was investigated. In a second project DNA was manipulated by linear substrate structures.

During phage assembly the phage DNA is very tightly packaged into the phage capsid. The question arises if the internal pressure resulting from the high DNA density inside the capsid is responsible for the complete or at least the partial DNA transfer into the host during infection. This was studied for the first time on single T5 phages whose DNA release can be triggered by the receptor protein FhuA *in vitro*. After T5 phages had adsorbed onto a microfluidic chamber, the ejected DNA was fluorescently stained and stretched in a hydrodynamic flow. The length could thereby be measured continuously. With this setup, we succeeded for the first time in visualizing the dynamics of the DNA ejection in real time. The DNA release is not an all-or-none process but occurs in a stepwise fashion and at a rate reaching 75 000 bp/s. The pauses in between steps can last for over half an hour. The length distribution of the ejected DNA was analyzed and characteristic peaks were found at positions that coincided with the position of single-stranded interruptions (nicks) of the phage genome.

DNA molecules adsorbed onto cationic fluid lipid membranes remain laterally diffusive. During this thesis rectangular grooves of a periodicity of 1000–1200 nm and a depth of 40–120 nm were imprinted into the thermoplastic “cyclic olefin copolymer” (COC). This substrate was coated with a lipid membrane. The influence of such a support on the conformational behavior of DNA is investigated here. The periodically structured membranes revealed the ability to stretch long DNA molecules. During a collaboration, L. Golubovic provided us with a theory explaining the observed process. The DNA stretching phenomenon can be elucidated in terms of a curvature dependent potential energy attained by the adsorbed DNA molecules.

The properties of lipid membranes supported by the hydrophobic solid polymer COC are investigated. Lipid layers were prepared by vesicle fusion and solvent exchange from varying amounts of 1,2-Dioleoyl-3-Trimethylammonium-Propane (DOTAP, cationic) and 1,2-Dioleoyl-sn-Glycero-3-Phosphocholine (DOPC, neutral). The influence of the membrane charge and also of the preparation method were investigated. All lipid mixtures

coated the COC surface homogeneously forming a fluid membrane as verified by quantitative fluorescence microscopy, the method of Continuous Bleaching and Fluorescence Recovery After Photobleaching (FRAP). The average diffusion constant was found to be $0.8 \mu\text{m}^2/\text{s}$ which is higher by a factor of 5 than the typical membrane diffusion constant for hydrophilic supports. The vertical electron density profile of the supported membranes was determined by synchrotron reflectivity experiments using a special microfluidic chamber adapted to reflectivity experiments. The x-ray data can not be fitted as expected with a model assuming a monolayer. They are however in agreement with a compressed and less densely packed bilayer. The head-to-head distance is 29 \AA , the density of the headgroups is $\rho_h = 0.34 \text{ e}^-/\text{\AA}^3$ and of the tails $\rho_t = 0.26 \text{ e}^-/\text{\AA}^3$.

Zusammenfassung

Im Rahmen dieser Doktorarbeit wurde Desoxyribonukleinsäure (DNA) in einschränkenden Geometrien mit Hilfe von Fluoreszenzmikroskopie untersucht. DNA diente dabei als bekanntes Modellpolymer, das gut mit Hilfe der Polymerphysik beschrieben werden kann. Zum einen wurde die Dynamik des DNA-Austritts aus dem vollgepackten Phagencapsids durch den engen Virusschaft untersucht und zum anderen wurden DNA-Stränge durch linienförmigen Substratstrukturen manipuliert.

Während des Phagenzusammenbaus wird die Phagen-DNA sehr dicht in das Phagencapsid gepackt. In dieser Arbeit wurde die Frage untersucht, ob der interne Druck, den die hohe DNA Dichte innerhalb des Capsids verursacht, dafür verantwortlich ist, dass die DNA ganz oder zumindest teilweise während der Infektion in den Wirt transferiert wird. Dies wurde an einzelnen T5 Phagen untersucht, deren DNA Freisetzung man durch die Zugabe des Rezeptorproteins FhuA *in vitro* auslösen kann. Nachdem T5 Phagen auf dem Boden einer Mikrofluidikkammer adsorbiert hatten, wurde die freigesetzte DNA mit Fluoreszenzfarbstoff markiert und im hydrodynamischen Fluß gestreckt. Dadurch konnte die DNA-Länge kontinuierlich gemessen werden. Mit dieser Vorgehensweise gelang es zum ersten Mal die Dynamik der DNA Freisetzung sichtbar zu machen. Diese findet nicht in einem kontinuierlichen Prozess statt, sondern erfolgt schubweise mit Pausen, die über eine halbe Stunde dauern können. Die Austrittsgeschwindigkeit beträgt mindestens 75 000 bp/s. Die Längenverteilung der freigesetzten DNA wurde analysiert und dabei wurden charakteristische Maxima bei Längen gefunden, die gut mit der Position von einzelsträngigen Fehlstellen in der Phagen-DNA, sogenannten Nicks übereinstimmen.

DNA-Moleküle, die auf planaren kationischen fluiden Lipidmembranen adsorbiert sind, bleiben lateral beweglich. In dieser Arbeit wurden Gräben mit einem Rechteckprofil einer Periodizität von 1000–1200 nm und einer Tiefe von 40–120 nm in das Kunststoffmaterial “Cycloolefin-Copolymer” (COC) gepresst. Dieses Substrat wurde mit einer Lipidmembran beschichtet. Die zentrale Fragestellung ist, wie die Konformation von DNA, die auf solchen Lipidmembranen adsorbiert ist, beeinflusst wird. Die periodisch strukturierten Membranen zeigten die Fähigkeit, lange DNA-Moleküle zu strecken. Im Rahmen einer Zusammenarbeit wurde von L. Golubovic eine Theorie erarbeitet, die diesen Vorgang erklärt. Darin kann die DNA-Streckung mit Hilfe einer krümmungsabhängigen potentiellen Energie der DNA erklärt werden.

Weiterhin wurden die Eigenschaften von substratgestützten Lipidmembranen untersucht, die den Thermoplasten COC als Trägermaterial hatten. Dabei wurden die Lipidmembranen aus verschiedenen Anteilen von 1,2-Dioleoyl-3-Trimethylammonium-Propan (DOTAP, einfach positiv geladen) und 1,2-Dioleoyl-sn-Glycero-3-Phosphocholin (DOPC, neutral) entweder mit Vesikelfusion oder mit einem Lösungsmittelaustauschverfahren hergestellt. Sowohl der Einfluß der Ladung als auch der Präparationsmethode auf die Eigenschaften der Membran wurden untersucht. Dabei zeigte sich, dass alle Lipidmischungen die COC Oberfläche homogen bedeckten und eine fluide Membran bildeten, wie mit quantitativer Fluoreszenzmikroskopie, der Methode des kontinuierlichen Fluoreszenzbleichens (Continuous Bleaching) und Fluoreszenzerholung nach Photobleichen (FRAP) bestätigt werden konnte. Die durchschnittliche Diffusionskonstante lag bei $0.8 \mu\text{m}^2/\text{s}$, was einen Faktor 5 unter der typischen Diffusionskonstante von Membranen auf hydrophilen Trägermaterialien liegt. Das vertikale Elektronendichteprofil der substratgestützten Membran wurde mit Reflektivitätsexperimenten mit Synchrotronstrahlung unter Verwendung einer für Reflektivitätsmessungen neu entwickelten Mikrofluidikkammer vermessen. Die Röntgendaten konnten nicht wie erwartet mit einem Modell erklärt werden, dass von einer Lipideinzelschicht ausgeht, sondern nur mit einem Modell einer Lipiddoppelschicht. Diese Lipiddoppelschicht ist deutlich dünner und weniger dicht gepackt, als man dies für Membranen im freien Volumen beobachtet. Die Kopf-zu-Kopf Distanz beträgt $d_{hh} = 29 \text{ \AA}$, die Dichte der Kopfgruppen $\rho_h = 0.34 \text{ e}^-/\text{\AA}^3$ und die der Schwanzgruppen $\rho_t = 0.26 \text{ e}^-/\text{\AA}^3$.

2 Introduction

A virus that infects only bacteria is called bacteriophage or simply phage. The name phage stems from Greek phageton = food/consumption. Phages play an important role in molecular biology as cloning vectors to insert deoxyribose nucleic acid (DNA) into bacteria. DNA contains the genetic instructions specifying the biological development of all cellular forms of life and many viruses. DNA is often referred to as the molecule of heredity, as it is responsible for the genetic propagation of most inherited traits. Inserting specific DNA into cells will therefore lead to desired traits of the cells. Additionally, phage therapy has been used as an alternative to antibiotics for treating bacterial infections in the former Soviet Union because phages are highly efficient at killing bacteria. The development of bacterial strains that are resistant to multiple drugs has also led western medical researchers to re-evaluate phages as alternatives to the use of antibiotics. Additionally, some phages seem to be related to human viruses e.g. the phage PRD1 shares a common ancestor with the human adenovirus [1]. Therefore understanding phages will improve our knowledge about human viruses which is in return helpful for developing effective anti-viral medicine. Like many viruses that infect eukaryotes, phages consist of an outer protein hull and the enclosed genetic material which consists of double-stranded DNA in 95% of the phages known. In many bacteriophages, DNA is highly compressed (e.g. phage T7: 450 mg/ml [2]) triggering the ongoing discussion on how and why DNA is arranged at such high packing densities [2, 3, 4, 5, 6, 7]. A hypothesis as to why phages pack their DNA so tightly is that the pressure resulting from the tight packing (~ 50 atm [8]) supplies the energy necessary for the DNA to cross the bacterial cell membrane [9, 10, 11]. In this study, the ejection process of single T5 phage particles is observed in vitro in real time. This allows us to resolve details of the infective process which are not accessible to bulk investigations. Fluorescence microscopy is well suited as a fast and non-invasive technique to observe this process. To resolve the length of the ejected DNA, a fluid flow was applied to stretch it out of its native coiled state.

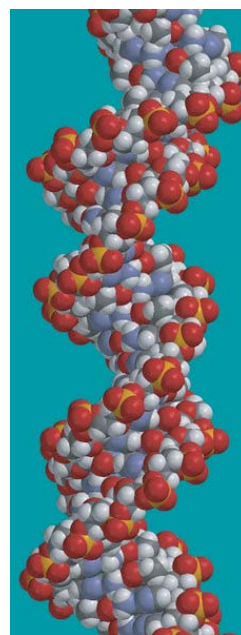


Figure 2.1: DNA

During the T5 phage experiments, stretching DNA was used primarily as a means to visualize the length of the ejected DNA, but stretching DNA is a very interesting topic

in itself. This has been indeed a subject of continuing research (s. chapter 3) for various reasons. The length of DNA can be quite large: a typical human chromosomal DNA strand is a couple of centimeters long. Such long DNA is always coiled and intertwined because of the entropic advantage of such conformations. For most biotechnological applications DNA has to be unfolded since only the uncoiled state allows the correct observation and manipulation of DNA. Additionally, stretching DNA enables us to learn about the mechanical properties of DNA such as its stretching modulus. The mechanical properties of DNA are very important for understanding the physics behind biological processes involving DNA. In typical experiments, DNA is attached with one end to a surface while the other end is pulled [12, 13, 14]. Another common approach to stretch DNA is to use electrostatic or hydrodynamic flow fields [15, 16, 17, 18]. In this work, a novel method to align DNA is presented which is very suitable for potential biotechnological applications. The idea originated from previous work: Cationic lipid DNA complexes form a lamellar structure of alternating lipid membranes and DNA smectic monolayers [19]. The origin of this DNA alignment is thought to originate from a 1-D sinusoidal curvature modulation of the lipid membranes. The DNA is situated within the membrane grooves thereby forming parallel strands [20]. The idea is to reduce this system to 2-D: a supported cationic lipid membrane with adsorbed DNA molecules. The surface curvature of such a supported membrane translates to a resulting attractive or repulsive potential for DNA. The membrane curvature can be achieved by fabricating a grid of parallel grooves on the support of a lipid layer. The surface topography produces attractive and repulsive lines which are shown to orient the DNA molecules similar to the process seen in 3-D. Supported membranes are easily further biofunctionalized [21, 22], thus allowing the use of this system for a broad range of applications, e.g. DNA chips for fast testing of genetic diseases. Standard supports such as mica, glass slides or silicon wafers can be topologically structured, but this requires clean room equipment and it is time consuming. Therefore a simpler method such as imprinting a master into a plastic material would be more desirable. The thermoplastic cyclic olefin copolymer (COC) is ideal for our purposes because its good optical properties [23] allow for the use of high resolution fluorescence microscopy. A theory was developed to describe quantitatively how the DNA stretching process is achieved and how it depends on the charge density of the lipid layer. Finally, the theoretical predictions are compared to the experimental results.

Until now, to the best of our knowledge, COC has not been characterized as a support for lipid membranes. The properties of the lipid membrane are, of course, of central importance for the DNA stretching experiments and were therefore investigated in this study. However, supported membranes constitute a very interesting field of research by itself. Supported membranes represent an important model system for cell membranes and they promise to be useful for the biofunctionalization of surfaces [24] which is in turn very important for biophysical applications [25]. Very few investigations aimed at directly resolving the structure of single lipid layers supported on hydrophilic substrates

[26, 27, 28, 29, 30, 31]. Typically, supported lipid layers are often only characterized optically, e.g. with fluorescence microscopy or with fluorescence recovery after photobleaching which yields the lateral diffusion constant of the lipid molecules [32]. Similarly, only a few investigations of supported lipid membranes on hydrophobic substrates were performed and these did not resolve the structure directly [33, 34, 35]. In this thesis it is shown that on hydrophobic COC surfaces lipid layers are organized as thin, loosely packed bilayers. For the first time, optical methods were combined with x-ray reflectivity measurements to characterize charged and neutral lipid membranes supported on COC.

This thesis is structured in the following way: Chapter 3 and 4 were written to give the reader an introduction and overview about the continuing efforts to stretch DNA, and about biomembranes and their constituents, the lipid molecules. The third chapter is dedicated to explain how the samples were prepared and to illustrate the principles of the methods used to characterize them. The next three chapters describe the three different experimental systems studied here: Chapter 6 examines the ejection process of the T5 phage. Chapter 7 reports on the properties of lipid membranes supported on the thermoplastic COC. Chapter 8 describes the study of the conformational behavior of DNA molecules adsorbed on cationic lipid membranes that are supported on grooved, periodic micro-structured surfaces. Finally, a short outlook proposes interesting future experiments.

3 The Ongoing Quest to Stretch DNA

DNA is usually organized as two complementary strands, which are held together by hydrogen bonds. Both strands of double stranded DNA (dsDNA) are intertwined to form a double helix, see Fig. 2.1. Such a structural conformation is called B-DNA, which is the natural conformation of DNA. Only very few DNA molecules are not paired in a natural biological environment and form single stranded DNA (ssDNA). A single strand is built from a polyester chain made up of alternating sugar (D-2-deoxyribose) and phosphate groups. A single sugar and phosphate group is called base. The four possible bases are adenine (A), thymine (T), cytosine (C), and guanine (G). Each base “pairs up” with only one other base: A+T and C+G. Therefore the second strand of the double helix DNA is complementary to the first. The specific pairing of the bases is the reason for the unique ability of DNA to replicate itself. The sequence of the different nucleotides translates into a sequence of amino acids which are the building blocks of proteins [36].

In the recent years, a great number of different approaches have been tried to unfold genomic-sized DNA which is naturally coiled and therefore inaccessible for biotechnological and research methods. For many biotechnological applications such as optical DNA restriction mapping and sequencing it is necessary to extend the polymer such that a one-to-one mapping can be established between the spatial position along the polymer and the position within the genome [37, 38, 39, 40, 41]. Additionally, it is very difficult to analyze dynamic processes such as the very complex DNA protein interactions if the DNA is folded. Besides, the question how DNA reacts to external forces and restrictions is of essential interest for polymer theorists. Until now, four different approaches to stretch DNA have been applied:

- A mechanical force may be applied to one or both ends of the molecule which leads to a constant force acting on each segment of the molecule.
- Electrophoretic and hydrodynamic flow can lead to DNA stretching even though the force applied to a segment depends critically on the position within the molecule.
- Molecular combing immobilizes stretched DNA molecules on a surface by the viscous drag of a receding water surface.
- Confinement elongation: DNA is confined within channels whose dimensions are much smaller than the contour length of the DNA.

3.1 Force Applied to the End of a DNA Molecule

The following techniques may be used to measure force-extension curves of single DNA molecules [42]:

- Optical Tweezers: They allow to apply forces between 0.1 pN and 100 pN.
- Glass Microneedles: The force can be as small as 1 pN and as large as desired.
- AFM: The force ranges between 5 pN and a few nN.
- Magnetic Tweezers: They offer a force range between 0.01 pN and 100 pN.

Which technique is chosen depends on the force range and time resolution needed.

For a physicist, DNA is seen as a heteropolymer whose mechanical behavior can be described by different polymer theories. The genetic information stored in DNA is often not of interest. The details of the molecular structure are neglected and DNA is viewed as a charged cylinder with a diameter of 2.2 nm. Among others, the following models have been developed to describe a polymer reacting to external forces:

- Freely-Jointed Chain Model
- Worm-Like Chain Model
- extensible Worm-Like Chain Model

The freely-jointed chain (FJC) model treats the polymer as a chain of statistically independent segments of length b (Kuhn length) joined together at the ends. Their orientations are uncorrelated in the absence of external forces. A force F acting on the free end of a molecule whose other end is attached to a fixed point stretches the polymer as each segment tends to align with the force. The external force is opposed by the thermal agitation of the polymer which tends to disorder the segments. Therefore the elastic response of the molecule with contour length L_0 is purely entropic and the length of the polymer along the direction of the force (L_z) is given by [12]:

$$L_z = L_0 \left(\coth \left(\frac{Fb}{k_B T} \right) - \frac{Fb}{k_B T} \right). \quad (3.1)$$

Smith et al. [12] pulled on dsDNA attached with one end to a glass surface and with the other end to a magnetic bead. Remarkably, they showed that the FJC model failed to account for their experimental data over the entire force range (0.01 – 30 pN).

Later theoretical analysis showed that the DNA molecule could be described as an elastic tube subjected to thermal fluctuations [43]. Its extension is obtained as a balance between the entropy of the molecule and the work of the stretching force. This description, known as the worm-like chain (WLC) model, first introduced by Kratky and Porod [44], turns out to provide an excellent approximation of the elasticity of DNA at forces smaller than ~ 15 pN. The WLC model assumes an elastic chain with persistence length ζ_p and a bending energy per length $E_b = k_B T \zeta_p C^2 / 2$, where k_B is the Boltzmann constant, T the temperature, and C the local curvature. The following interpolation formula describes the relation between the applied force F and the extension along the axis of the force (z-axis) L_z [43, 45]:

$$F \frac{\zeta_p}{k_B T} = \frac{L_z}{L_0} + \frac{1}{4(1 - L_z/L_0)^2} - \frac{1}{4}. \quad (3.2)$$

However at larger forces ($F > 15$ pN), the DNA molecule no longer responds to the stress by reducing its entropy but by modifying its molecular structure. Near full extension, L_z approaches L_0 as $F^{-1/2}$ [45]. In this regime DNA can also be enthalpically stretched beyond the contour length defined by B-DNA geometry [13]. An equation that describes this extensible WLC regime well is

$$\frac{L_z}{L_0} = 1 - \frac{1}{2} \left(\frac{k_B T}{F \zeta_p} \right)^{1/2} + \frac{F}{S}, \quad (3.3)$$

where S is the elastic stretch modulus [46]. The dependence of the persistence length ζ_p and the stretch modulus S on salt conditions was investigated by Baumann et al. [47]. For monovalent salt, ζ_p decreases with increasing salt concentration while S increases. An interpolation formula for an extensible WLC for the complete force range from 0 – 50 pN was found by Wang et al. [48]:

$$\frac{F \zeta_p}{k_B T} = \frac{L_z}{L_0} + \frac{1}{4(1 - L_z/L_0 + F/S)^2} - \frac{1}{4} - F/S. \quad (3.4)$$

Smith et al. [13] and Cluzel et al. [14] measured the force-displacement response of a single dsDNA molecule up to higher forces. When the force reaches 65 – 70 pN, a structural transition to a new DNA phase, called S-DNA, is observed. At this force, the molecule overstretches abruptly to 1.7 times of its original contour length. The change in length takes place over a very narrow force range (~ 2 pN) which indicates that this transition is highly cooperative. The transition force is dependent on the base pairs used [49] and on the pH of the solution [50]. At a force of 150 pN the dsDNA melts, leading to another plateau in the force curve [49]. The force at which the melting transition occurs depends on the pulling speed indicating that the transition does not take place

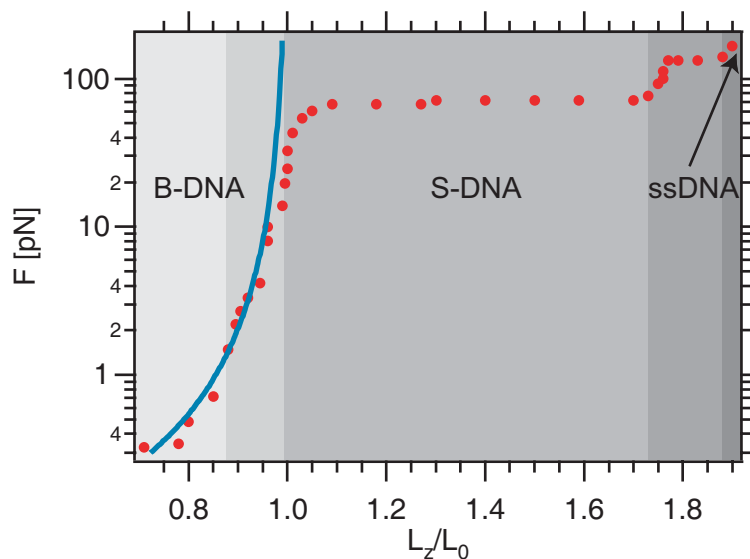


Figure 3.1: Force versus relative extension of dsDNA: Data points are taken from [51] and are shown as red dots. The different regimes are displayed in different shades of grey: The entropic elasticity regime (light grey) is followed by the intrinsic elasticity regime (slightly darker grey). At ~ 70 pN the DNA makes a transition to S-DNA (grey). At ~ 150 pN the dsDNA melts (dark grey) and the curve coincides with that of ssDNA (very dark grey). The curve resulting from the WLC model (s. Eq. 3.2) assuming $\zeta_p = 50$ nm is shown in blue.

in equilibrium. After this transition the force extension curve coincides with that of ssDNA.

Recapitulating, at least five different regimes can be distinguished in the dsDNA force-extension curve (s. Fig. 3.1). At low forces (up to ~ 15 pN) entropic forces dominate (“entropic elasticity regime”). After that, DNA starts to stretch linearly with F , this “intrinsic elasticity regime” is followed by the transition from the B-type DNA to S-DNA which occurs at $65 - 70$ pN (“overstretching transition”). The DNA may stretch up to $1.7 \times$ its contour length L . At around 150 pN the dsDNA denatures (“melting transition”) and starts to follow the force extension curve of ssDNA.

3.2 Electrophoretic and Hydrodynamic Stretching

Under biotechnological and experimental conditions a DNA molecule will rarely be exposed to a force exerted to its ends but it will be subjected to divers hydrodynamic flows and electric fields, e.g. during electrophoresis. Such realistic scenarios are more complicated to understand. For example, a major difficulty in theoretical descriptions of polymer chain dynamics is the hydrodynamic coupling within the chain - the motion

of one part of the chain perturbs the surrounding flow and modifies the hydrodynamic force exerted on another part. Electric fields in aqueous solutions almost always lead to electroosmosis and therefore both hydrodynamic and electric interactions have to be taken into account. Because of the diversity of interactions of DNA with hydrodynamic and electric fields, this overview will be restricted to a few interesting cases.

3.2.1 Tethered DNA in Uniform Flow

Perkins et al. [15] optically trapped a microsphere attached to one end of a DNA molecule while the other end remained free. A uniform (nonshearing) fluid flow was achieved by translating the fluid chamber and therefore also the fluid horizontally with a velocity v while the bead remained stationary. Here, the applied force is zero at the free end and maximal at the attached end. The fractional extension L_z/L_0 is a function of $\eta v L_0^{0.54}$. η is the fluid viscosity. Surprisingly, over a large extension range (20% to 80%) the relatively simple WLC model (s. Eq. 3.2) coincides with the data very well.

3.2.2 DNA in Shear Flow

The dynamics of flexible polymers in shear flow is of great practical interest because this type of flow occurs whenever a fluid flows past a surface. Smith et al. [16] investigated the behavior of DNA molecules under steady shear flow ($dv/dy = \gamma = \text{const}$, where y indicates the direction perpendicular to the surface and v is the velocity of the flow). Their data show that even at relatively low shear rates there are large fluctuations in the extension of the molecule. As the shear rate γ is increased the molecules fluctuate more rapidly and reach larger extensions. The mean fraction extension $\langle L_z \rangle / L_0$ increases gradually with the shear rate and approaches an asymptotic value of $L_z/L_0 \sim 0.4$ to 0.5 .

Doyle et al. [17] observed the dynamics of a single polymer tethered to a planar solid surface in a shear flow using fluorescently labeled DNA chains. Shearing a tethered chain gives rise to large temporal fluctuations in the chain extension. Simulations revealed that these fluctuations are due to a continuous recirculating motion of the chain. This cyclic dynamics was caused by a coupling of the flow field gradient with thermally driven fluctuations of the chain in the shear gradient direction. Ladoux et al. [18] showed that the tethered chains approach full extension as the flow rate was increased very slowly. Assuming a WLC, the shear rate γ is related to the relative extension L_z/L_0 :

$$1 - L_z/L_0 \sim \gamma^{-1/3}, \quad (3.5)$$

for L_z approaching the contour length L_0 . Such asymptotic behavior was indeed observed experimentally.

3.2.3 2D Polymer in an Electric Field

B. Maier et al. [52] investigated the elastic response of single DNA molecules to an external electric field in two dimensions. The DNA is tethered at one end to a bead and it is restricted to movements within the 2-D plane of a cationic membrane. The end-to-end distance in the strong stretching limit ($\nu E \zeta_p > k_B T$) elongates with increasing field strength in good agreement with the worm-like chain model adapted to 2D:

$$L_z \approx 1 - \frac{1}{\sqrt{\frac{4\nu E \zeta_p L_0}{k_B T}}}, \quad (3.6)$$

where ν is the effective line charge density of the DNA molecule (here: $\nu = 0.6 \pm 0.1 \text{ e}^-/\text{nm}$) and E the electric field strength.

3.3 Molecular Combing

In a process called “molecular combing” [53, 54], DNA molecules attached at one end to a solid surface were extended and aligned by a receding air-water interface and left to dry on the surface. In contrast to viscous drag and electrophoresis which act on the full length of the molecule, the action of the receding interface appears to be localized at the air-water interface and is thus independent of the length and conformation of the molecule. The combed molecules are lying flat in a linearized state on a dry solid substrate, they are observable with fluorescence even several months after combing, and are available for further manipulation. The force acting on the DNA molecule in the vicinity of the contact line can be estimated by using Hooke’s law. It depends strongly on the surface used to attach the DNA. For silanated surfaces the force amounts to $F = 160 \text{ pN}$. This technique has been modified to serve different applications and needs [55].

3.4 Confinement Elongation

Genomic-sized DNA molecules are trapped inside channels whose width d equals its depth. If d is much less than the radius of gyration of the unconfined polymer, the extension along the channel L_z scales linearly with the contour length L_0 of the polymer. This effect is called confinement elongation [56]. Confinement elongation does not require the presence of a known external force because a molecule in a nanochannel will remain stretched in its equilibrium configuration, and hence, the mechanism is in equilibrium.

Self avoidance effectively divides the confined polymer into a series of noninterpenetrating blobs, distributing the polymer mass along the channel in such a way that the monomer density is uniform. Consequently the extension of the polymer in the channel L_z must scale linearly with the contour length L_0 [57]:

$$L_z \simeq L_0 \frac{(\zeta_p w)^{1/3}}{d^{2/3}}, \quad (3.7)$$

where w is the width of the polymer (here 2 nm) and ζ_p the persistence length (50 nm). Once the channel dimensions drop below the persistence length, the de Gennes approximation fails and the following approximation of Odijk has to be considered [58, 59, 60]:

$$L_z = L \left[1 - 0.361 \left(\frac{d}{\zeta_p} \right)^{2/3} \right]. \quad (3.8)$$

With a channel of width of 100 nm and depth of 200 nm, λ -phage DNA can be stretched to 8 μm length which amounts to a relative extension of $L_z/L_0 = 36\%$ [56]. This ratio is improved to 71% if nanochannels of dimension 30×40 nm are used [60]. A simplified approach to fabricate nanofluidic channels with well-controlled dimensions was reported by Guo et al. [61]. In $120 \text{ nm} \times 75 \text{ nm}$ channels they observed that T5 DNA was stretched to 90% - 100% of its contour length.

4 About Lipids and Membranes

4.1 Biomembranes

Life as we know it is only possible because nature has invented membranes. Membranes enable the separation of living entities from the lifeless and possibly hostile environment while preserving a selective material exchange between the two worlds. Additionally, the function of cells, the basic unit of life, depends on the controlled interplay between compartments performing different functions. Therefore, membranes are used to divide the cell into compartments which are specialized for certain well defined functions. Simultaneously, the biomembranes themselves developed into sites of essential biochemical functions, such as protein biosynthesis or oxidative phosphorylation. Therefore the intracellular space is divided into two sub-spaces: the lumina of the various organelles and the cytosol. For example, different ionic compositions and pHs can be established in the lumina of the various organelles essential for varying purposes. Membranes differ in molecular composition and architecture according to the function of the compartment they are enveloping. For example, the cell membrane (plasma membrane) of animal cells is in general a three layered compound system (see Fig. 4.1). Its center is formed by a

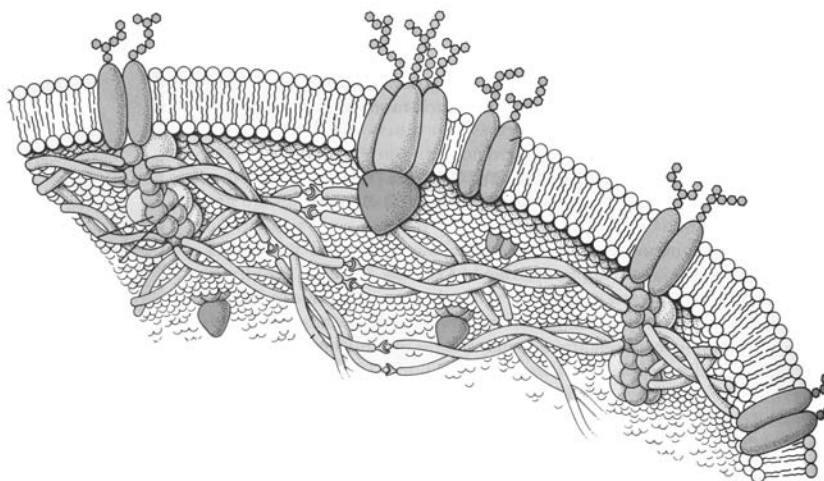


Figure 4.1: Schematic illustration of a typical plasma membrane, in this case an erythrocyte membrane. Image taken from [62].

lipid/protein layer. The extracellular side is covered by the glycocalyx: a film formed

by the oligosaccharides protruding from glycolipids or proteins. At the intracellular side the membrane is coupled to the cytoskeleton, a stabilizing protein complex [63]. The fundamental component of all biomembranes is the lipid bilayer, which consists of two monolayers of lipids facing each other. Proteins are embedded into the fluid, i.e. freely diffusive lipid matrix [64].

4.2 Lipids

The term lipid comprises a diverse range of molecules such as fatty-acid derived phospholipids, sphingolipids, glycolipids and terpenoids, such as retinoids and steroids. Membrane lipids consist of a polar, hydrophilic headgroup and nonpolar, hydrophobic tails. This amphiphilic nature of lipids is responsible for their self assembly properties. The hydrophobic tails tend to be packed together away from the water surrounding while lipid heads face towards it. Therefore, lipids will aggregate in aqueous environments if a certain lipid concentration called critical micelle concentration is exceeded. Among a variety of structures lipids may form micelles, vesicles or bilayer structures depending on the exact size relation of the hydrophobic to the hydrophilic part of the lipid. Cone-shaped molecules tend to form micelles while cylindrical molecules prefer to form bilayers. A bilayer consists of two monolayers of lipids where the hydrophobic tails face each other and the hydrophilic heads shield them from the surrounding water. This structure is also called a membrane and is the fundamental structure of biomembranes. Multiple membranes stacked on top of each other and separated by thin water layers are referred to as the lamellar or multilamellar phase.

Phospholipids or, more precisely, glycerophospholipids, are built on a glycerol core to which two fatty acid-derived “tails” are linked by ester linkages and one “head” group by a phosphate ester linkage. Fatty acids are unbranched hydrocarbon chains, connected by single bonds alone (saturated fatty acids) or by both single and double bonds (unsaturated fatty acids). The chains are usually 10-24 carbon groups long. Common fatty acid chain residues are myristoyl which has 14 carbon groups and no double bond (14:0), palmitoyl (16:0), and oleoyl (18:1). Typical head groups of phospholipids found in biological membranes are phosphatidylcholine (lecithin, PC), phosphatidylethanolamine (PE), phosphatidylserine (PS) and phosphatidylinositol (PI), whose head group can be modified by the addition of one to three more phosphate groups. The short name for the most common phospholipids is composed of two letters indicating the two fatty acid chains and two or three letters indicating the head group. For example, POPE stands for Palmitoyl-Oleoyl-PhosphatidylEthanolamine. DOPC indicates two (Double) chains of Oleoyl with a PhosphatidylCholine head. While phospholipids are the major component of biological membranes, other lipid components like sphingolipids and sterols (such as cholesterol in animal cell membranes) are also found in biological membranes.

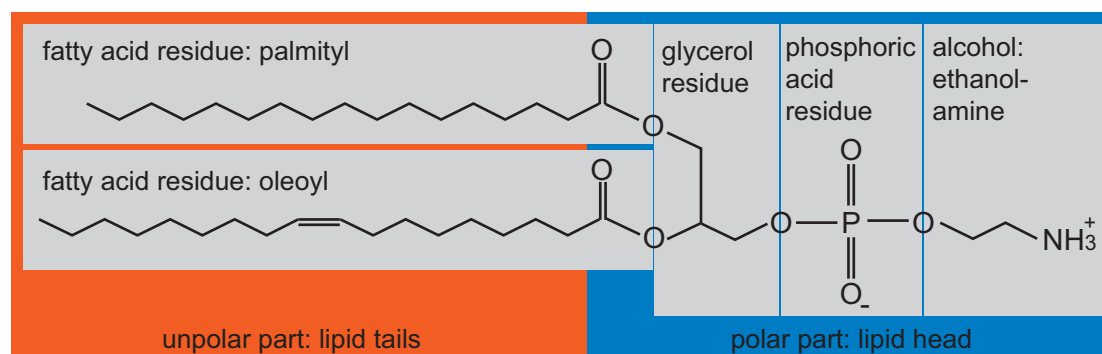


Figure 4.2: Structure formula of the phosphoglycerollipid POPE. The two fatty acids (here palmitoyl and oleoyl) are esterified to the hydroxyl groups of the glycerol backbone. The phosphate group is attached to the glycerol backbone by an ester link. This group is finally linked to an alcohol, such as ethanolamine (shown here) or inositol, serine or choline.

A lipid bilayer can undergo multiple phase transitions upon heating. The chain-melting transition or the gel to liquid crystalline phase transition is accompanied by the largest entropy change. The bilayer changes from the gel phase to the liquid-crystalline phase (L_α) (s. Fig. 4.3 (a)) at the main transition temperature (T_m). The gel phase comprises

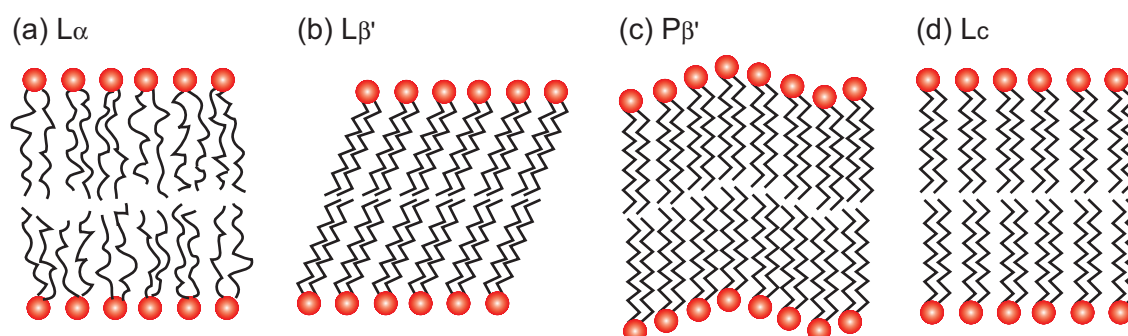


Figure 4.3: Different lipid bilayer phases: (a) L_α phase, the bilayer is fluid and the lipid chains are unordered. (b) $L_{\beta'}$ phase, the bilayer is in the ordered gel phase, the chain orientation is tilted with respect to the membrane normal. (c) The ripple phase ($P_{\beta'}$). The membrane shows a saw tooth like height variation. (d) The liquid-crystalline phase: the lipids are immobile and ordered.

among others the L_C (lamellar crystalline), $L_{\beta'}$ (tilted gel), and finally the $P_{\beta'}$ (ripple gel) phase (s. Fig. 4.3). In the gel phase, the long tilted acyl chains of the lipid adopt an all-trans conformation and are packed together closely. At the main transition temperature, the tight packing becomes loosened which can be attributed basically to a trans-gauche isomerization of carbon-carbon single bonds along the acyl chain [65]. The liquid-crystalline phase is also called the fluid phase because the molecules can diffuse

freely within the bilayer. The corresponding diffusion coefficients usually are between $1 - 10 \mu\text{m}^2/\text{s}$.

4.3 Structural Models of Substrate Supported Membranes

Lipids can interact in several ways with surfaces [s. Fig. 4.4]. If the substrate is too rough or chemically heterogeneous, no lipid adsorption is expected [33]. For hydrophilic

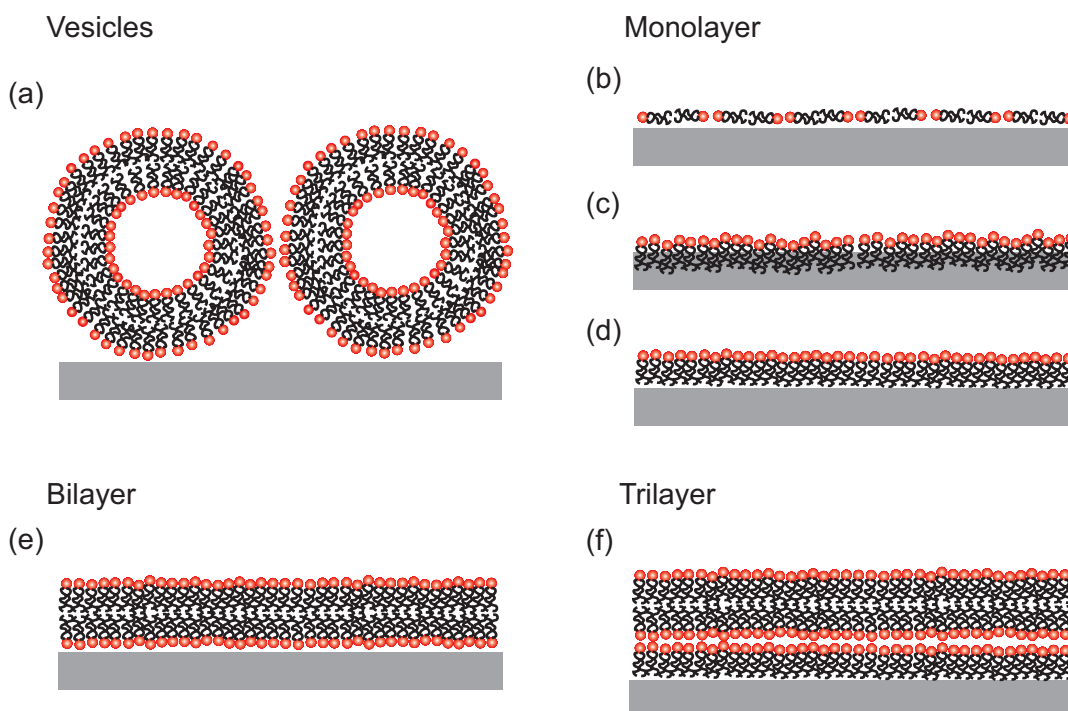


Figure 4.4: Coating Possibilities: Schematic drawing of how the lipids might coat the COC surface: (a) lipid vesicles attached to the surface (b) monolayer with the lipids laying flat on the substrate (c) monolayer with the lipid tails inserted into the substrate (d) monolayer with the tails facing towards the surface (e) lipid bilayer (f) trilayer: a bilayer is firmly attached to a lipid monolayer on COC.

surfaces, either vesicles may attach [Fig. 4.4 (a)] or if the interactions are well tuned, a lipid bilayer may form [Fig. 4.4 (e)]. On hydrophobic surfaces, such as hydrocarbon terminated surfaces, the existence of lipid monolayers has been reported [66]. As shown in Fig. 4.4 (b) a monolayer might consist of lipids laying flat on the hydrophobic substrate thus increasing the length of hydrocarbon chain interaction with the surface. Depending on the polymer density the lipid chains could be fully or partially inserted into the

support [Fig. 4.4 (c)] or stay above the surface [Fig. 4.4 (d)]. A third alternative is the formation of multilayers, consisting of a mono- or bilayer directly adsorbed onto the surface and many bilayers stacked onto the first layer. Such formations are usually called oriented membrane stacks [67] as opposed to randomly oriented bilayer stacks forming if DOPC is hydrated in water [68]. A simple example of such multilayers is a trilayer, consisting of a monolayer attached to the surface and a bilayer stacked onto it [Fig. 4.4 (f)].

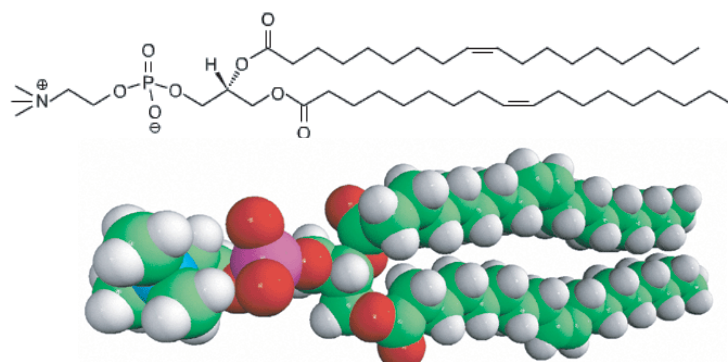
5 Preparation Techniques and Experimental Methods

5.1 Materials and Preparation Techniques

Chemicals 1,2-Dioleoyl-sn-Glycero-3-Phosphocholine (DOPC) [Fig. 5.1 (a)] and 1,2-Dioleoyl-3-Trimethylammonium-Propane (DOTAP) [Fig. 5.1 (b)] were bought from Avanti Polar Lipids Inc. (Alabaster, USA) and used without further purification.

2-(12-(7-nitrobenz-2-oxa-1,3-diazol-4-yl)amino)dodecanoyl-1-hexadecanoyl-sn-glycero-

(a) DOPC



(b) DOTAP

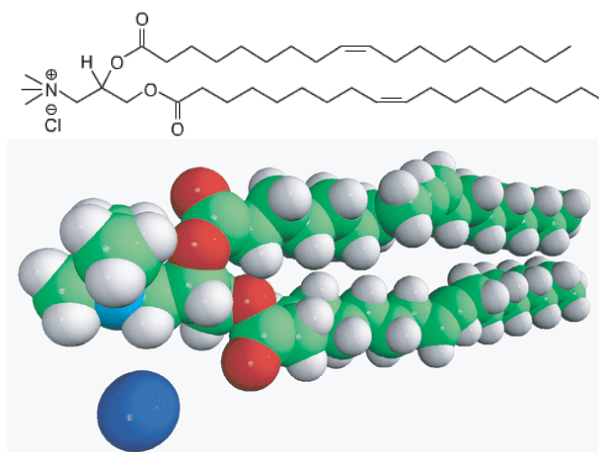


Figure 5.1: (a) Structure formula of DOPC. (b) Structure formula of DOTAP.

3-phosphocholine (NBD C12-HPC) was purchased from Molecular Probes (Eugene, USA). For diffusivity measurements, 1% (w/w) of the fluorescence probe was used to label the membrane. For the experiments with DNA, the lipids were mixed with 0.05% (w/w) of 2-(4,4-difluoro-5-(4-phenyl-1,3-butadienyl)-4-bora-3a,4a-diaza-s-indacene-3-pentanoyl)-1-hexadecanoyl-sn-glycero-3-phosphocholine (Bodipy-C5HPC, Molecular Probes, Eugene, USA).

Only freshly bidistilled water (18.2 M Ω , Millipore, Billerica, USA) was used throughout this study.

Chloroform, toluene and 2-propanol were bought at HPLC grade from Carl Roth GmbH & Co (Karlsruhe, Germany).

N-(2-Hydroxyethyl)piperazine-N'-(2-ethanesulfonic acid) (HEPES), tris(hydroxymethyl)aminomethane (TRIS), CaCl₂, MgSO₄, NaCl, ascorbic acid (vitamin C), ethylene-diamine-tetraacetic acid (EDTA), H₂O₂, and NH₄OH were bought from Sigma Aldrich (Taufkirchen, München) at a purity of 99.5%. N-octyl beta-D-glucoside (octyl glycoside, OG) was purchased from Bachem (Basel, Switzerland).

The DNA intercalating dyes, 1-1'-[1,3-propanediylbis[(dimethyliminio)-3,1-propanediyl]]bis[4-[(3-methyl-2(3H)-benzothiazolydene)methyl]]-tetraiodide (TOTO-1) and 4-[(3-methyl-2(3H)-benzoxazolydene)methyl]-1-[3-(trimethylammonio)propyl]-diiodide (YO-PRO-1), were bought from Molecular Probes (Eugene, USA).

Buffer Solutions For the phage experiments, the following buffer solutions were needed:

phage buffer: 10 mM Tris-HCl, 100 mM NaCl, 1 mM MgSO₄, and 1 mM CaCl₂ (pH 7.6)

flow buffer: 10 mM Tris-HCl, 100 mM NaCl, 1 mM MgSO₄, and 1 mM CaCl₂ 0.1 μ M YO-PRO-1 and 0.01% OG (pH 7.6)

OG buffer: 25 mM HEPES, 150 mM NaCl, OG 0.5% (w/v) (pH 7.4)

For the DNA experiments the following buffers were prepared:

attachment buffer: 10 mM Hepes (pH 7.0)

salt buffer: 10 mM Hepes, 30 mM NaCl, 5 mM Vit C (pH 7.0)

DNA storage buffer: 10 mM Tris, 1 mM EDTA (pH 7.5) (TE buffer)

Buffers were filtered and autoclaved. They were freshly degassed before usage.

DNA λ -phage DNA (48 502 bp) was bought from Roche (Mannheim, Germany), diluted to a concentration of $0.1 \mu\text{g}/\text{ml}$ in DNA storage buffer and stored at -20°C . $127 \mu\text{l}$ of a $0.5 \mu\text{M}$ Toto-1 solution and 1 ml of the attachment buffer were added to $200 \mu\text{l}$ of DNA. The solution was heated to 50°C for 20 min . This results in a labelling ratio of 1:5. Pipet tips were cut to avoid high shear forces during DNA handling.

Microfluidic Chambers The plastic chambers (μ -Slides, ibidi GmbH, München, Germany) consisted of two reservoirs connected by a channel with dimensions $5 \times 0.4 \times 50 \text{ mm}^3$ (width \times height \times length). The bottom of the channel was sealed with a plastic foil made out of the copolymer 2-norbornene ethylene (cyclic olefin copolymer, COC). Its high transparency and the thickness of 0.18 mm allow the application of high resolution optical microscopy ([Fig. 5.2 (a)]. The microfluidic chambers were cleaned before use by flushing 2 ml of 2-propanol through the flow chamber followed by at least 20 ml of bidistilled water. For the x-ray reflectivity measurements, a thin film

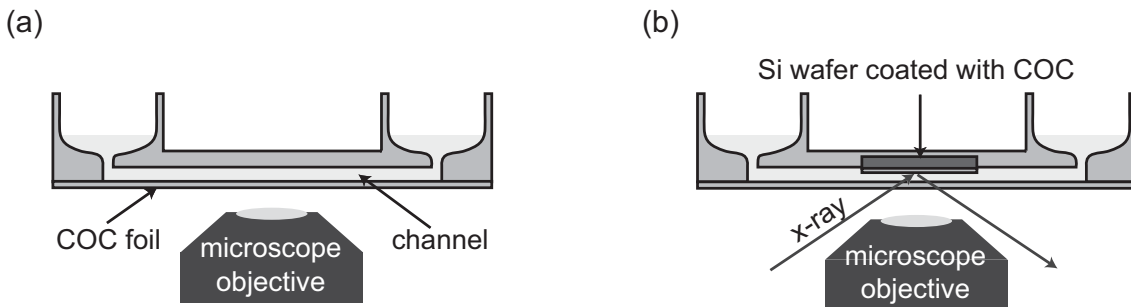


Figure 5.2: Microfluidic Chambers: (a) Schematic drawing of the plastic chamber used for microscopy (side view). (b) Modified chamber for the x-ray measurements (side view).

of COC was prepared by spin-coating COC onto a silicon wafer thus avoiding the long range undulations present in free-standing foils. A silicon wafer ($20 \times 20 \text{ mm}^2$) with a thermally grown oxide layer of 400 nm thickness was cleaned thoroughly for the COC coating by a modified RCA method [69]. In short, the wafer was ultrasonicated for 5 min in acetone, in 2-propanol, and in water. Afterwards it was boiled at 80°C in a $1:1:5 \text{ H}_2\text{O}_2:\text{NH}_4\text{OH}:\text{H}_2\text{O}$ mixture. The wafer was shortly rinsed in bidistilled water, then boiled in $1:1:5 \text{ H}_2\text{O}_2:\text{HCl}:\text{H}_2\text{O}$ at 80°C . The wafer was dried at 70°C for 3 hours . $300 \mu\text{l}$ of $1 \text{ mg}/100 \text{ ml}$ COC dissolved in toluene was deposited onto the wafer and the wafer accelerated to 3000 rpm for 2 min . This procedure yielded a homogeneous, smooth COC layer with a thickness of around 450 \AA and a surface roughness of 7 \AA .

A specially modified chamber was used to embed the silicon wafer as described in detail elsewhere [70]. In brief, the μ -slide was milled open with a square of the size of the wafer. The wafer was embedded into the chamber with the COC layer facing towards

the channel interior. Finally the chamber was sealed again with a two component epoxy glue (“Uhu Plus Endfest 300”, Uhu GmbH, Bühl, Germany) [Fig. 5.2 (b)]. After drying for several hours, the chamber was ready for the deposition of the lipids.

Assuming a Poiseuille flow, the volume flow rate can be related to the shear rate at the bottom of the chamber by $\gamma = 6\Phi/wh^2$ ($w = 5$ mm width of chamber, $h = 0.4$ mm height of chamber). We flushed up to 8 ml/min through the channel resulting in a shear rate of roughly 1000 s^{-1} .

The patterned COC surface used in the DNA experiments were produced the following way:

The grating substrates were produced using holographic methods and subsequent reactive ion etching techniques on (100) silicon wafers (25 Å of native oxide)[71]. To imprint the negative structure on COC [72], the waver was put onto a COC foil with a weight of 80 g. The temperature was raised to 150°C and the sample equilibrated over night (s. Fig. 5.3). The master was removed after the temperature had dropped below 70°C[73]. The foil was glued to the μ -slide top part with the patterned surface facing into the channel.

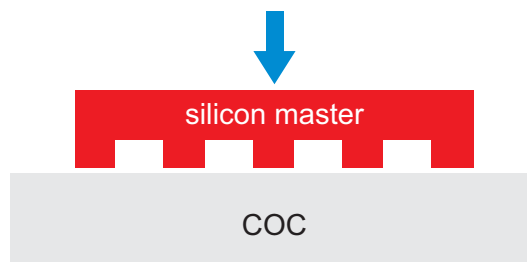


Figure 5.3: : Imprinting: the silicon master is pushed onto the planar COC foil while the temperature is raised to 150°C.

DNA Adsorption Procedure The water inside the microfluidic chamber was exchanged to the attachment buffer. Excess buffer in the reservoirs of the chamber was removed such that only roughly 200 μl of buffer were left. 200 μl of the DNA solution was added. Adsorbed DNA molecules could be seen with a fluorescence microscope as small disk-like bright spots. The salt free attachment buffer provides a rapid deposition rate of the anionic DNA molecules, yet it immobilizes them after they had attached to the membrane. The concentration of adsorbed molecules was monitored with time and the DNA containing buffer exchanged to the salt buffer once the desired concentration was achieved. This was usually the case after 5 min. The exchange to a salt containing buffer activates the post-deposition dynamics of the adsorbed DNA by screening electrostatic interactions. Therefore the adsorbed DNA molecules are now freely diffusing in the 2-D plane of the lipid membrane. During the entire adsorption procedure great care was taken to avoid exposure to air.

Vesicle Fusion (VF) The desired lipid ratio was mixed in chloroform, dried under nitrogen flow, and stored in a vacuum chamber over night. Bidistilled water was added to the dried lipid to a concentration of 1 mg/ml and the solution was incubated for 4 h at 50°C resulting in multilamellar vesicles. Small unilamellar vesicles were prepared by sonicating the lipid-water mixture in a tip sonicator (Sonoplus UW 2070, Bandelin electronic, Berlin, Germany) for 10 min at an amplitude of 170 μm while the solution was cooled on ice [74]. 400 μl of the lipid solution were deposited into the chamber channel and incubated over night. The chamber was washed with at least 100 ml of bidistilled water while great care was taken to avoid air contact with the lipid layer.

Solvent Exchange (SE) The lipids were mixed and dried as described above. A solution with a concentration of 1 mg/ml was prepared by adding 2-propanol to the dried lipid. 200 μl of the lipid solution were injected to the chamber. 2 ml of bidistilled water were added into one of the two reservoirs of the chamber which lead to a reduction of the 2-propanol content in the solvent to 10%. After equilibration of the water levels in both reservoirs, 30 ml of bidistilled water were quickly flushed through the plastic slide to remove excess vesicles in the buffer solution and reduce the amount of vesicles adhered to the membrane.

For comparison, a membrane on a hydrogen-terminated silicon wafer (H-Si) was prepared as follows: a DOPC membrane was deposited by spin coating a DOPC 2-propanol solution (1 mg/ml) immediately after a HF etch [30]. Then the dried sample was placed in the microfluidic chamber and flushed with water prior to the measurement.

T5 Phage Wild-type T5 (wt) and T5 st(0), a heat stable deletion mutant, were used throughout this study. They were produced on *E. coli Fsu β ⁺* and purified by polyethylene glycol precipitation followed by a CsCl-step gradient as described in Bonhivers et al. [75]. They were stored in phage buffer at a concentration of 10¹³ phage particles/ml at 4°C.

FhuA was overexpressed in *E. coli HO830fhuA* transformed with plasmid pHX405 and purified following the protocol described in Boulanger et al. [76]. The protein was solubilized in OG buffer and stored at 4°C at a concentration of 2 mg/ml.

5.2 Methods

5.2.1 Fluorescence Microscopy

Principles of Fluorescence Microscopy A fluorochrome is able to absorb a certain range of wavelengths. Fig. 5.4 shows a schematic drawing illuminating the following

explanations. The excited electron of the fluorochrome relaxes very fast from higher rotational and vibrational states to the lowest excited state (S_1). From this state the electron can return to the ground state (S_0) or to some vibrational state above it while emitting a red-shifted photon. In rare cases, the electron undergoes intersystem crossing to the triplet state from where it also returns to the ground state by emitting a red shifted photon (phosphorescence). A sample labeled with a fluorescence probe is illuminated

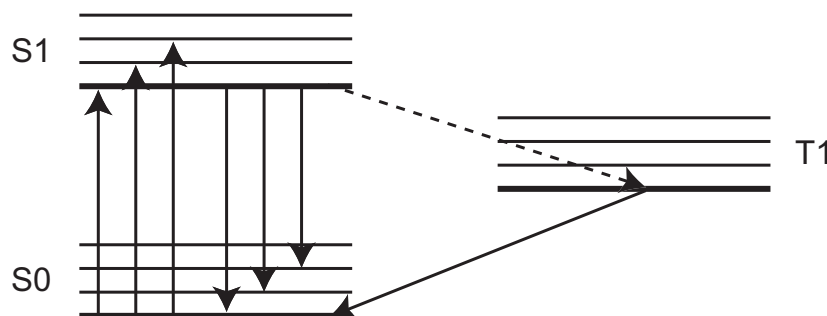


Figure 5.4: Simplified Jablonski diagram showing the possible transitions of a fluorochrome. By photon absorption the electron is lifted from the ground state S_0 to an excited state S_1 . The electron relaxes back to the ground state by emitting a photon of reduced energy. In rare cases the electron can perform the so called intersystem crossing and ends up in the triplet state T_1 from where it can relax back to the ground state by releasing a photon (phosphorescence).

with light within the absorption wavelength range. The emitted red-shifted fluorescence light is collected with an objective which creates a sharp image of the fluorochrome distribution in the sample. This image can be detected with a CCD camera or it might be seen with the eyes with the help of ocular lenses. In this study, an epi-fluorescence setup was used, i.e. the excitation light is steered through the same objective lenses that are used for the collection of the emitted light.

Experimental Details Fluorescence microscopy was performed on an inverted fluorescence microscope (Axiovert 100M, Carl Zeiss, Oberkochen, Germany) equipped with an $100\times$ oil immersion objective (100 Plan Neofluar, N.A. 1.3, Carl Zeiss, Oberkochen, Germany). Images were captured with a CCD camera (CoolSnap HQ, Photometrics, Roper Scientific Inc., Tuscon, USA) and analyzed with Igor Pro 4.0 (Wavemetrics, Portland, USA).

5.2.2 Continuous Bleaching

The diffusivity of lipid membranes is determined by Continuous Bleaching following the method initially developed by Dietrich et al. [77]. The field stop of the microscope is

closed in such a way that only a roughly circular spot ($\odot 70 \mu\text{m}$) is illuminated while the rest of the membrane is left in the dark.

In the center of the observation area, the fluorescence signal of the membrane decays exponentially as a function of exposure time as expected for a large ensemble of continuously excited dyes:

$$I(x = d/2, t) = I_{d/2} e^{-bt} + B. \quad (5.1)$$

Here $I(x, t)$ is the intensity, x is the distance from the rim towards the center of the illuminated area, d is the diameter of the field stop, t is the time since the beginning of the exposure, B is the background noise, and b is the bleaching constant, which depends on the brightness of the illumination, the buffer, and on the fluorescent molecule used.

At the edge of the illuminated area, two cases have to be taken into account. If the membrane is immobile, a discontinuous jump in the concentration of unbleached dyes forms at the edge of the illuminated area. If the lipid layer is fluid, unbleached fluorescently labeled lipids from the surrounding non-illuminated area diffuse continuously into the illuminated spot thereby increasing the fluorescence signal at the rim. Hence, a bright halo forms at the periphery of the illuminated area. In this case, the signal decreases approximately exponentially from the dark field stop towards the middle of the observation area:

$$I(x, t_0) = I_{t_0} e^{-x/\lambda} + B = I_{t_0} e^{-\sqrt{b/D}x} + B, \quad (5.2)$$

where λ is the decay length, $D = b/\lambda^2$ is the diffusion constant of the lipid layer, and b is the bleaching constant. Equation 5.2 holds only for small x . If x is too large, the decaying fluorescence signal is obscured by the background. It is important that an equilibrium between the bleaching process and the diffusion process is established. Care has to be taken that the sample is not bleached too much for having a good signal to noise ratio. Both conditions are met within $5 \leq tb \leq 10$.

5.2.3 Fluorescence Recovery After Photobleaching

Introduction to the Technique Fluorescence recovery after photobleaching (FRAP) is a method for measuring the lateral mobility of fluorescent particles. A small spot on a fluorescent surface is bleached by short exposure to an intensive focused laser beam. The subsequent recovery of the fluorescence is monitored by another attenuated laser beam. Recovery occurs because intact fluorophores are transported in the bleached spot from the surroundings.

Here, only the theory concerning the transport by diffusion monitored with an uniform circular laser profile will be described. It is thus possible to determine the diffusion constant D and the mobile fraction M of the fluorophore.

The bleaching intensity $I(r)$ is given by

$$I(r) = \begin{cases} \frac{P_0}{\pi\omega^2} & : r \leq \omega \\ 0 & : r > \omega \end{cases}, \quad (5.3)$$

where P_0 is the laser power, ω the beam radius, and r is the distance from the center of the bleaching spot. If the photobleaching of the fluorophore is an irreversible first-order reaction with rate constant α , the concentration of the unbleached fluorophore $C(r, t)$ can be calculated from

$$\frac{dC(r, t)}{dt} = -\alpha I(r)C(r, t). \quad (5.4)$$

The concentration immediately after bleaching at $t = 0$ is given by

$$C(r, 0) = C_0 \exp(-\alpha T I(r)), \quad (5.5)$$

where C_0 is the initial uniform fluorophore concentration. T is the bleaching time which should be short compared to the characteristic time of diffusion τ_D . The concentration is determined by the following diffusion equation:

$$\frac{\partial C(r, t)}{\partial t} = D\Delta C(r, t). \quad (5.6)$$

If the solution is denoted as $C_K(r, t)$, the fluorescence signal $F(t)$ at $t \geq 0$ can be represented by

$$F_K(t) = \left(\frac{q}{A}\right) \int I(r)C_K(r, t)d^2r, \quad (5.7)$$

where q is the combined quantum efficiency of absorption and emission and A the attenuation factor. To simplify the mathematic description, it is more convenient to display a fluorescence recovery curve in the fractional form

$$f_K(t) = \frac{[F_K(t) - F_K(0)]}{[F_K(\infty) - F_K(0)]}. \quad (5.8)$$

Here, the fractional recovery curve can be described as

$$f_K(t) = 1 - \left(\frac{\tau_D}{t}\right) \exp\left(\frac{-2\tau_D}{t}\right) \left[I_0\left(\frac{2\tau_D}{t}\right) + I_2\left(\frac{2\tau_D}{t}\right)\right] \\ \mp 2 \sum_{k=0}^{\infty} \frac{(-1)^k (2k+2)! (k+1)! \left(\frac{\tau_D}{t}\right)^{k+2}}{(k!)^2 [(k+2)!]^2}, \quad (5.9)$$

where $\tau_D = \frac{\omega^2}{4D}$ [78]. The mobile fraction M can be determined quantitatively from the recovery ratio

$$M = \frac{F_K(\infty) - F_K(0)}{F_K(-) - F_K(0)}, \quad (5.10)$$

where $F_K(-)$ is the fluorescence signal before bleaching. If one considers the diffusion of bleached fluorophores to the outside of the spot, the following equation can be derived [79]:

$$F_K(t) = F_K(\infty) - \\ [F_K(-) - F_K(0)] \cdot \\ \left\{1 - \exp\left(\frac{-2\tau_D}{t}\right) \left[I_0\left(\frac{2\tau_D}{t}\right) + I_1\left(\frac{2\tau_D}{t}\right)\right]\right\}. \quad (5.11)$$

This equation was used to fit the experimental data. The parameter are used to extract D and M .

Experimental Setup Fluorescence Recovery After Photobleaching (FRAP) [78] was measured on a modified inverted microscope (Axiomat, Carl Zeiss, Oberkochen, Germany). The beam ($\lambda = 488$ nm) of a 0.8 W argon laser (Innova 70-4, Coherent Inc., Santa Clara, USA) was split into a bleaching and an observation beam such that the intensity of the bleaching beam was more than $1000\times$ stronger than the observation beam. The microscope objective ($100\times$ Fluar N.A. 1.3, Carl Zeiss, Oberkochen, Germany) was used to direct both beams to the same spot and collect the fluorescence. A rectangular intensity profile with a diameter of $9.3\ \mu\text{m}$ was created by insertion of a pinhole into the beam path. The dye molecules were bleached by a short laser pulse (200 ms), and the recovery of the fluorescence intensity was monitored with a photomultiplier (Hamamatsu Photonics). The lateral diffusion constant D and the mobile fraction M were calculated from the measured fluorescence recovery profiles, following the method reported by Soumpasis [79] (s. Equation 5.11).

5.2.4 X-ray Reflectivity

Theory of Specular X-Ray Reflectivity Specular x-ray reflectivity can be described with the laws of classical optics if the appropriate index of refraction n is used. For x-rays, $n = 1 - \delta - i\beta$, with the dispersion δ and the adsorption β :

$$\delta = \frac{r_0}{2\pi} \lambda^2 \rho \quad \text{and} \quad (5.12)$$

$$\beta = \frac{\lambda}{4\pi} \mu. \quad (5.13)$$

λ is the wavelength of the incident wave, r_e the electron radius, which is also known as the Thompson scattering length of the electron. ρ is the electron density and μ the linear absorption coefficient.

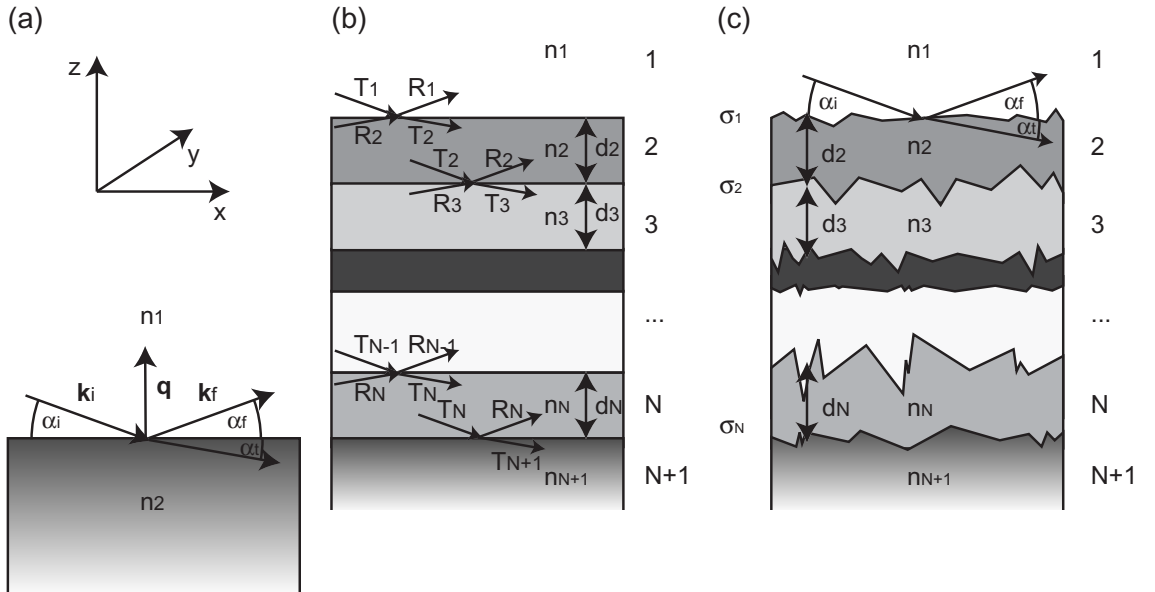


Figure 5.5: X-Ray Reflectivity: (a) The incident wave is scattered at a perfectly smooth surface resulting in a reflected beam and a transmitted beam where $\alpha_i = \alpha_f$ and $\cos\alpha_t = \frac{n_1}{n_2} \cos\alpha_i$. (b) Sketch of a system consisting of $N+1$ layers with N interfaces. (c) Same multilayered system, now including interface roughnesses.

For a single interface between two media with the refractive indices n_1 and n_2 an incoming electromagnetic wave with wavevector \mathbf{k}_i ($|\mathbf{k}_i| = \frac{2\pi}{\lambda}$) is splitted into a reflected ($\alpha_i = \alpha_f$) and a transmitted wave with an angle α_t ($\cos\alpha_t = \frac{n_1}{n_2} \cos\alpha_i$) (Fig. 5.5 (a)). We only consider elastically scattered waves with $|\mathbf{k}_i| = |\mathbf{k}_f|$. The intensity R_F of the

reflected x-ray wave (“Fresnel Reflectivity”) can be analytically determined from Fresnel’s equations. Total external reflection occurs if $n_1 < n_2$ and $\alpha_i < \alpha_c = \sqrt{2(\delta_2 - \delta_1)}$. For $\alpha_i > 3\alpha_c$, R_F can be approximated by $R_F = (\alpha_c/2\alpha_i)^4$.

For practical applications, the case of multiple interfaces is more interesting than that of a single surface. Fig. 5.5 (b) shows a multilayer stack consisting of N interfaces. Scattering from all interfaces has to be taken into account. The recursion algorithm described in the classic paper of Parrat et al. [80] allows to calculate the reflection and transmission coefficients (R_j and T_j) of the j^{th} interface from R_{j-1} and T_{j-1} of the preceding interface. Assuming that the reflectivity of the substrate R_{N+1} is zero and that $T_1 = 1$ all reflectivity coefficients can be calculated, arriving finally at R_1 , the measured reflectivity.

In practice, interfaces are always rough. Therefore the measured reflectivity will be significantly lower than the intensity calculated in the previous paragraph. Instead of looking at a constant refractive index n with sharp steps it is now preferable to think of a continuous refractive index $n(x, y, z)$. Since the moment transfer $\mathbf{q} = \mathbf{k}_i - \mathbf{k}_f$ ($|\mathbf{q}| = \frac{4\pi}{\lambda} \sin(\alpha_i)$) is parallel to the z axis, which is perpendicular to the sample surface, one-dimensional refractive index profiles are considered:

$$n_j = \iint n_j(x, y, z) dy dx. \quad (5.14)$$

with σ_j being the surface roughness of the j^{th} interface. The refractive index profile in between the layers j and $j + 1$ is assumed to be:

$$n_j(z) = \frac{n_j + n_{j+1}}{2} - \frac{n_j - n_{j+1}}{2} \operatorname{erf}\left(\frac{z - z_j}{\sqrt{2}\sigma_j}\right). \quad (5.15)$$

The recursive algorithm can now be modified accordingly, yielding the final reflectivity R_1 .

Experimental Details All x-ray reflectivity measurements using COC supports were performed at the ESRF in Grenoble (France) at the beamline ID01. The measurement of a lipid membrane supported by hydrogen terminated silicon was carried out at HasyLab (beamline D4, Hamburg, Germany). The x-ray energy was 19.5 keV ($\lambda = 0.636 \text{ \AA}$). The energy was chosen to minimize parasitic effects such as incoherent scattering while maximizing coherent scattering on the sample. The data analysis takes into account the correction for background, footprint, and beam attenuation. The attenuation correction is dependent on the angle of incidence because the beam passes through different lengths of the plastic COC (l) and water (d) (s. Fig. 5.6 (b)). The loss of intensity is less than one order of magnitude due to the compact chamber geometry. Details of the experimental

setup are described in Reich et al. [70]. Special care was taken to avoid beam damage due to overexposure by shifting the sample during the measurement. Since all reflectivity curves could be reproduced with a high accuracy during several consecutive scans, we can exclude beam damage. The data were analyzed using the Parratt algorithm [80].

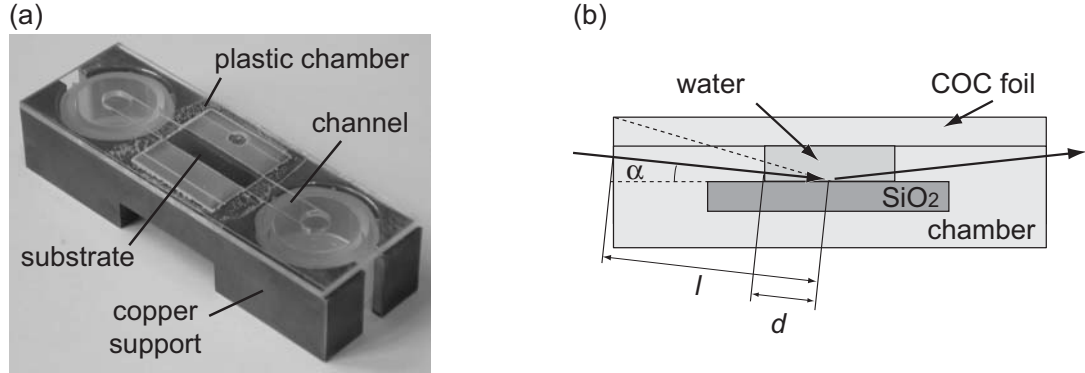


Figure 5.6: X-Ray Reflectivity: (a) Photo of a microfluidic chamber used during the experiments. The chamber is inserted in a copper block to stabilize it during reflectivity experiments. (b) Schematic drawing of a cross section along the plane of incidence: The incoming beam travels through the length l of the plastic material COC and then the length d through the bulk water. The reflectivity data is corrected for the resulting attenuation.

5.2.5 Atomic Force Microscopy

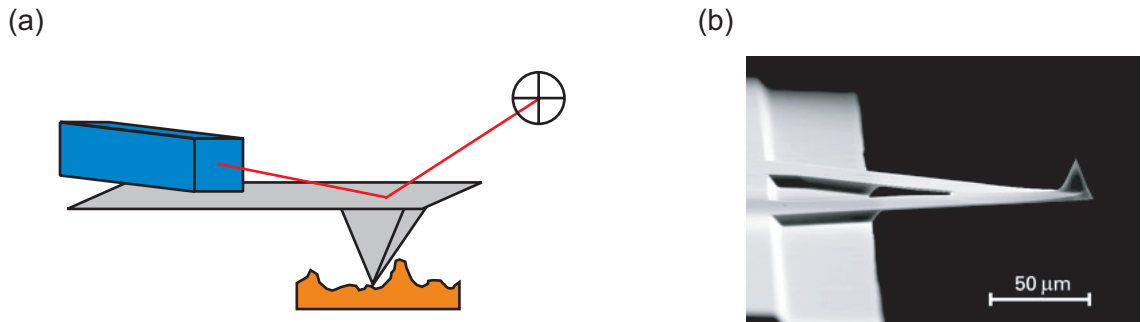


Figure 5.7: Schematic setup of Atomic Force Microscopy (AFM). A sharp tip attached to a cantilever is pulled over a surface. Height undulations lead to deflection of the cantilever which is registered by the movement of a reflected laser beam.

A very sharp tip (tip radius < 10 nm) is grown onto a silicon nitride cantilever. The tip is pushed onto a surface with a constant force while it is moved horizontally. The deflection of the cantilever resulting from height modulations of the surface are detected. A laser

beam is reflected from the cantilever and variations of the position of the reflected beam are measured by a quadrant diode (Fig. 5.7). Atomic Force Microscopy (AFM) pictures were taken on a NanoScope MultiMode AFM (Digital Instruments, Santa Barbara, USA) in contact mode with a constant force and 512 dots per line and 512 lines.

5.2.6 Scanning Electron Microscopy

An electron microscope uses electrons with a deBroglie wavelength $\lambda = h/\sqrt{2m_e eU}$ to resolve structural details of a sample. Here, m_e is the electron mass, e is the electron charge, and U is the voltage used to accelerate the electron beam. The electron beam is created in the electron gun and accelerated to the desired voltage. The electron beam is collimated by electromagnetic lenses and focused to a very fine spot. The scanning coils deflect the electron beam such that the electron beam is moved back and forth across the specimen. The electron beam hits the surface and frees electrons from the sample. These electrons are detected and an image is generated.

A field emission scanning electron microscope (Modell DSM 982 Gemini, LEO Elektronenmikroskopie GmbH, Oberkochen, Germany) was used to image both the gold sputtered imprinted foil and the original master at 5 keV.

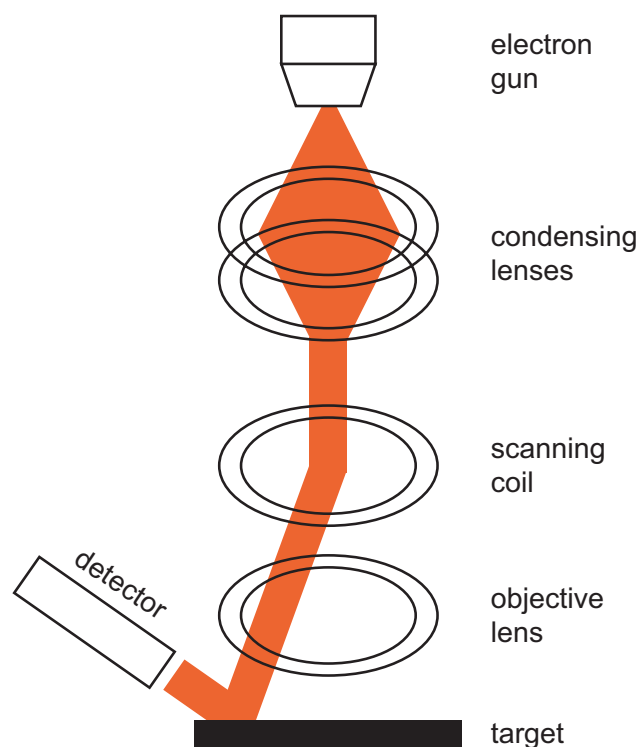


Figure 5.8: Schematic setup of Scanning Electron Microscopy (SEM).

6 Real-Time Imaging of DNA Ejection from Single Phage Particles

6.1 Introduction to T5 Phage

Bacterial viruses or bacteriophages, frequently called “phages”, were discovered at the beginning of the twentieth century. Bacteriophages constitute one order, 13 families, and 30 genera which is a proof of their diversity. Tailed dsDNA phages (Caudovirales) consist

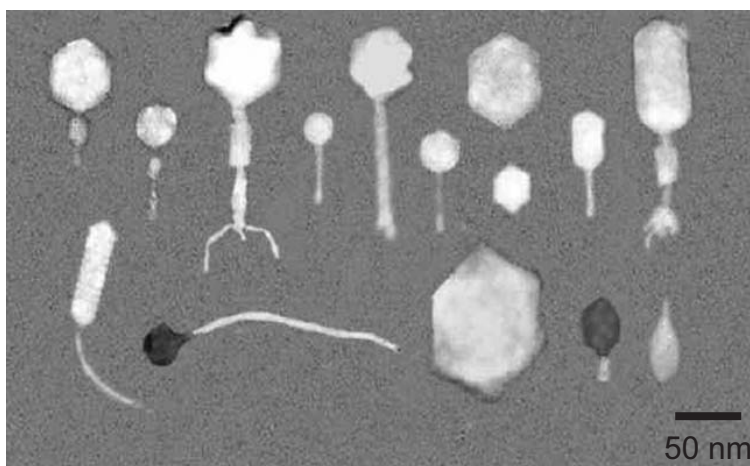


Figure 6.1: Electron microscopy images of different phages. Image taken from reference [81].

of an isometric proteinaceous capsid in which the viral genome is condensed [2]. Located at one of the capsid vertices is an oligomeric protein structure, the connector, that links the capsid to the tail and forms the channel through which the DNA is packaged during morphogenesis and exits during infection [82]. The tail ends with fibers and a tail tip that ensures the binding of the phage to a specific host membrane receptor.

The native hosts of the T5 phage are *Escherichia coli* bacteria. *E. coli* are gram negative bacteria which means that the phage DNA has to overcome two hydrophobic barriers: the outer and the inner membrane. Furthermore it has to cross the periplasm, the space separating the two membranes which contains nucleases and the rigid polymeric

structure of the peptidoglycan. Infection results after a phage particle has reversibly bound to liposaccharides of the *E. coli* outer membrane with its tails fibers. The phage irreversibly binds to the membrane protein FhA with pb5, a protein located at the distal end of the phage tail. FhuA is an outer membrane protein of *E. coli* that transports iron chelated to the siderophore ferrichrome [76]. Upon infection, receptor binding leads to conformational changes that are transmitted to the connector triggering its opening and the release of the DNA, which is transferred to the cytoplasm linearly base pair after base pair through the bacterial envelope (reviewed in [83] and [84]). The T5 infectious

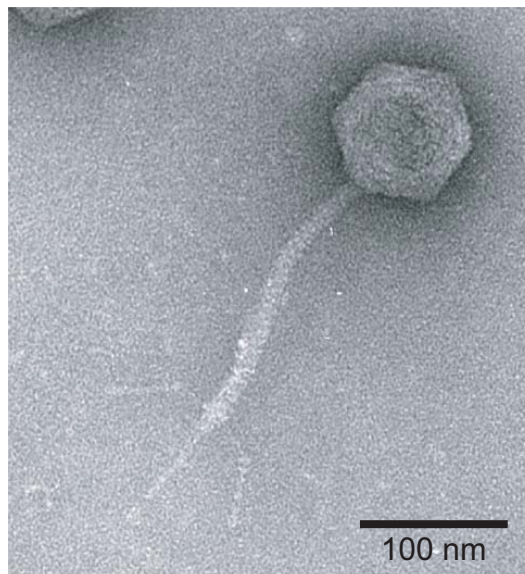


Figure 6.2: Electron microscopy image of a T5 phage virion. Image taken at the Institut de Biochimie et Biophysique Moleculaire et Cellulaire, UMR, CNRS at Université Paris Sud. Permission for publication granted by L. Letellier.

cycle lasts roughly 20 min during which about 200 new phages are produced. Its DNA (121.4 kbp, 41.3 μm) may be released from the capsid in vitro by mere interaction of the phage with its purified *Escherichia coli* outer membrane protein receptor, FhuA [75, 85, 86].

6.2 Setup

For the experiment, phage particles were adsorbed onto the plastic COC foil of a microfluidic chamber. The receptor protein FhuA was added which triggered the release of the phage DNA into the bulk solution. The DNA was fluorescently labeled by an intercalating dye. A constant flow stretched the DNA during the ejection process when still attached to the phage capsid. The length of the ejected DNA was monitored with

a fluorescence microscope. The experimental setup is shown schematically in Fig. 6.3. The best results were obtained for the following experimental conditions:

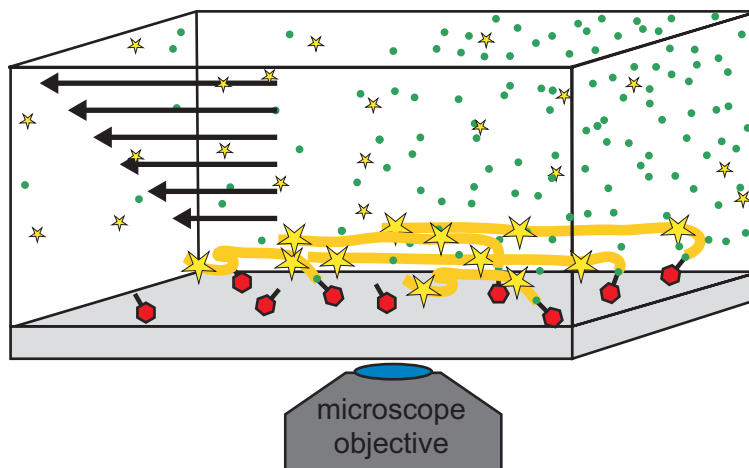


Figure 6.3: Schematic drawing of the experiment: Phage particles (red hexagons) adsorb to the COC surface in the microfluidic slide. The phage DNA is stained with an intercalating dye (yellow stars). The injection of the receptor protein FhA (green dots) triggers the ejection of the phage DNA. The partly ejected DNA is stretched by an applied hydrodynamic flow (depicted as black arrows). The ejection process can now be monitored with a fluorescence microscope.

Adsorption Procedure $150\ \mu\text{l}$ of a phage solution containing 6×10^6 particles/ml were incubated for 5 min in the microfluidic chamber to allow the T5 phage particles to adsorb to the bottom of the microfluidic chamber. We found that the amount of attached phages did not increase further when the incubation time was prolonged to as much as one hour.

The concentration of attached phages was roughly proportional to the phage concentration during incubation. Therefore we chose a incubation concentration that resulted in a phage surface density that allowed to observe several phages at once which improved the statistics while still keeping the probability low that two phages attached too close together to be resolved separately.

The phage particles resisted continuous perfusion with the flow buffer up to a flow velocity of $10\ \text{ml}/\text{min}$ for more than one hour without being detached (data not shown). Therefore we conclude that the phage particles were strongly bound to the surface.

Fluorescence Label The intercalating dye YO-PRO-1 (Molecular Probes, Eugene, USA) was used to stain the phage DNA because previous studies showed that T5 retains infectivity in the presence of this dye [76]. Addition of YO-PRO-1 ($200\ \mu\text{l}$ yielding a final concentration of $0.1\ \mu\text{M}$) resulted in the appearance of

bright spots corresponding to individual phage particles that were either stained by the diffusion of the dye through the capsid or by staining of the capsid itself. This allowed us to focus onto the surface before the ejection was started. The YO-PRO-1 concentration was chosen such as to obtain a reasonable fluorescence signal while avoiding quenching effects.

Flow Buffer Low concentrations of the surfactant octyl glucoside (OG) had a protective effect against photobleaching and DNA breaking usually induced by intercalating dyes [87]. High amounts of OG lead to air bubbles in the flow buffer which tore apart the phages. This led to a release of DNA which stucked irreversibly to the surface. A concentration of 0.01% OG in the flow buffer turned out to provide optimal results.

It was necessary to keep the concentration of the intercalating dye YO-PRO-1 at $0.1\ \mu\text{M}$ during the stretching because the DNA fluorescence would eventually subside without it. An explanation of why the fluorescence signal deteriorated without YO-PRO-1 in the flow buffer is given in the following: Since the dye is not covalently bound to the DNA, it does have a considerable on/off kinetic. Unbound dye molecules will be swept away immediately when a flow is applied and can not be replenished if the flow buffer does not contain the dye.

Strength of Flow To resolve the ejection process with the fluorescence microscope it was necessary to stretch the partly ejected phage DNA. Without a flow the DNA builds a random coil where the contour length cannot be resolved with optical microscopy. The flow should stretch the DNA reasonably while not exerting too high force on it to avoid overstretching. Details will be discussed in the next chapter.

Illumination The illumination of the sample had to be carefully controlled to avoid bleaching and breaking of the exposed DNA molecules as observed previously with this family of intercalating dyes [87] while still allowing the detection of single DNA molecules. Therefore the illumination was reduced to 6% by a neutral density filter.

FhuA Concentration and Temperature Throughout the incubation process and during all following experiments the chamber temperature was stabilized at 23°C . To trigger the ejection process, $40\ \mu\text{l}$ ($0.8\ \mu\text{g}$) of FhuA in OG buffer was added resulting in a ratio of FhuA to phage particles of 4000:1. These conditions allowed efficient receptor binding and DNA release.

6.3 Response of the Ejected DNA to a Hydrodynamic Flow of Variable Strength

DNA stretching by flow is completely reversible. Without flow the DNA forms a random coil (Fig. 6.4 (a)). The same DNA can be stretched to the left (Fig. 6.4 (b)) and right (Fig. 6.4 (c)). The extension of partly ejected DNA was measured at varying strengths

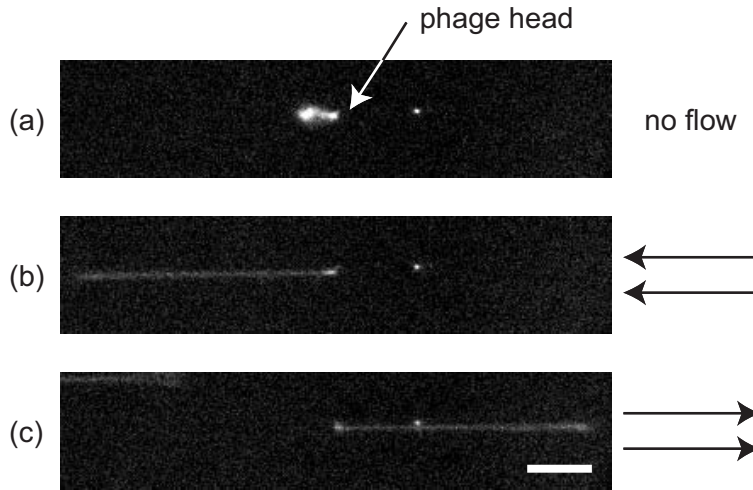


Figure 6.4: Fluorescence microscopy pictures of a single phage particle with partly ejected DNA. The white bar has a size of $10 \mu\text{m}$. (a) No flow is applied, the DNA is in a random coil conformation. (b) A flow is applied which stretches the DNA to the left or (c) to the right.

of the flow. Accurate measurements required to know how much the intercalating dye increased the mean basepair distance. We assumed that YO-PRO-1 intercalation leads to an overestimation of the DNA length by a factor of approximately 1.2 [52]. The measured DNA length was divided by this factor to gain an extension per basepair of 0.34 nm which corresponds to a contour length of $41.2 \mu\text{m}$ of the complete T5 phage DNA. Fig. 6.5 displays the length L_z of four representative DNA strands versus the applied flow Φ after applying the correction for the intercalating dye. The DNA length increased monotonically with the flow and reached a plateau for flows higher than 2 ml/min (shear rate: 250 s^{-1} , see 5.1). For the extrapolation of the plateau value L_0 the data was fitted with the relation:

$$L_z = L_0 \left[1 - (C\Phi)^{-1/3} \right], \quad (6.1)$$

where L_0 and C represent adjustable parameters, see section 3.2.2. Consistent with the work of Doyle et al. [17] for a tethered DNA molecule in shear flow, we also observed a cyclic dynamic motion of the ejected DNA molecules. Next, we plotted the relative

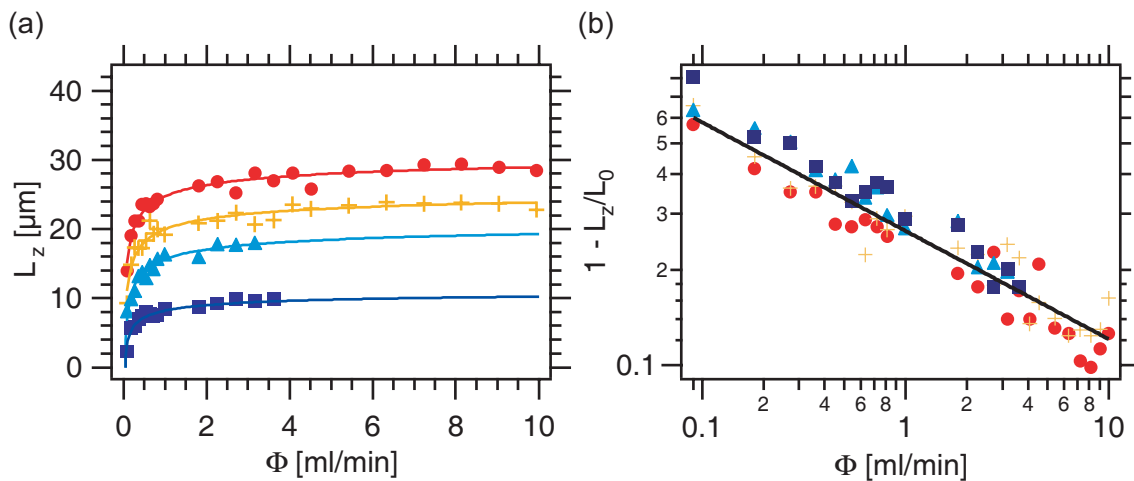


Figure 6.5: Length of ejected DNA versus applied flow: (a) The length of the ejected DNA is plotted for different phages versus the applied flow. From the fitted curves (solid lines) the plateau value, the contour length, can be derived. By measuring at a flow velocity of 0.6 ml/min, the contour length is underestimated by a factor of 1.3. (b) $1 - L_z/L_0$ is plotted for the same four viruses versus the flow rate in a log-log graph. The expected slope of $-1/3$ is shown as a black solid line which describes the data accurately.

extension L/L_0 versus the flow and compared the curve obtained with the force-extension curve of a DNA molecule to whose end a force is applied [88] (Fig. 6.5). Because both curves overlap, it may be deduced that a maximum force of 10 pN was applied under our experimental conditions. Further experiments were performed at flow rates of 0.5 to 0.6 ml/min which corresponds to a force of about 2 pN. Therefore the measured lengths needed to be corrected by a factor of 1.3 to compensate for the incomplete extension.

6.4 Phage Ejection Process

6.4.1 Stepwise Ejection

The fluorescence increased locally after FhuA addition and spread within a few 100 ms suggesting that the DNA ejection had started. The ejected DNA adopted a relaxed random-coil conformation and appeared extended upon applying a hydrodynamic flow. DNA ejection was not observed in the absence of FhuA. Fig. 6.7 (b) shows a typical picture taken about 2 min after the addition of FhuA. Almost all phage particles had started to eject their DNA but the pattern of ejection differed from one phage to the other. Some phages had released their DNA completely appearing as faint white spots. The DNA of other phages remained attached to the particles. The length of those

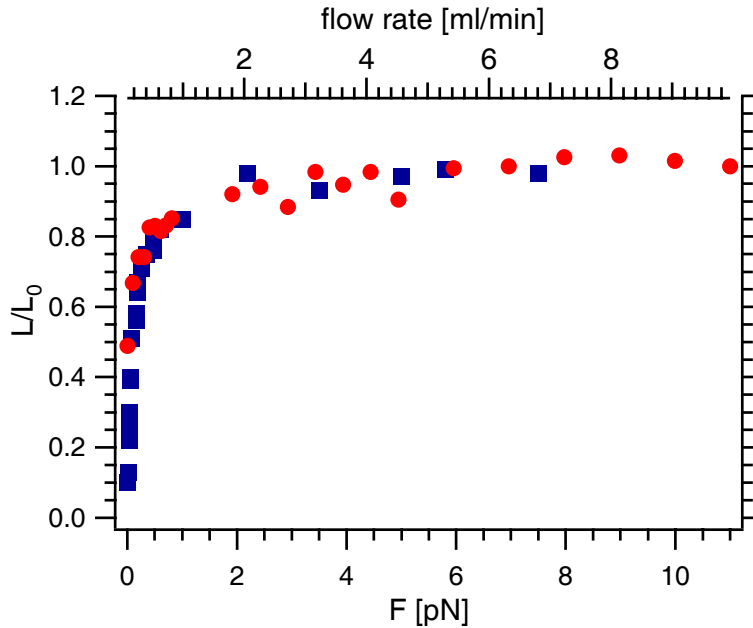


Figure 6.6: Estimation of the applied force: The relative extension of a partly ejected DNA molecule is plotted versus the flow rate (red dots). The curve overlaps with the force-extension curve shown in Strick et al. [88] (blue squares). Therefore the flow rate can now be mapped to a corresponding force.

still attached DNA molecules varied with time and from particle to particle. Fig. 6.7 (a) shows a typical sequence of events observed on one phage particle. Time resolved observations showed that about 25% of the phage particles had released their DNA within the first minute. The DNA of the other phages remained attached to the particles and was ejected in discrete steps. Typical length versus time profiles recorded during 200 s are presented in Fig. 6.8. The attached DNA was ejected in either three steps (Fig. 6.7 (a)) or one to two steps (Fig. 6.7 (b)). The duration of the pauses differed from phage to phage but in all cases the transition from one stage to the next took place in less than 750 ms which is the lower limit of the time between our two images. The ejection rate can be estimated to be as high as 75 kbp/s using the one-step ejection profile seen in Fig. 6.8 (b). The heterogeneity in the number of steps, duration of the pauses, and consequently in the length distribution was not caused by YO-PRO-1 as control experiments showed the same characteristics when the dye was added directly before taking a picture. Moreover, those DNA strands that were attached to the phage particles remained attached for more than one hour implying that they did not break due to the exciting beam. They also resisted back and forth stretching under flows as high as 10 ml/min (i.e. forces in the order of 10 pN) without changing their length or being detached from the phage particle (data not shown). The same discrete lengths were observed at 37°C, indicating that the stepwise ejection was not due to a specific effect of temperature (data not shown).

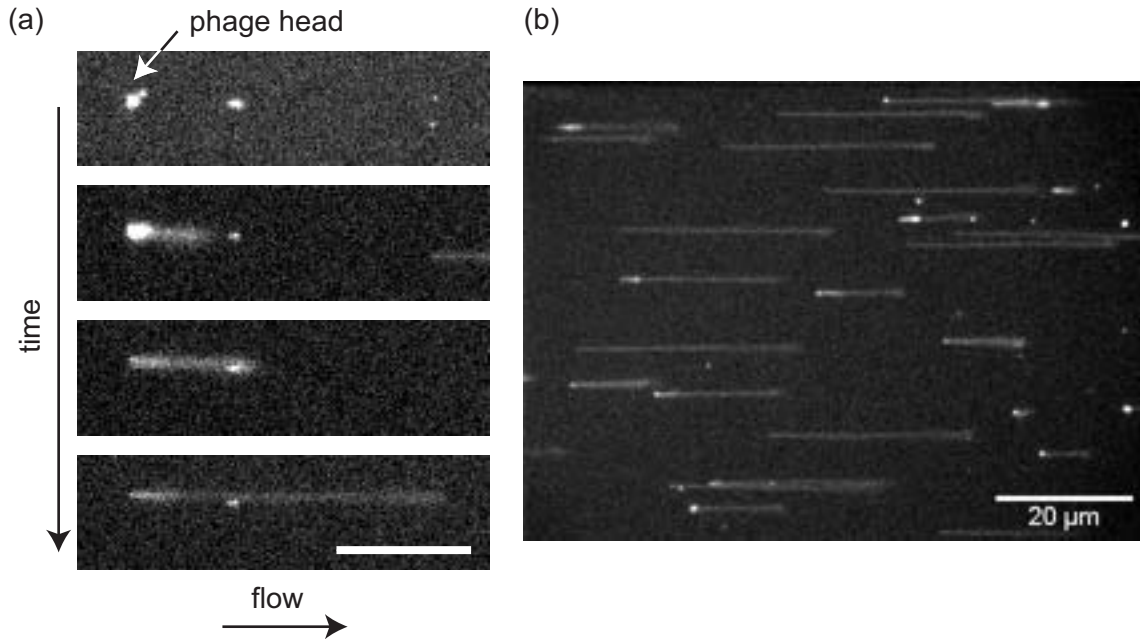


Figure 6.7: Time Evolution of DNA ejection: (a) First image: single T5 phage particle before addition of FhuA. Second image: DNA stretched to the right after the first part of the DNA is ejected. Third image: DNA after the second step in DNA ejection. Last image: DNA after the third step. The white scale bar represents $10 \mu\text{m}$. (b) Typical image of phage particles during the ejection process. The image shows clearly that DNA molecules of different discrete lengths are ejected.

6.4.2 Length Distribution of the Ejected DNA

DNA lengths were measured on more than 350 DNA strands over a period of one hour resulting in the histogram shown in Fig. 6.9 (a). Values of the lengths were calculated with corrections made due to the intercalating dye and the low flow velocity. The lengths of the ejected DNA were not homogeneously distributed but showed distinct peaks around certain lengths. The positions of those peaks were determined by fitting Gaussian curves to the data. The peaks were centered around 4.2 ± 1.2 , 5.6 ± 0.12 , 10.9 ± 0.9 , 21.8 ± 3 , $26.8 \pm 1.5 \mu\text{m}$, see also table 6.1. For comparison Fig. 6.9 (b) shows the distribution of the ejected DNA lengths of T5 st(0), a heat stable mutant, which is missing a region of 8000 bp located approximately between 22% and 33% of the genome [89]. This distribution shows also discrete peaks in the length distribution located at 4.5 ± 1 , 7.3 ± 0.2 , 11.8 ± 0.3 , 20.4 ± 1 , and $23.7 \pm 1 \mu\text{m}$ (s. table 6.1). We further analyzed the distribution of these lengths as a function of time (Fig. 6.10). From the three histograms at 1 min, 20 min, 60 min it is clearly seen that the number of phages which had ejected a short part of its DNA decreases with time while the amount of phages that had ejected their DNA to about $27 \mu\text{m}$ length increases. To obtain more quantitative information about this process, we counted (1) the number of particles on

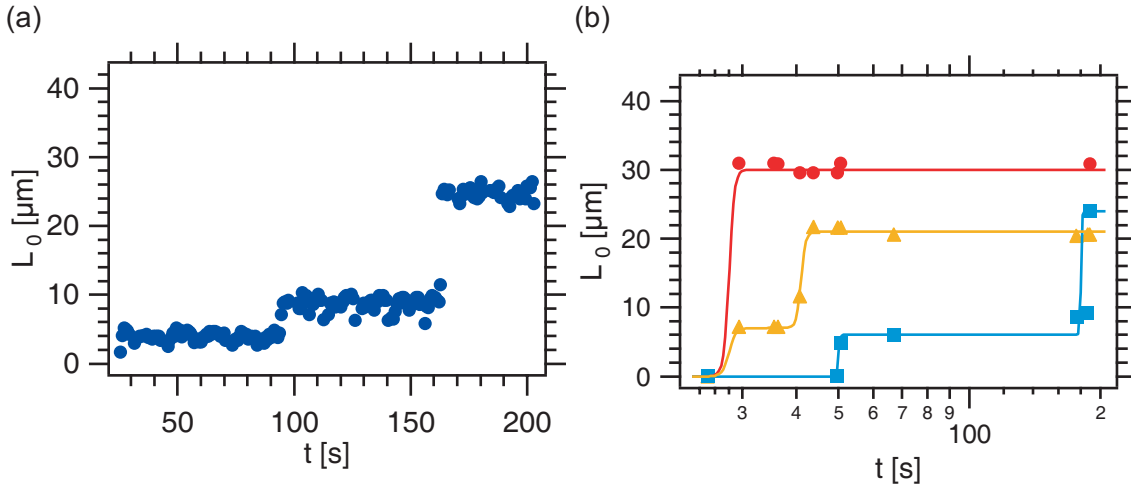


Figure 6.8: Length of ejected DNA versus time: (a) The ejected DNA length of a phage that shows three pauses at three discrete lengths and remains attached to the phage head until the end of the observation time. (b) The ejection process of three representative phage particles is displayed showing one or two steps.

which the DNA was still attached and the length of the DNA strands and (2) the number of faint stained spots corresponding to the phages that had ejected their DNA; because the released DNA was dragged along with the buffer, we could only estimate that the length of the ejected DNA corresponded to the whole genome ($41.2 \mu\text{m}$). 80 to 120 different phage particles were used to create the category plot for each time [Fig. 6.11]. From these data, we deduced that 43%, 77%, and 90% of the whole T5 genome was ejected to $27 \mu\text{m}$ or completely released after 1 min, 20 min, and 60 min, respectively.

Why did the DNA ejection transiently stop at defined positions of the genome? An unusual feature of phage T5 is the existence of genetically defined single-stranded interruptions (nicks) in one of the DNA strands. They are positioned at 7.9%, 18.5%, 32.6%, 45.3%, and 64.8% of the whole genome starting at its left end (reviewed in [90]). This corresponds to DNA lengths of 3.3, 7.6, 13.4, 18.7 and $26.7 \mu\text{m}$ if one assumes that the length of the full genome is $41.2 \mu\text{m}$ (s. table 6.1). The positions of the peaks of the histogram of the length of ejected DNA and the fact that the left end of the DNA is always ejected first [91, 92, 93] suggest that the pauses in the DNA ejection occur in the vicinity of the DNA nicks. This is shown in Fig. 6.9 (a) where the arrows indicate the positions of the nicks in the phage DNA. To test this proposal, we reproduced the above experiments with phage T5 st(0), which is missing the nick located at 32.6% of the genome because of the deletion of a region of 8000 bp located approximately between 22% and 33% of the genome. The histogram presented in Fig. 6.9 (b) shows that DNA ejection from T5 st(0) also occurred in steps. The positions of the first three peaks were very similar to that of the T5 (wt) in agreement with the fact that this part of the genome is located upstream of the deletion (GenBank accession numbers AY 692264 and NC

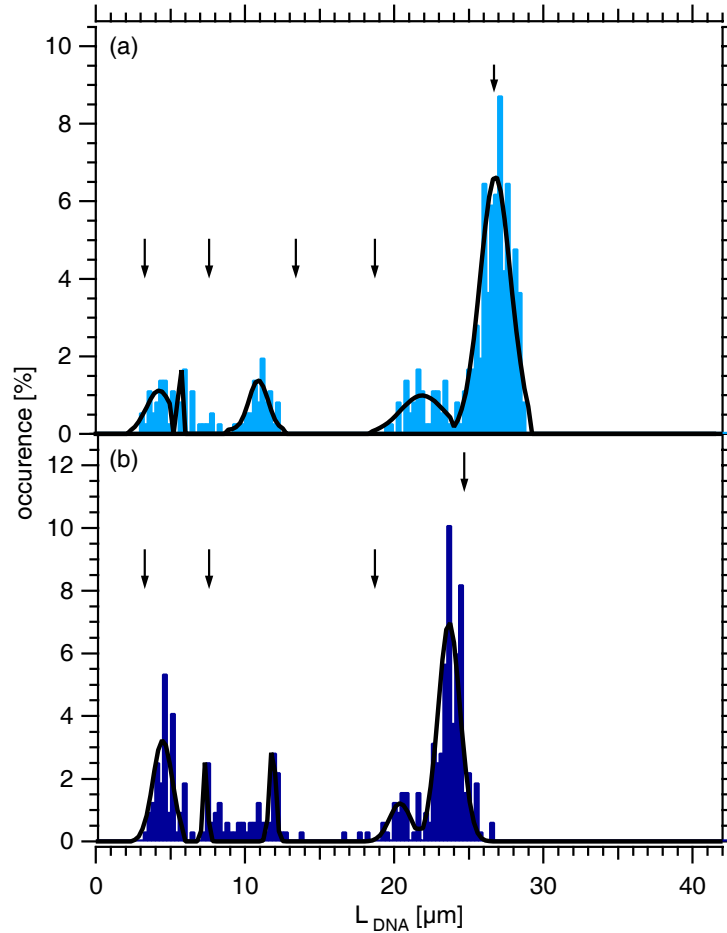


Figure 6.9: Distribution of the ejected DNA length: Amount of DNA at a certain length for (a) wild type phage (b) mutant phage. Discrete peaks are clearly distinguishable.

005859). On the other hand, the Gaussian curves of the two longest DNA strands, which are located downstream of the deletion were shifted by $2.5 \mu\text{m}$ corresponding to 7400 bp. This agrees well with the introduced shortening by 8000 bp ($2.7 \mu\text{m}$) which supports our proposal that the pauses in ejection correlate with the presence of nicks in the phage DNA. The peak and nick positions are summarized in table 6.1.

6.5 Discussion and Conclusion

For the first time, the data presented here has provided an insight into the receptor-triggered DNA ejection process at a single phage particle level. This study has revealed that the ejection process is unexpectedly complex. Some phages released their whole

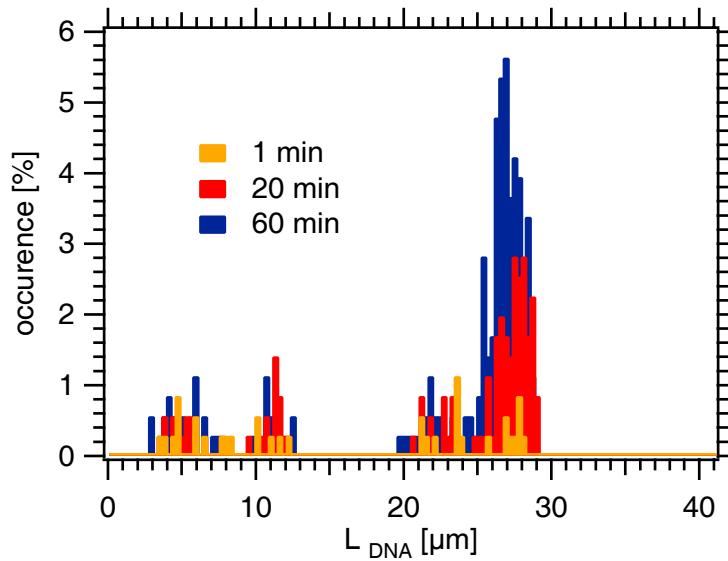


Figure 6.10: Development of the size distribution of the ejected DNA with time: The peak heights at small DNA sizes were reduced with time while at larger DNA sizes the peak heights increased.

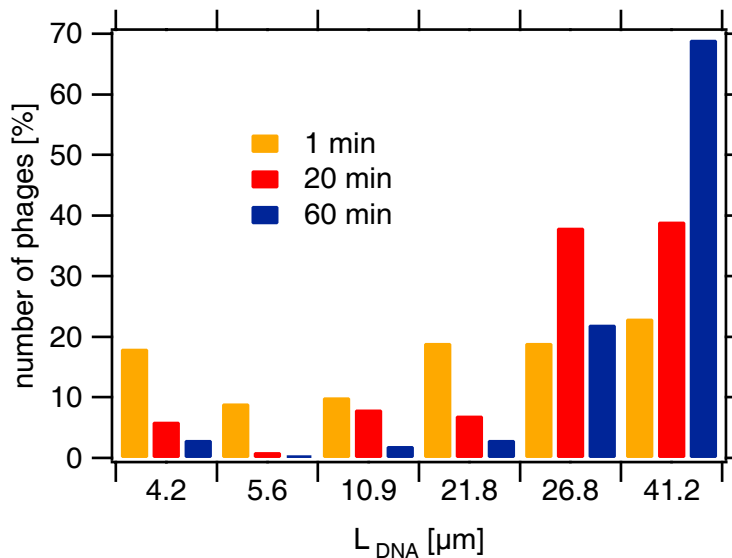


Figure 6.11: The number of phages with a certain ejected DNA length divided by the total number of phages counted at 1 min, 20 min, 60 min. The number of phages with small ejected DNA sizes decreased with time while the total number of DNA with sizes of 26.8 and 41.2 μm increased.

genome in one step without pausing after receptor binding. For all other phages, the ejection proceeded in a stepwise manner with pauses at certain discrete lengths. The rate of ejection in between the steps is estimated to be 75 kbp/s. Ejection was reproducibly

phage		pos. 1 [μm]	pos. 2 [μm]	pos. 3 [μm]	pos. 4 [μm]	pos. 5 [μm]
wt	nick	3.3	7.6	13.4	18.7	26.7
	peak	4.2	5.6	10.9	21.8	26.8
st(0)	nick	3.3	7.6	-	16	24
	peak	4.5	7.3	11.8	20.4	23.7

Table 6.1: Position of nicks and peaks along the T5 wt and T5 st(0) DNA.

stopped at defined positions of the genome at various times. The stepwise ejection was not an artifact of the labeling dye used because pauses also occurred when the dye was added right before observation a long time after addition of the receptor protein. The attachment of the particles to the COC foil of the microfluidic chamber or the applied flow could lead to this exceptional behavior of the T5 particles. To test this, DNA ejection was independently measured by light scattering on T5 populations in bulk solution. For the analysis of the complex shape of the kinetics one had to assume that the DNA ejection occurred in multisteps [94].

The ejection speed $v = 75 \text{ kbp/s}$ allows us to estimate the friction coefficient β acting on the DNA during the ejection process. The force F driving DNA out of a viral capsid at a velocity v was measured to be of the order of 10 pN [3, 5]. The friction coefficient β is derived to be $\beta = F/v$ of order $\beta = 4 \times 10^{-7} \text{ Ns/m}$. We now assume that the viral stalk is the bottleneck during the ejection process. We estimate the resulting friction coefficient with a simple model: a cylindrical piston (DNA) with radius r and length L is pushed through a hollow tube (viral stalk). The piston and the inner wall are separated by a thin lubricating film of thickness d and surface area $A = 2\pi rL$. In this case β is given by $\beta = \eta A/d$, where η denotes the viscosity of the lubricating film. With $\eta = 10^{-3} \text{ kg/ms}$ for water, $r = 1 \text{ nm}$, $L = 200 \text{ nm}$, and $d = 0.5 \text{ nm}$ we expect β to be of order $\beta \sim 3 \times 10^{-9} \text{ Ns/m}$ which is two order of magnitude smaller than measured. We therefore conclude that the friction in the stalk is negligible. Rather the uncoiling of the tightly packed DNA inside the phage head dominates the initial ejection rate.

We found a reasonable correlation between the positions at which the DNA stopped during ejection and the locations of single-stranded interruptions on the DNA suggesting that these nicks could be involved in the pauses. The basepair sequence surrounding most of the nicks is GCGC [95]. This sequence clearly does not suffice to define the position of a nick because the T5 genome contains roughly 240 such sequences. Even the recent complete sequencing of the T5 wt and T5 st(0) genomes has not allowed the identification of specific sequences at the location of the nicks. How could the nicks lead to pauses in the ejection process? Interestingly, it was shown that the introduction of a single single-stranded interruption in a 139 bp DNA duplex was sufficient to cause local flexibility of the DNA, which adopted a V-shape rather than a straight configuration as observed with electron microscopy [96].

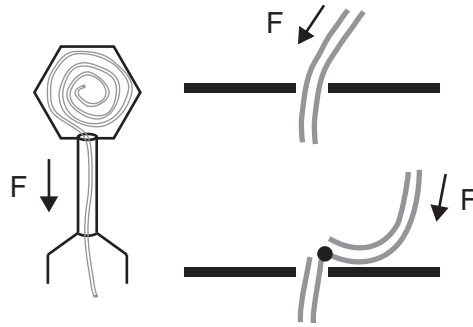


Figure 6.12: DNA buckling induced by a single stranded nick in the DNA (a) dsDNA pushed through a small channel (b) dsDNA with a nick pushed through a small channel.

Therefore, we propose that nicks in the T5 DNA involve a particular arrangement of the DNA that represents an energetic barrier to the ejection process. The flexibility introduced by the nick may result in the buckling of the DNA during its passage through the inside of the connector or the tail (see Fig. 6.12). As a consequence, the translocation is inhibited unless thermal motion lifts the DNA strand into a parallel orientation with respect to the tail. The stepwise DNA ejection process would therefore reflect similar events whether it occurred in one, two, or three steps.

Why did most phages remain only a short time (~ 1 min) at a stage where they had ejected the shortest DNA length and up to 20 min and even one hour at a stage where the longest DNA strands were ejected? It has been observed that the force resisting DNA entry during packaging increased sharply after loading about $3/4$ of the genome [8, 3]. It was further postulated that the reverse situation occurred during ejection: the force will drop quickly as soon as a small fraction of the DNA chain is released. In agreement with this proposal, it has been shown that the extent of in vitro ejection of the DNA of the phage λ can be controlled by varying the osmotic pressure outside the capsid [97]. Such pressure dependence was also observed for T5 phages (P. Tavares et al., submitted). If T5 DNA ejection was indeed dependent on the difference between the inside and outside pressure a different scenario would occur. Complete ejection would occur for those phages that eject their DNA without being stopped at the nicks: this corresponds to free DNA found in the bulk solution of the microfluidic chamber. For the phages whose ejection process was stopped at a nick position, the remaining internal pressure is sufficient to overcome the energy barrier of the first nicks. Ejection remains blocked for longer times at the last nicks because the pressure inside the capsid is insufficient. In support of this proposal, de Frutos et al. [94] recently suggested a kinetic model based on light scattering experiments that allowed to determine the characteristic times required to pass from one state of the T5 phage ejection process to the next. The probability for switching to the next stage depended on the DNA length still remaining inside the capsid. Therefore a longer time was required to transfer the last fraction of

DNA remaining in the capsid.

The physiological role of the nicks is still not elucidated. The conformation of the DNA at the nicks may contribute to the formation of protein-DNA complexes required for optimal viral development. Alternatively, the stop sites may be involved in regulating DNA transfer *in vivo*. It is unique among phages that the T5 phage transfers its DNA in two steps *in vivo*. The first 8% of the DNA (First Step Transfer DNA or FST DNA) enters the cytoplasm. Proteins synthesis directed by this part of the DNA is required for the subsequent transfer of the remaining DNA in the second step transfer (SST) process [8]. It is thus tempting to correlate the *in vitro* arrests to *in vivo* events. However, phage mutants have been isolated that are apparently free from single-stranded interruptions and still inject their DNA in two steps [98]. Whether such nickless mutants would eject their DNA *in vitro* in one or several steps remains an open question.

This single particle study clearly shows that DNA ejection from phage T5 is a complex process. The recent sequencing of the phage T5 genome should help to elucidate some of its singularities. It remains to be determined whether such complexity is also observed in other tailed phages.

6.6 Outlook

This study succeeded to visualize the T5 ejection process for the first time. A lot of optimization of the experimental conditions was necessary to achieve this. A future goal is to improve the length distribution histogram to prove the correlation between the nicks in the phage DNA and the DNA length. Additionally, the time resolution which was limited to 700 ms because of the low signal to noise ratio needs to be enhanced to determine exactly the ejection speed in between steps.

To realize these two goals, it is essential that the signal to noise ratio is improved. This can be implemented by using free-radical scavengers such as ascorbic acid. Of course, it is necessary to ensure that those anti-fade solutions do not interfere with the ejection process. Additionally, the signal to noise ratio could be enhanced using an intensified camera.

By replacing the peristaltic pump used here with a syringe pump the flow velocity should be more constant which should reduce the observed cyclic dynamics of the DNA molecules. Unfortunately, the tumbling motion can not be completely avoided this way because it is an intrinsic process of a polymer in shear flow (s. chapter 3.2.2). Even so a syringe pump should lead to a better approximation of the ejected DNA length.

An alternative experimental setup could be used to avoid the tumbling motion altogether. Single phage particles are adsorbed to a COC coated diamagnetic beads trapped in a laser trap and moving at a constant velocity through the bulk solution. This way

it is possible to expose the phages to a uniform flow instead of a shear flow. This setup resembles the one used in [15]. The uniform flow would not lead to a cyclic motion of the DNA thereby simplifying the exact determination of the DNA contour length. Of course, this approach is very time consuming if one aims for statistics. On the other hand, this setup allows to measure additionally the force that keeps the DNA inside the head during the pauses of ejection: The partially ejected DNA of a phage particles adsorbed to a COC coated bead is attached to a static surface, e.g. via sulfur bonds to a gold electrode. The remaining DNA is pulled out of the phage head by exerting a force to the bead in the laser trap.

To prove the assumption that the nicks are somehow responsible for the stepwise ejection could be easily tested by repeating the experiment with a nick-deficient mutant. The ejection is expected to be complete for such mutants if the nicks determine the pauses.

The experimental setup used in this study should be easily adaptable to different phages, e.g. λ -phage, by adding the receptor protein LamB. Comparative studies of the ejection process of different phages are therefore feasible.

7 Structure and Fluidity of Lipid Membranes Supported on the Thermoplastic COC

7.1 Introduction

Cells are surrounded by a plasma membrane which protects the cell interior from its environment while still transducing signals necessary for cell functioning. Proteins in the intercellular space and sugar moieties protruding from neighboring cells interact constantly with the cell membrane, inducing a proper reaction of the cell to its environment. Many processes within cells such as cellular respiration require biomembranes. It is therefore necessary to understand how biomembranes work if one is interested in understanding biological processes in cells. Biomembranes consist mainly of a fluid lipid bilayer with a great variety of different proteins and peptides incorporated and attached [64]. For this reason simplified model systems such as liposomes, lipid bilayer stacks, and black lipid membranes have been studied. Solid supported fluid lipid bilayers [32] serve as one of the most important model systems for cell membranes because they allow the application of several surface sensitive techniques such as ellipsometry, surface plasmon spectroscopy, atomic force microscopy (AFM) [25], and neutron and x-ray reflectivity [99, 100]. Neutron and x-ray reflectivity are powerful tools to investigate soft condensed matter systems at interfaces. Neutron reflectivity allows to vary the contrast by isotopic substitution while it is possible to measure up to higher momentum transfer with x-ray reflectivity used in our study. Hence, structural details of membranes on a solid support may be obtained which are not accessible to this extent for other model systems.

Supported membranes represent an effective way of generating biofunctional surfaces, e.g. for biosensor applications [24, 101]. Furthermore, supported fluid positively charged membranes may be used for the manipulation of single biomolecules such as DNA [102, 103, 104].

The fluidity of the membrane is a basic requirement for mimicking functional membranes [32]. Hence, the proper choice of the supporting substrate is crucial to ensure a fluid supported membrane. Standard supports, including glass cover slides [105], quartz substrates [106], oxidized silicon wafers [107, 108], and mica [109], are hydrophilic and

negatively charged. The charge density and the surface chemistry are highly dependent on the cleaning procedure and change with time. Surface modification and structuring is time consuming and often needs clean room equipment. Plastic materials can be easily formed at low cost to the manifold shapes to comply with the different needs. For technical and industrial applications it is therefore appealing to use plastic materials as support. Studies of the behavior of lipid membranes supported to plastic material such as Poly(dimethylsiloxane) (PDMS) [33] and Polystyrene (PS) [34] have been performed previously indicating that fluid membranes can also be formed on plastic supports.

Here, the hydrophobic copolymer 2-norbornene ethylene ("cyclic olefin copolymer", COC) is studied because of its good optical properties. COC promises to be a very useful plastic material since COC is inert against most acids, basis and polar solvents, and it does not swell in water [72]. Its surface chemistry is robust, e.g. it is independent of the cleaning procedure used and does not vary after exposure to air due to aging effects. Also, COC is basically uncharged. Its high optical transmission, its low amount of inclusions, and low autofluorescence [23] make it well suited for high resolution fluorescence microscopy. Various kinds of functional microfluidic chambers can be formed out of this material by injection molding, nanoimprinting [73] and surface functionalization [110].

In this section, we study the homogeneity, fluidity, and the structure of cationic DOTAP/zwitterionic DOPC lipid layers supported on COC. We have chosen DOTAP/DOPC mixtures as these lipids were well characterized in previous studies [111, 112, 113, 114, 19]. Two preparation methods were compared, the well-established vesicle fusion method [115] and the method of solvent exchange [116]. First, the homogeneity and fluidity of the supported membranes were characterized optically with fluorescence microscopy, continuous bleaching and fluorescence recovery after photobleaching. Finally, the structure of COC-supported DOPC membranes was resolved by x-ray reflectivity and the results are discussed.

7.2 Results

7.2.1 Homogeneity and Fluidity of the Lipid Layers

Lipid DOPC membranes mixed with 0% to 100% DOTAP were prepared on COC by vesicle fusion and solvent exchange.

The optical homogeneity of all lipid layers was checked repeatedly for each preparation using fluorescence microscopy. In all cases, the membranes were found to be homogeneous independent of the lipid composition and preparation technique. Increasing the salt content up to 150 mM did not alter the membrane appearance. The same held true

exponential decay to determine the bleaching constant b [Fig. 7.1 (d)]. Line profiles were extracted for each image. Fig. 7.1 (e) includes every 4th line profile up to 100 s. The first curves show a more or less flat intensity profile. With time, a pronounced exponential decrease at the periphery developed.

To test for the homogeneity of the illumination, the diffusion constant was determined on both sides of the illuminated area (left-right). The two calculated diffusion constants coincided for truly homogeneous illumination. All lipid layers displayed a diffusion constant of around $2 \pm 1 \mu\text{m}^2/\text{s}$ which is in the order of magnitude expected for a fluid membrane [117, 118]. This proves that the lipids form a continuous lipid membrane on COC rather than sticking to the plastic surface in an irregular fashion.

In summary, the Continuous Bleaching method made it possible to estimate the integrity and fluidity of supported membranes prepared on COC easily and quickly. Furthermore Fluorescence Recovery After Photobleaching (FRAP) experiments were performed to quantify whether the diffusion constant depends on the lipid composition beyond the limited sensitivity of the Continuous Bleaching method.

For each membrane at least 5 independent measurements on different spots were performed to determine the mean value and the standard deviation of the diffusion constant D and the mobile fraction M . Typical measurements are shown in Fig. 7.2. All membranes had mobile fractions above 98%. The average diffusion constant of all membranes prepared by vesicle fusion and by solvent exchange except 100% DOTAP prepared by solvent exchange was calculated to be $0.83 \mu\text{m}^2/\text{s}$. The diffusion constant D of the membranes prepared by vesicle fusion [Fig. 7.3] exhibits almost no dependence on the amount of cationic lipids and it is approximately $0.73 \mu\text{m}^2/\text{s}$. This is in striking contrast to results obtained on glass surfaces where the diffusion constant depended strongly on the amount of charged lipids in the membrane and on the detailed cleaning procedure (data not shown). Only for solvent exchange preparation did the diffusion constant of the 100% DOTAP ($D = 0.38 \mu\text{m}^2/\text{s}$) deviate clearly from the average of the other lipid mixtures prepared by solvent exchange ($D = 0.88 \mu\text{m}^2/\text{s}$). This was validated for several independently prepared membranes, and the origin of this behavior will be discussed below.

7.2.2 Structure of the Lipid Layer

To probe the structure of the lipid membranes supported on COC, x-ray reflectivity experiments on DOPC membranes obtained by both preparation techniques were performed.

To characterize the bare polymer surface, first the oxide terminated silicon wafer with the spin coated COC layer was measured in air [Fig. 7.4 (a), orange dots] and in contact with water [Fig. 7.4 (a), red dots], using a microfluidic setup [70]. The air-COC-silicon

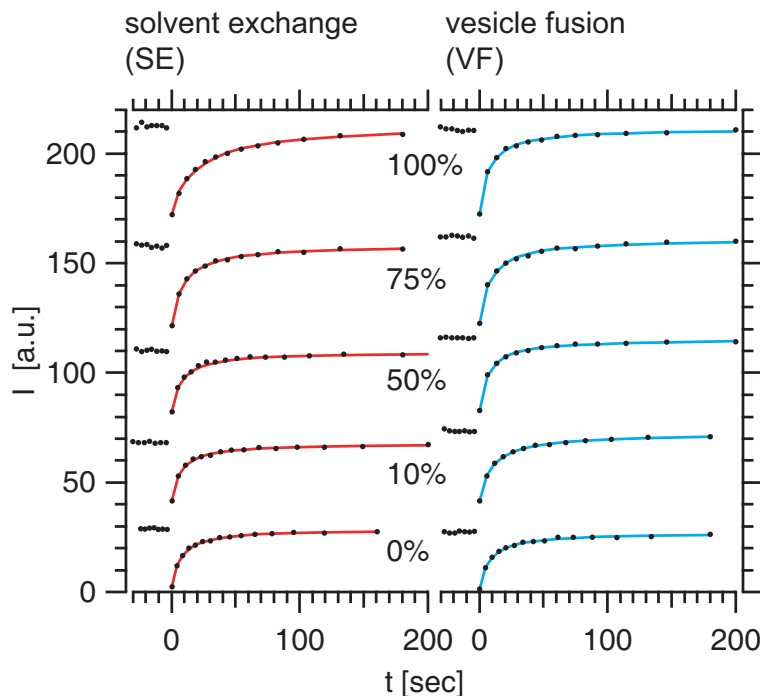


Figure 7.2: FRAP: Typical FRAP measurements for membranes prepared by solvent exchange (SE, curves on the left) and by vesicle fusion (VF, curves on the right). The measured intensity is plotted vs. time (black dots), the fit is shown as a red line (solvent exchange) or blue line (vesicle fusion). From top to bottom the DOTAP percentage in the membranes decreases from 100% to 0%.

oxide system exhibits a high contrast in electron density, therefore the x-ray intensity oscillations occurring in the reflectivity curve of the COC layer had a large amplitude. When water was filled into the chamber, the loss of contrast at the water-COC interface reduced the oscillations. At the same time, the critical angle shifts from 0.09° to 0.06° while the shape of the curve remained unchanged.

Both curves (air and water) can be fitted very nicely with a box model shown in Fig. 7.4 (b) where the electron density of silicon and air/water are known [119] and the electron density, the thickness of the COC layer and the surface roughnesses are free fitting parameters. Thus, the main information obtained is the electron density of the COC layer ($\rho = 0.24 \text{ e}^-/\text{\AA}^3$), the COC layer thickness ($\sim 450 \text{ \AA}$), and the COC surface roughness ($\sigma = 7 \text{ \AA}$), all of which do not change significantly in the presence of water. The resulting modeled reflectivity curves are displayed in Fig. 7.4 (a) as solid lines overlaying the original data.

The shape of the reflectivity curve changed qualitatively when a DOPC layer was prepared on the COC film by vesicle fusion [Fig. 7.4 (a) light blue dots]. The corresponding x-ray intensity curve exhibits a beating effect, indicating that additional layers are

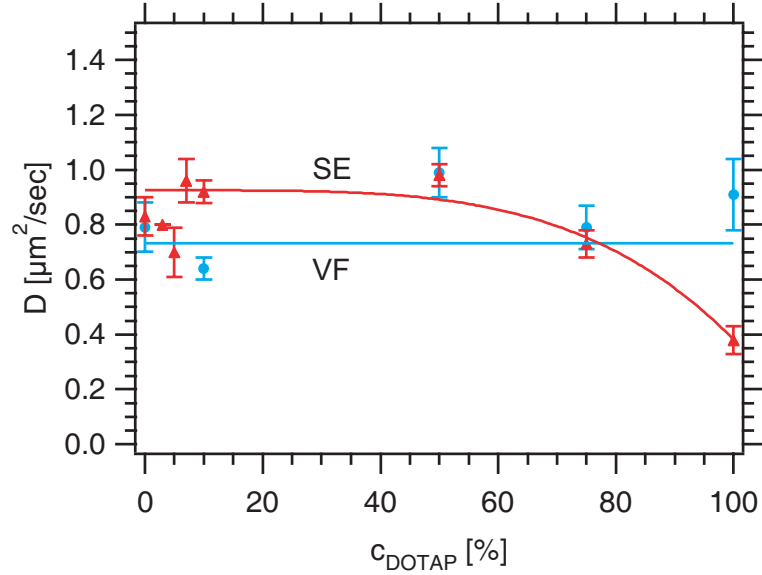


Figure 7.3: FRAP: Diffusion constant of the lipid membrane prepared by vesicle fusion (blue dots) and solvent exchange (red triangles) vs. content of cationic DOTAP. The blue line shows the average diffusion constant of the membranes prepared by vesicle fusion. The orange curve represents an estimation for the evolution of the diffusion constant for membranes assembled by solvent exchange using the ansatz $D [\mu\text{m}^2/\text{s}] = 0.93 - 5.4 \cdot 10^{-9} c_{\text{DOTAP}}^4 [\%]$.

present. In fact, the data can be described well by introducing two additional electron density boxes representing lipid headgroups and a box with a low electron density representing the lipid tails [Fig. 7.4 (a + b), blue curves], i.e. a lipid bilayer. The head-to-head distance was found to be $d_{hh} = 29 \text{ \AA}$ (s. table 7.1). An explanation as to why these measured data deviate from literature values of free or supported bilayer will be given in the discussion.

In order to explore whether the observation of a lipid bilayer on a hydrophobic support is unique to COC polymer surfaces, we have also prepared a lipid membrane on hydrogen-terminated silicon (H-Si). The data is shown in Fig. 7.5 as black dots.

Finally, a control experiment was carried out with a DOPC membrane deposited on a silicon wafer covered by an oxide layer (SiOx) (Fig. 7.5 red dots). The reflectivity curves of the SiOx and the H-Si supported membranes can be fitted by a bilayer model. The resulting electron density profiles are shown in the inset. The resulting electron densities of the lipid heads ρ_h are found to be $0.43 \text{ e}^-/\text{\AA}^3$ and $0.46 \text{ e}^-/\text{\AA}^3$ for H-Si and SiOx respectively (s. table 7.1). The electron densities of the lipid tails ρ_t coincide at $0.30 \text{ e}^-/\text{\AA}^3$ for both supports. The head-to-head distance d_{hh} is given by 40 \AA and 36 \AA for H-Si and SiOx respectively (s. table 7.1).

To test the influence of the deposition method, we performed reflectivity measurements

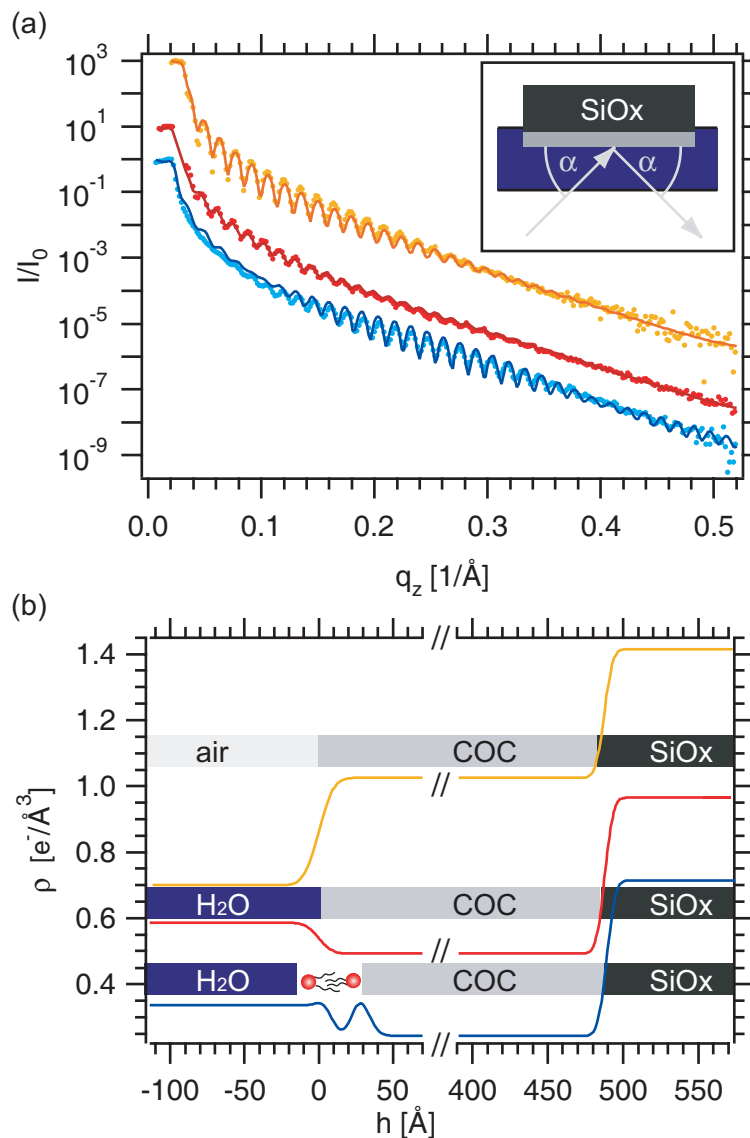


Figure 7.4: X-Ray Data: (a) Reflectivity curves of a uniform COC film exposed to air (orange dots), to water (red squares) and with a DOPC layer prepared by vesicle fusion (light blue triangles). Fits to the different curves are included as solid lines in the same color shaded slightly darker. The reflectivity curves are shifted vertically for clarity. The inset illustrates the setup used during reflectivity measurements. (b) The electron density profiles corresponding to the fits in (a) are plotted. The profile for the COC layer on air is shown as an orange line, the profile for the COC layer under water is displayed as a red line, and the profile of a COC layer with a lipid membrane on top is depicted with a blue line. The profiles are shifted vertically for clarity. A cartoon illuminating the physical meaning of the electron density profile is placed on top of each profile.

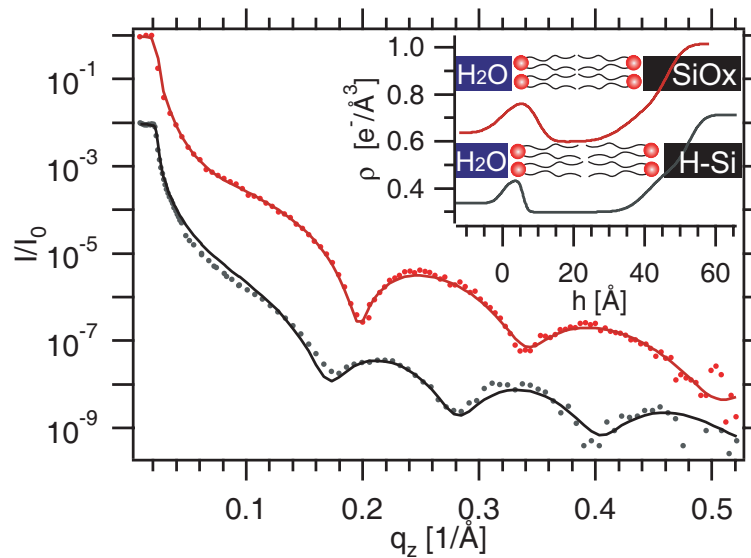


Figure 7.5: DOPC membranes on SiOx and H-Si: The reflectivity curve of a lipid layer on the hydrophilic SiOx (red circles) and the best fit (dark red line) is shown. Displaced vertically is the reflectivity curve of a membrane on the hydrophobic H-Si (grey dots) with the best fit (black line). The profiles corresponding to the fits are shown in the inset in the upper right corner. A schematic drawing above the profiles illustrates the interpretation of the box models.

on a DOPC membrane deposited on COC by solvent exchange. The measurements on the lipid membrane prepared by vesicle fusion (light blue dots) and by solvent exchange (red dots) are compared in Fig. 7.6. For the membrane prepared by solvent exchange, a reduced amplitude of the oscillations was observed. Again, a bilayer model fits best to the data, indicating that qualitatively, the bilayer formation was not dependent on the preparation method. However the electron density contrast was clearly reduced ($\rho_h = 0.33 e^-/\text{\AA}^3$ and $\rho_t = 0.29 e^-/\text{\AA}^3$). The reason for this is elucidated in the discussion. The head-to-head distance is $d_{hh} = 27 \text{\AA}$.

7.3 Discussion

7.3.1 Homogeneity and Fluidity

On hydrophilic supports such as glass cover slides, a change in temperature or salt concentration may result in membrane defects visible with fluorescence microscopy. It is known that the diffusion constant of glass-supported membranes shows a strong dependence on the cleaning procedure [118]. The conformation of a lipid membrane supported by COC seems more stable and less dependent on solvent and temperature conditions

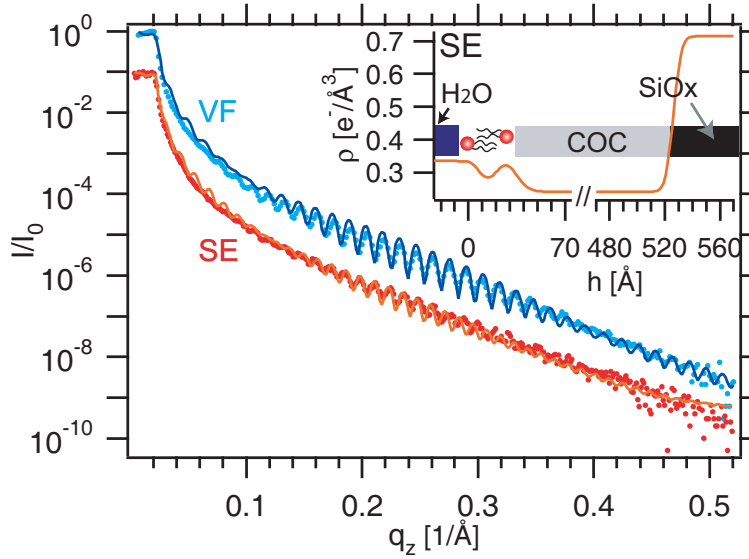


Figure 7.6: X-Ray Reflectivity: The reflectivity curves of DOPC lipid layers prepared by vesicle fusion (VF) and solvent exchange (SE). The fits are included as full lines in the same color shaded darker. The inset shows the electron density profile of the sample prepared by solvent exchange.

as defect formation has not been observed during this study and the diffusion constant does not depend on the amount of charge in the membrane. This stability is of practical relevance.

It can be ruled out that the lipids adsorb to the surface as vesicles because our Continuous Bleaching and FRAP experiments probed the mobility of the lipid membrane on the length scale of a few μm .

The diffusion constants measured with FRAP in this work ($0.8 \mu\text{m}^2/\text{s}$) is very similar to the diffusion constant ($0.9 \mu\text{m}^2/\text{s}$) measured by Lenz et al. [33] for a POPC lipid membrane on hydrophobic Polydimethylsiloxane (PDMS) surfaces. POPC is similar to DOPC except one fatty acid chain is shorter and has no double bond (16:0). Also, FRAP measurements showed no dependence of the diffusion constant on the lipid composition for membranes on COC prepared by vesicle fusion. The same holds true for membranes prepared by solvent exchange up to a DOTAP ratio of 75%. This is explained by the hydrophobic surface being uncharged and therefore the electrostatic interactions between the lipid membrane and the substrate being reduced compared to glass surfaces. Only the diffusion constant of membranes composed of 100% DOTAP prepared by solvent exchange differed notably from all others. It is likely that during the preparation process by solvent exchange some amphiphilic 2-propanol stays intercalated in the membrane [120, 121]. This effect could increase for charged lipids which could lead to the formation of small defects (below the resolution of optical microscopy) in the membrane. Such defects reduce the diffusion constant significantly.

7.3.2 Structure

COC represents a highly hydrophobic substrate (contact angle = 89° [110]). Because of hydrophobic effects one might expect that lipids form a monolayer on hydrophobic substrates with the lipid tails facing towards the substrate. A clear reduction of the number of lipids in membranes deposited on hydrophobic substrates has been reported before [33, 34, 35]. In detail, Lenz et al. [33] found a factor of two between the two fluorescence intensities of a lipid membrane on hydrophobic and oxidized (hydrophilic) PDMS. Elliot et al. [34] compared the fluorescence intensity of lipid membranes on polystyrene films with equivalent membranes on glass surfaces and counted the single fluorescence events with fluorescence correlation spectroscopy. Retzinger et al. [35] counted the radioactivity of radioactively labelled lipids on polystyrene-divinylbenzene beads. These experiments have taken the reduced number of lipids as an indication for monolayer formation. Naturally, the total amount of lipids in a monolayer is only half of that in a compact bilayer. Our experiments suggest a different interpretation. We argue that the reduction of the number of lipids on hydrophobic supports may not be due to formation of a compact monolayer but at least in the case of COC due to the formation of a thinned, less densely packed bilayer as we will show in the following discussion of the x-ray data.

To emphasize details of the reflectivity curve, the measured reflectivity curve of the lipid layer is divided by the Fresnel reflectivity ($1/q^4$) and displayed in Fig. 7.7 (a) as light blue dots (“data”). Vertically displaced is the best fit to the reflectivity curve resulting from a bilayer box model shown as a solid dark blue line (“bilayer”). The reflectivity curve resulting from the best fit using a monolayer box model is displayed stacked under it (“monolayer”). Fig. 7.7 (b) shows the associated electron density profiles. Schematic drawing are placed on top of them illustrating the physical composition of the layers. Only the section of the electron density profile in proximity to the lipid layer is displayed.

The monolayer model succeeds in imitating the amplitude and phase of the small oscillations quite well but it fails to show the beating effect. In contrast, the bilayer model fits the oscillations reasonably including the beating well. Therefore we conclude that a bilayer is formed.

7.3.3 Details of the Bilayer Structure

The vertical head-to-head distance of the COC supported bilayer (d_{hh}) was found to be 29 \AA . This is 8 \AA and 6 \AA shorter than reported by Liu et al. [122] for DOPC multilamellar membranes on SiOx and similar measurements on DOPC/water solutions [68] respectively. In the following, we call this membrane a thinned bilayer.

The electron density of the lipid heads (ρ_h) in the thinned bilayer is reduced to $0.34 \text{ e}^-/\text{\AA}^3$, i.e. $0.1 \text{ e}^-/\text{\AA}^3$ and $0.12 \text{ e}^-/\text{\AA}^3$ smaller than reported previously [122, 68], indicating a clear reduction in the packing density of the lipids.

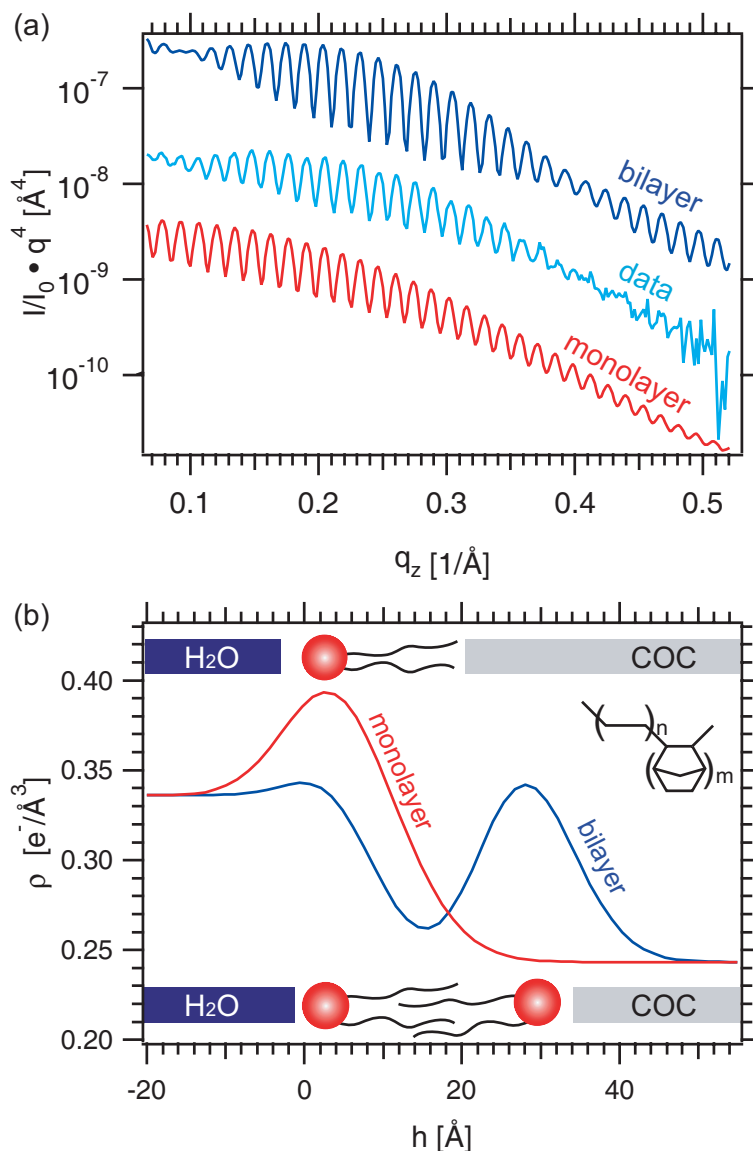


Figure 7.7: (a) The best fit to the reflectivity curve assuming a bilayer box model is displayed divided by the Fresnel reflectivity q^{-4} (dark blue solid line, “bilayer”). Stacked under it, the measured reflectivity curve (light blue solid line, “data”) is displayed. The last curve represents the best fit to the reflectivity curve using a monolayer box model (red solid line, “monolayer”). (b) The profiles corresponding to the fit curves in (a) are shown (bilayer dark blue line, monolayer red line). Schematic drawings illustrate the box models. The structure formula of COC is placed in the upper right corner.

The electron density of the lipid tails (ρ_t) in the thinned bilayer was found to be $0.26 \text{ e}^-/\text{Å}^3$. Tristram et al. [68] and Liu et al. [122] distinguish two domains in the

lipid tail region. The headgroup region is followed by a tail region with an intermediate electron density ($0.29 \text{ e}^-/\text{\AA}^3$ [122, 68]) separated from the other leaflet of the bilayer by a small region with very low electron density ($0.24 \text{ e}^-/\text{\AA}^3$ [122], $0.23 \text{ e}^-/\text{\AA}^3$ [68]). In our study, we do not distinguish between those tail regions since it is well-known that data up to $q > 0.5 \text{ \AA}^{-1}$ may not be interpreted by a too complex box model [123]. Therefore our ρ_t is in between those literature values ($\rho_t = 0.26 \text{ e}^-/\text{\AA}^3$).

Note that the lipid density of a bilayer formed on SiOx [Fig. 7.5] compares reasonably well with literature values [122, 68] (these values are summarized in Table 7.1). For a

source	support	d_{hh} [Å]	ρ_h [$\text{e}^-/\text{\AA}^3$]	ρ_t [$\text{e}^-/\text{\AA}^3$]
this work	COC (VF)	29	0.34	0.26
	COC (SE)	27	0.33	0.29
	H-Si	40	0.43	0.30
	SiOx	36	0.46	0.30
Liu et al. [122]	stacks on SiOx	37	0.44	0.24 - 0.29
Tristram-Nagle [68]	free stacks	35	0.46	0.23 - 0.29

Table 7.1: Parameters extracted from x-ray reflectivity measurements for DOPC membranes on different supports.

SiOx-supported membrane [Fig. 7.5] we obtain a head-to-head distance of $d_{hh} = 36 \text{ \AA}$, an electron density of the heads of $\rho_h = 0.46 \text{ e}^-/\text{\AA}^3$ and an electron density of the tails of $\rho_t = 0.3 \text{ e}^-/\text{\AA}^3$, in good agreement with literature values [122, 68].

Table 7.1 summarizes the head-to-head distance d_{hh} , the maximal electron density of the headgroups ρ_h , and the density of the lipid tails ρ_t on the different supports and for the different preparation techniques. Values from literature are added for comparison. A simple explanation of the reduced electron density of the thinned bilayer on COC is a reduced packing density of the lipids.

The bilayer structure found on SiOx and two different bilayer configurations in agreement with the measurements on COC are summarized in Fig. 7.8. Fig. 7.8 (a) shows the configuration of a typical bilayer as found for example on SiOx. On COC the packing density of the lipids is reduced allowing the lipid tails to relax into a more disordered conformation, see Fig. 7.8 (b). As shown in Fig. 7.8 (c), the lipid tails could also interdigitate, reducing the packing density and the bilayer thickness.

This thinned bilayer is similar to the monolayer formation found for the bipolar lipids in archae bacteria [124]. Interdigitated PC bilayers induced by traces of alcohol in the bulk solution have been reported by Mou et al. [125]. Hollinshead et al. [126] also demonstrated that lipids may interdigitate with the carbon chains of an OTS monolayer if the OTS grafting density is 60%.

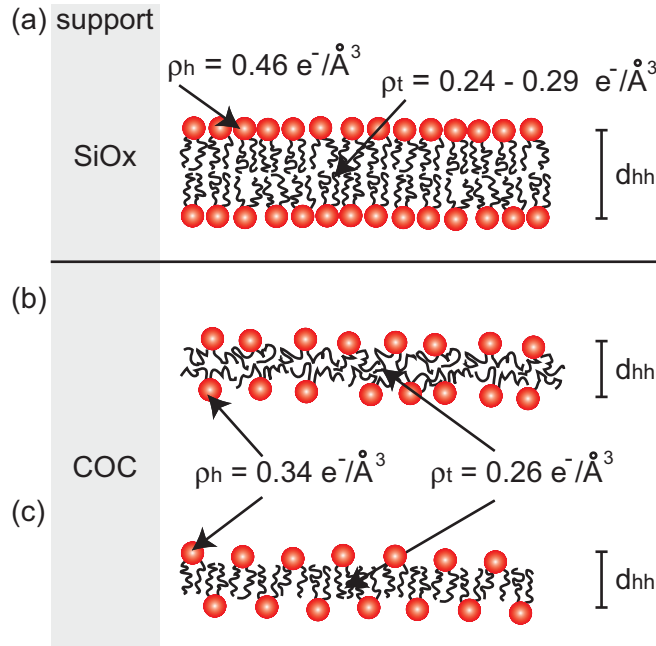


Figure 7.8: Packing density in a bilayer: (a) typical bilayer as found in supported DOPC membrane stacks or on SiOx. Thinned bilayer: (b) the tails are coiled (c) the tails are interdigitated.

For COC, a different, more general mechanism may be responsible for the formation of a thinned bilayer. Burgess et al. [31] showed that the bilayer thickness (d_b) of DMPC membranes spread on gold depended critically on the surface charge density of the gold surface. DMPC has the same head group as DOPC but two shorter fatty acid residues without any double bonds (14:0). At charge densities more negative than -0.2 C/m^2 , the bilayer thickness on gold corresponded to the thickness typically found for fully hydrated multilayers ($d_b = 37 \text{ \AA}$). A similar surface charge density (-0.25 C/m^2) was estimated for silicon oxide surfaces at pH 8 [21]. In turn, the bilayer thickness on SiOx is the of the same size as in bilayer stacks.

At zero surface charge the bilayer thickness d_b on gold was reduced to 26 \AA . The ζ -potential of COC is -25 mV [127] corresponding to a basically uncharged surface. Remarkably, the reduced bilayer thickness on COC agrees with the reduced bilayer thickness on uncharged gold surfaces, suggesting that surface charge may control membrane thickness.

On the other hand, we can not exclude other explanations that may be responsible for the membrane thinning on COC. Such reasons could comprise surface roughness or details of the molecular composition of the surface. This is supported by the enlarged d_{hh} found on H-Si. The d_{hh} of DOPC on H-Si was calculated to be 40 \AA , 3 to 5 \AA larger than the respective literature values, while ρ_h and ρ_t did not deviate drastically. While

both H-Si and COC are hydrophobic, those substrates are very different in terms of molecular composition. Also, the COC support has a larger surface roughness which might influence the packing density as well. For a membrane prepared by solvent exchange on COC, a bilayer model also fits the data reasonably well. The head-to-head distance is 27 Å in accordance with the distance gained from the vesicle fusion sample. The reduced electron density contrast ($\rho_h = 0.33 \text{ e}^-/\text{\AA}^3$ and $\rho_t = 0.29 \text{ e}^-/\text{\AA}^3$) compared to the vesicle fusion sample can be explained by intercalated 2-propanol molecules. Another explanation is the formation of defects smaller than the optical resolution. Other experiments performed in our lab in which DNA molecules were adsorbed onto mixed DOPC/DOTAP lipid membranes did not show a difference between the preparation methods although these experiments are intrinsically very sensitive to even small membrane defects [128]. Therefore, the reduced electron density of the heads is most likely explained by 2-propanol molecules being intercalated into the membrane rather than defect formation.

The fluorescence microscopy and FRAP experiments did not detect any difference in the lipid membranes prepared by vesicle fusion or by solvent exchange. This was further supported by x-ray reflectivity experiments where both preparation techniques resulted in similar curves except for a slight reduction in the electron density contrast.

7.3.4 Further Structural Lipid Membrane Models

Can only a thinned bilayer explain our data or is there another solution which would result in a similar reflectivity curve? For an overview of the different structural models of supported membranes, see section 4.3.

Clearly, a model without a lipid layer does not fit the measured reflectivity data at all and the homogeneous coverage observed with fluorescence microscopy can not be explained without any coverage. We can also exclude the formation of a monolayer with the hydrophobic tails inserted into the COC support [Fig. 4.4 (c)] or with their tails laying flat onto the surface [Fig. 4.4 (b)] because both possibilities would lead to a rather immobile layer. This leaves three possible configurations: a supported upright fluid monolayer [Fig. 4.4 (d)], a solid-supported bilayer [Fig. 4.4 (e)], and multilayers, e.g. a trilayer [Fig. 4.4 (f)].

The monolayer versus bilayer formation was discussed previously (s. 7.3.3) and we found that a monolayer can not explain our measured data satisfactorily while a thinned supported bilayer does. However, a third possibility, the formation of multilayers, has not yet been discussed. Immediately our reflectivity curve proves that the lipids do not assemble into a multilamellar structure with more than 10 layers on COC because no indication for a multilayer Bragg peak was discernable. The formation of a trilayer, i.e. a bilayer on a monolayer, is another possibility. Therefore, we fitted the reflectivity

data using a trilayer box model. The resulting best fit multiplied with q_z^4 is shown in Fig. 7.9 (a) and compared with the best fit for a bilayer box model and the measured data. Fig. 7.9 (b) displays the corresponding electron density profiles. The formation of a trilayer is very unlikely because the best fit assuming trilayer box model results in unphysical parameters, such as an extremely low head-to-head distance of the lipid supported bilayer ($d_{hh} = 21 \text{ \AA}$). There is no explanation why the lipid supported bilayer should be so strongly distorted since the influence of the surface should be screened by the underlying monolayer. Also, for a lipid supported bilayer, we would expect to get two diffusion constants, one slower one for the monolayer directly attached to the surface and a larger one for the bilayer stacked on top. Therefore we tried to fit our FRAP data with a model assuming two different diffusing species. The population of the slower species consisting of the lipids in the lower monolayer should make up about 30% of the whole population while the faster species consisting of the bilayer lipids make up about 70%. Fits assuming such a two component system always resulted in the two diffusion constants coinciding at the value determined for the diffusion constant of a single species. Therefore our FRAP data also does not support a membrane with two different diffusion constants. Additionally, a bilayer stacked onto a monolayer is unlikely stable against the large shear rates generated during the preparation process in our microfluidic chamber (s. 5.1). Of course, this excludes the existence of higher order layer systems as well, especially since such supported oriented lipid lamellar systems have been found to be unstable [30, 129, 130, 67].

7.3.5 Water Layer

Finally, we want to address the question whether a mesoscopic water layer ($d_w \geq 10 \text{ \AA}$) is needed to ensure a fluid bilayer.

In the literature d_w was determined directly with scattering methods [131, 28, 27, 26, 30] or indirectly with microscopic techniques [132] and ranged between 5 \AA and 500 \AA . The large deviations in d_w resulted most likely from different surface treatments prior to lipid deposition.

In our study, we tried to determine the size of the water gap (d_w) between the membrane and the support for COC, SiOx and H-Si. We were not able to resolve a water layer on COC within the error of the surface roughness which implies that d_w must be smaller than 7 \AA if present at all. Also, no water gap was resolved on SiOx and H-Si, implying that in these cases, d_w is smaller than 4 \AA and 3 \AA respectively. Recent x-ray reflectivity measurements on DOPC membranes on SiOx confirm this value [133, 70].

The fact that we obtain fluid membranes on COC and SiOx without a significant water layer present suggests that a mesoscopic water layer is not mandatory to maintain fluidity. Note that we do not exclude the possibility that hydrating water molecules surround the lipid headgroups.

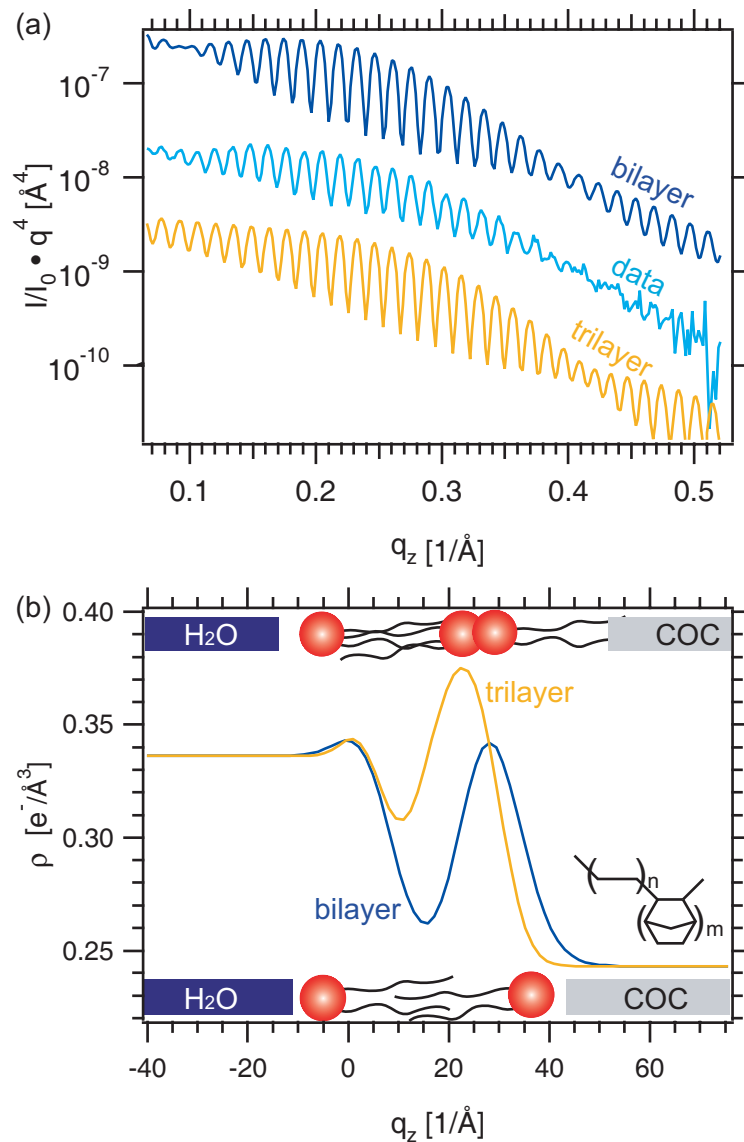


Figure 7.9: Analysis: (a) The top curve features the best fit to the reflectivity curve assuming a bilayer box model. The curve is divided by the Fresnel reflectivity q_z^{-4} (dark blue solid line, “bilayer”). Stacked under it, the measured reflectivity curve (light blue solid line, “data”) is displayed. The last curve represents the best fit to the reflectivity curve using a trilayer box model (orange solid line, “trilayer”). (b) The profiles corresponding to the fitted curves in (a) are shown (bilayer dark blue line, trilayer orange line). Schematic drawings illustrate the box models.

7.4 Conclusion and Outlook

Here, it is demonstrated that it is possible to prepare homogeneous and fluid lipid membranes on COC surfaces for different membranes consisting of different concentrations of DOTAP and DOPC. Using x-ray reflectivity measurements we found that these membranes consist of a thinned bilayer. These coating properties make the thermoplastic COC an ideal material for biofunctional surfaces [128].

In the future, the structure of supported membranes should be studied in dependence of the contact angle. Is there a critical contact angle at which the structure of the supported membrane changes from bilayer to monolayer? Maybe this transition depends on the exact chemical composition of the support. Pure highly packed hydrocarbon chains lead to supported monolayers. What needs to be changed to produce bilayers? The microfluidic setup can easily be modified to investigate the above questions.

8 DNA Localization and Stretching on Periodically Microstructured Lipid Membranes

8.1 Introduction

DNA is the storage molecule of our hereditary information: Our chromosomes encode not only all proteins found in our body but they also regulate their time-dependent expression. Therefore it is very important to obtain a thorough understanding of the chemical and the physical properties of DNA. Studies on a single molecule level provide new insights compared to bulk investigations since:

1. Heterogeneities and impurities are intrinsically impossible.
2. Transient states may be investigated whose signals might be too weak to be detected in bulk experiments.
3. Only low amounts of probe material are necessary.

Single molecules can be investigated for example by transmission or scanning electron microscopy, by AFM or by optical microscopy, especially fluorescence microscopy. While the first two techniques only allow to see static images, AFM and fluorescence microscopy enable us to observe dynamic processes. Additionally, fluorescence microscopy allows to gain fast and instantaneous information about a pretty large area (in this study with a 100× objective: $90 \times 70 \mu\text{m}$ within $< 0.5 \text{ s}$), allowing for high content screening.

Fluorescence microscopy is restricted to obtain sharp images only from the very thin focal plane of the objective (here: $\sim 0.2 \mu\text{m}$). Background fluorescence originating from other molecules or from parts of the studied molecule which are not in the focal plane severely degrades image quality. It is hence necessary to confine the molecules of interest to a 2-D plane to obtain sharp images while not destroying their native properties.

B. Maier et al. [102, 103] established a system where DNA molecules are confined to the plane of a glass-supported cationic fluid lipid membrane. Although attached to the

membrane by electrostatic interactions, the DNA keeps lateral mobility. B. Maier et al. proved that the center of mass movement can be described very well with the Rouse model while the radius of gyration scaled as expected for a self-avoiding 2-D polymer.

Furthermore, the charged supported membrane system has great potential not only for the investigation but also for the selective manipulation of single DNA molecules. For example, Olson et al. [104] proved that different sized DNA molecules separate once an electric field is applied. By incorporating proteins in the lipid membrane the DNA could be processed as needed for biotechnological applications. For example, membrane bound restriction enzymes could cut DNA, polymerases could reproduce it, transcription factor could anchor DNA to a certain location. Obviously, this system could serve as a molecular workbench for DNA molecules and potentially also for other charged biopolymers (s. Fig. 8.1).

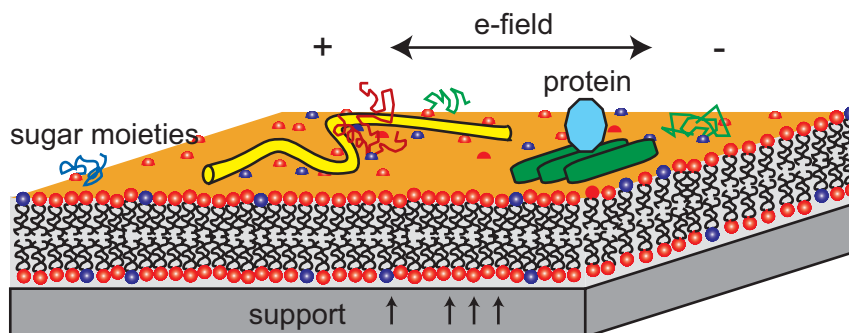


Figure 8.1: Schematic drawing of a supported lipid membrane used as a molecular workbench for the manipulation of single DNA molecules (yellow). Integrated into the lipid membrane are functional proteins (green cylinders and blue decagon) and lipids (blue). Oligosaccharides are depicted as red, green or blue zigzag lines. The support can be dynamically structured by local fields, such as heat or electrical fields (symbolized as arrows).

We explore the behavior of DNA adsorbed on cationic lipid membranes prepared on grooved, periodically structured surfaces. These microstructured membranes reveal a striking ability to stretch DNA which is prone to play a significant role for future biophysical and biotechnological applications.

In addition to potential technological applications, the system studied here is also of interest from a theoretical polymer physics point of view: What happens with the large-scale conformation of semi-flexible polymers, such as DNA, once they are adsorbed on curved surfaces, such as periodically structured surfaces? In a previous work, the reaction of DNA to external constraints was examined in the case of DNA confined to channels whose dimensions were smaller than the radius of gyration of the free molecule. Under such conditions DNA was found to stretch along the channel [60].

To answer these questions, periodic arrangements of long grooves with a rectangular cross section were imprinted into COC foils. Lipid DOPC membranes with varying amounts of the cationic lipid DOTAP were prepared on those topologically structured foils in a microfluidic chamber (s. section 5.1). The post-deposition dynamics and conformations of adsorbed λ -phage DNA molecules were visualized using fluorescence microscopy.

8.2 Theory

The theory explaining the experimental processes observed in this study was developed by Leo Golubovic [134, 128]. On planar cationic lipid membranes, a DNA molecule has a random walk shape fluctuating in time. The essential difference between the planar and the structured membranes is that the surfaces of curved membranes are generally *not* equipotentials. Due to this, a macro-ion adsorbed on a curved charged surface attains a position dependent free energy, which depends on the local curvature C of the surface. In the following, the DNA molecules shall be represented as a uniformly charged cylinder with radius r_{DNA} sliding along our one-dimensionally modulated membrane surface. In our case, the curvature free energy in Eq. 8.1 is the difference between binding free energy per unit length of DNA adsorbed along a charged large cylinder with radius $R = -1/C > r_{DNA}$ and the binding free energy of DNA adsorbed on a charged plane. DNA with its axis along the direction of the grooves acquires the potential energy of the form

$$U_{ul}(C) = -\Gamma C, \quad (8.1)$$

per unit length of the cylinder [128]. In Eq. 8.1, Γ is the attraction coefficient. Using the Poisson-Boltzmann theory, we estimate the constant Γ to range up to about $5 k_B T$ in the present system depending on salinity and charged lipid fraction [134]. We worked at a temperature of $T = 30^\circ\text{C}$, corresponding to a thermal energy $k_B T \approx 25 \text{ meV}$ where k_B is the Boltzmann constant. In essence, Eq. 8.1, with Γ positive, exhibits a Gibbs-Mullins-type change of the binding free energy of an adsorbed object due to a non-zero surface curvature: surface sections with $C > 0$ (concave parts, curved upwards) bind the object more strongly than planar surface sections ($C = 0$) while convex parts ($C < 0$) bind less strongly [135]. For the present one-dimensionally modulated surface, the curvature dependent potential in Eq. 8.1 yields an interesting potential landscape, consisting of a periodic sequence of potential traps ($C > 0$) and barriers ($C < 0$), see Fig. 8.2. Note that there are actually two traps inside each groove. They occur at highly curved sections of the surface, the surface edges, across which the interface slope angle increases quasi-discontinuously by an amount of $\Delta\Theta$ over a very narrow edge width ω , see Fig. 8.2 (c). By Eq. 8.1 such an edge yields a potential trap (potential well) with the depth $-U_0 = -\Gamma \Delta\Theta/\omega$. A single long edge-trap can efficiently bind (localize) a

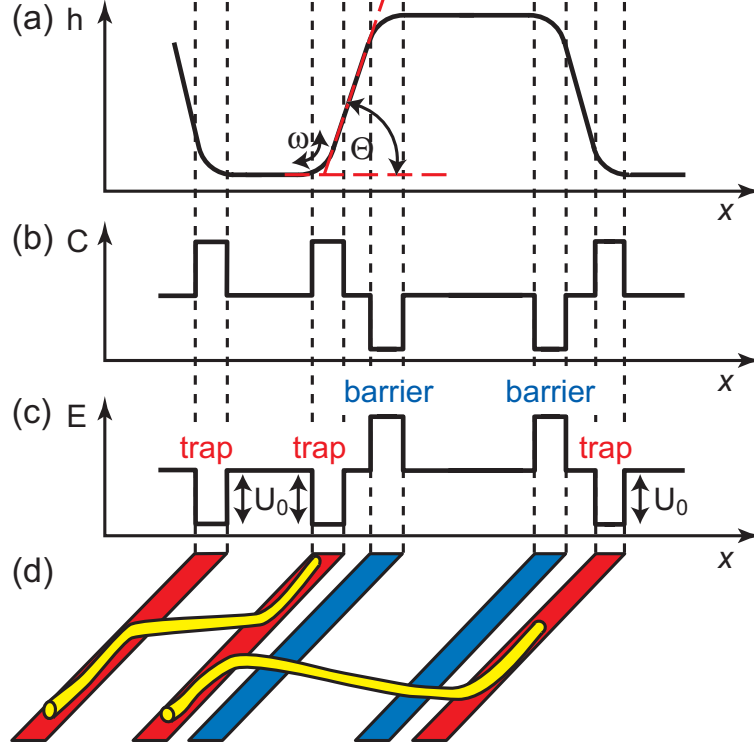


Figure 8.2: From surface topography to the potential energy of DNA: (a) Schematic drawing representing a cross sectional profile of the surface height. (b) Curvature C corresponding to the surface topology. (c) Resulting potential energy E of a DNA molecule on the surface. Note that there are two potential traps inside every groove. They are situated at highly curved sections of the surface, the surface edges at which the surface slope angle quickly increases by the amount $\Delta\Theta$ over the narrow edge width ω (see Fig. 8.5). (d) Schematic drawing of a DNA molecule making a short jump between the two potential traps inside the same groove (molecule on the left) and of a DNA molecule making a long jump between two potential traps located in two different grooves.

semi-flexible polymer along it, provided this binding is strong enough to overcome the molecules positional entropy tending to unbind it from the trap. To elucidate this, we consider the difference between the free energies per unit length of the bound and the free polymer,

$$\Delta F_{ul} \approx -U_0 + F_{st}. \quad (8.2)$$

Here F_{st} is the steric entropy free energy per unit length of a long polymer confined in two dimensions within a stripe (2D “tube”) of the width ω [136]:

$$F_{st} = 1.103 \frac{k_B T}{(\zeta_p/2)^{1/3} \omega^{2/3}}. \quad (8.3)$$

Here, ζ_p is the persistence length of the polymer. Thus

$$\Delta F_{ul} \approx -U_0 (1 - k), \quad (8.4)$$

using the binding parameter

$$k = F_{st}/U_0 = 1.103 \frac{k_B T}{\Gamma \Delta \Theta} \left(\frac{2\omega}{\zeta_p} \right)^{1/3}. \quad (8.5)$$

$k_c \approx 1$ is the critical binding parameter: For $k < k_c$, i.e. $\Delta F_{ul} < 0$, the binding energy wins over the entropy ($U_0 > F_{st}$) and the polymer remains localized inside the edge. Conversely, for $k > k_c \approx 1$, i.e. $\Delta F_{ul} > 0$, the entropy wins over the binding energy ($F_{st} > U_0$) and the polymer unbinds from the edge while still bound to the membrane to eventually assume the shape of a 2-D self-avoiding random walk [128].

So far, we have focussed on the effects of a single edge potential trap whereas on our surfaces we had a periodic sequence of such edge-traps competing to capture DNA (Fig. 8.2). Due to this, a very long polymer may still maintain a random walk shape even for $k < k_c$ by developing crossings between different attractive edges (Fig. 8.2 (d)). Note that the presence of such a crossing along the polymer with width L_c introduces an extra free energy cost relative to a polymer completely bound to a single edge of the form

$$\Delta F_c = \sigma L_c. \quad (8.6)$$

The line extraction tension $\sigma = -\Delta F_{ul}$ is the free energy cost to unbind a unit length of the polymer from the edge-trap. It is positive for $k < k_c$. At long times, in thermodynamic equilibrium, crossings between traps must form in a long enough polymer: by analogy to thermally activated domain walls in 1-D magnetic systems [137], the average separation in thermal equilibrium between the crossings along the polymer contour behaves as

$$\zeta_c \sim \exp(\Delta F_c/k_B T) = \exp(L_c/l_\sigma), \quad (8.7)$$

with l_σ the capillary length given by

$$l_\sigma = k_B T / \sigma \approx \omega \frac{k_B T}{\Gamma \Delta \Theta (1 - k)}. \quad (8.8)$$

If ζ_c is much larger than the polymer size there will be no such crossings once the thermodynamic equilibrium is reached. Note that on our surface, DNA molecules can form “short crossings” between the two edge-traps in the same groove (see Figs. 8.5 and 8.2) or “long crossings” between edge-traps in different grooves. The long crossings will of course cost more energy than the short ones and therefore the equilibrium distance between two short crossings ζ_c^s will be smaller than the distance between two long crossings ζ_c^l [128].

8.3 Experimental Observations

At first, it was necessary to measure the curvature and the inclination angle to estimate the binding parameter k and the separation distance between crossings ζ_c^s and ζ_c^l for our experimental conditions. Additionally, the fluidity of the structured lipid membrane had to be confirmed.

8.3.1 Characterization of the Master and the Lipid Membrane

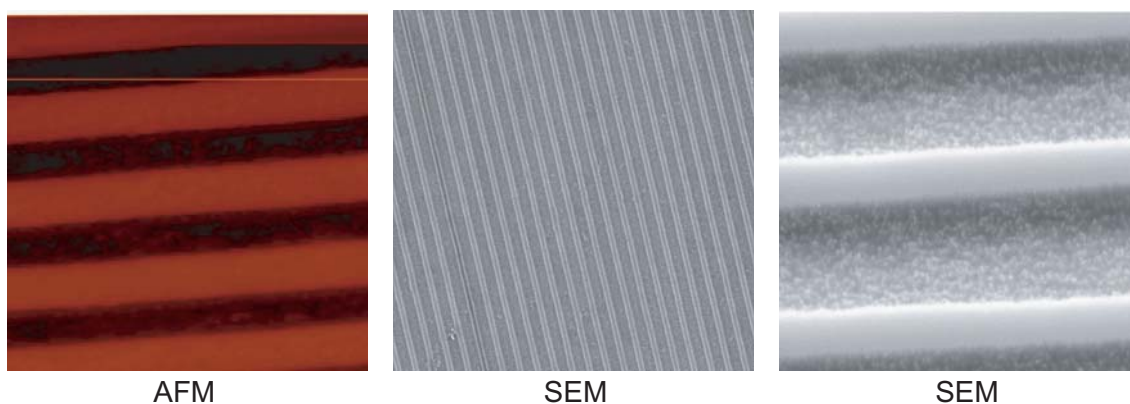


Figure 8.3: Different images of the microstructured silicon master.

Fig. 8.3 shows pictures of the silicon master used to imprint the COC foil. They were obtained with AFM (left) and SEM (middle, right).

The imprinted foil is presented in Fig. 8.4. The left and the middle image feature an AFM and a SEM image of a section of the imprinted foil respectively. A single channel is imaged with AFM (right). The AFM images were used to extract a height profile of the surface perpendicular to the channel direction (see Fig. 8.5). From the height profile of a single channel [Fig. 8.5 (b)] the local slope angle $\theta = \arctan(dh/dx)$ and the curvature $C = d\theta/ds = d^2h/dx^2 / [1 + (dh/dx)^2]^{3/2}$ were derived. θ and C are displayed versus the distance perpendicular to the channels x for the right side of the channel as indicated by the dashed circle in Fig. 8.5 (b). At the edge, the curvature C and θ reached a peak level of $C = 0.05 \text{ nm}^{-1}$ and $\theta = 73^\circ$. Of course, the finite AFM tip size will influence these results by decreasing the measured curvature. The tips used are supposed to have a radius of curvature of maximal 10 nm. Therefore the AFM images obtained were diluted with a tip radius of 10 to eliminate this influence. The curvature and the inclination angle are found to be $C = 0.14 \text{ nm}^{-1}$ and $\theta = 74^\circ$ [Fig. 8.5 (c)]. As expected, the curvature increased while θ remained unchanged. For future calculations, the values resulting from the diluted image are used because these values are more realistic.

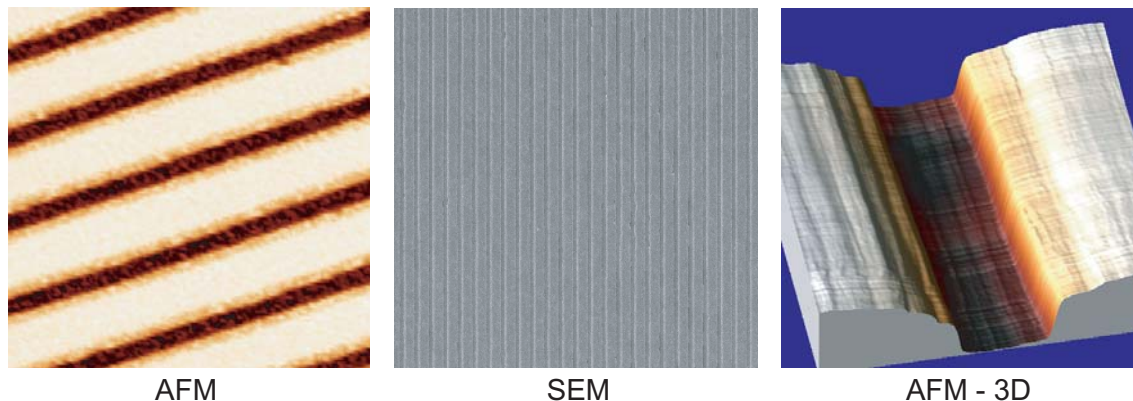


Figure 8.4: Different views of the imprinted COC foil.

The average surface curvature within the edge is $C = \Delta\theta/\omega \approx 0.05 \text{ nm}^{-1}$, whereas $\Delta\theta \approx 1 \text{ rad}$, corresponding to an edge width $\omega \approx 20 \text{ nm}$.

From Eq. 8.5 and $\zeta_p = 60 \text{ nm}$ for 1:5 labeled DNA [15] the binding parameter k was calculated to be $k \approx 0.96 k_B T/\Gamma \approx k_B T/\Gamma$ for our experimental conditions. For a membrane containing 95% DOPC (neutral lipid) and 5% DOTAP (cationic lipid) the binding parameter was found to be $k \approx 0.2$. k increased with decreasing the amount of DOTAP. The capillary length was estimated to be some 50 times smaller than the distance between two traps in neighboring grooves $L_c^l = 1000 \text{ nm}$. Because of this large separation between the length scales of L_c^l and l_σ the average equilibrium distance between such crossings along the polymer contour $\zeta_c \sim \exp(L_c/l_\sigma)$ was large, primarily due to having narrow edges here. For a realistic finite size polymer such as λ -phage DNA, this means that there will be no such crossings between grooves once the thermal equilibrium is reached. In practical terms, the extinction of the long crossings relied on the kinetic ability of the DNA to reach its thermal equilibrium shape within experimentally accessible time scales.

The membrane fluidity plays a very important role for the 2-D mobility of the DNA molecules. For planar membranes supported on COC the structure and fluidity of the lipid membrane was resolved in chapter 7. Does the diffusion constant change on the structured surface as compared to the plane COC foil? FRAP experiments showed no difference in the diffusion constant of planar membranes to structured ones ($D = 0.7 \mu\text{m}^2/\text{s}$, data not shown). Since the grooves within the foil introduce a preferred direction to the system, the following question arises: Does the diffusion constant of lipids in the membrane parallel to the grooves (D_{\parallel}) differ from the diffusion constant perpendicular to the grooves (D_{\perp})? Standard techniques such as FRAP do not distinguish between the different directions but give an average diffusion constant. Continuous Bleaching [s. Fig. 8.6] allows to measure D_{\parallel} and D_{\perp} if the intensity profile perpendicular and parallel to the grooves are analyzed. Within the accuracy D_{\parallel} and D_{\perp} were calculated

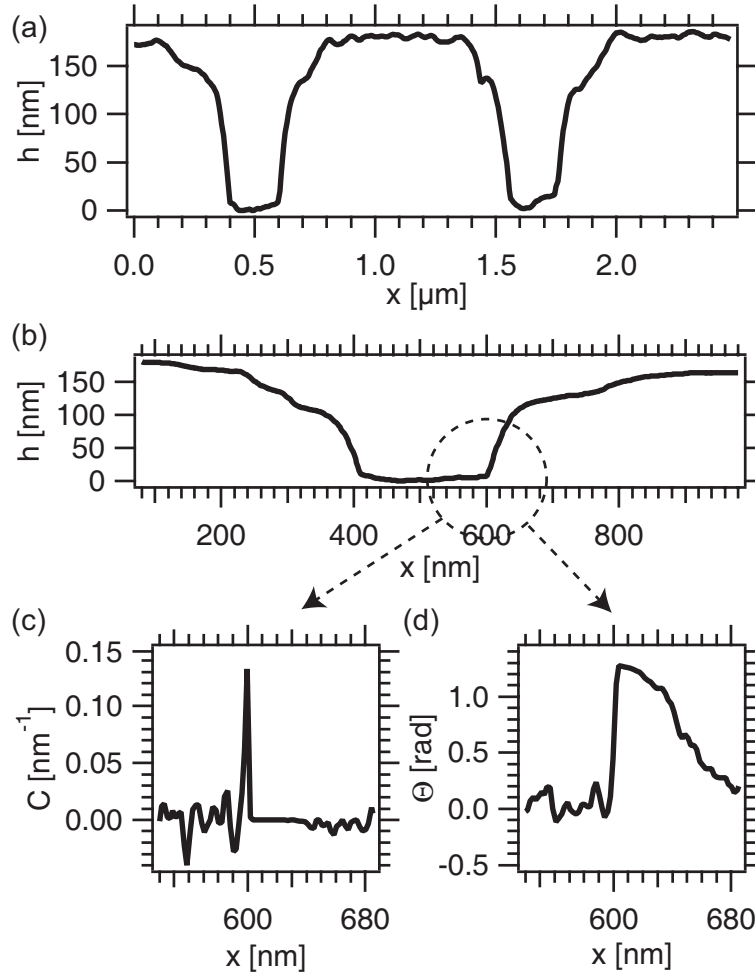


Figure 8.5: Cross sectional height profile of AFM images of small sections of the microstructured foil: (a) Height profile of two consecutive grooves taken perpendicular to the grooves. (b) To-scale height profile of a single channel. (c) Curvature C resulting from the circled part of the height profile in (b). (d) Inclination angle θ .

to be $1.8 \pm 1 \mu\text{m}^2/\text{s}$ and $2.1 \pm 1 \mu\text{m}^2/\text{s}$ respectively which coincided with the value of planar membranes $2 \pm 1 \mu\text{m}^2/\text{s}$. Therefore the lipid mobility was not influenced by the substrate structuring. Note that the fluorescence signal of the grooved membrane was modulated with a periodicity corresponding to the periodicity of the imprinted channels (1200 nm).

8.3.2 DNA Stretching

As a first step reference experiments on planar unstructured membranes supported on COC were conducted. DNA was adsorbed to membranes containing as little as 1%

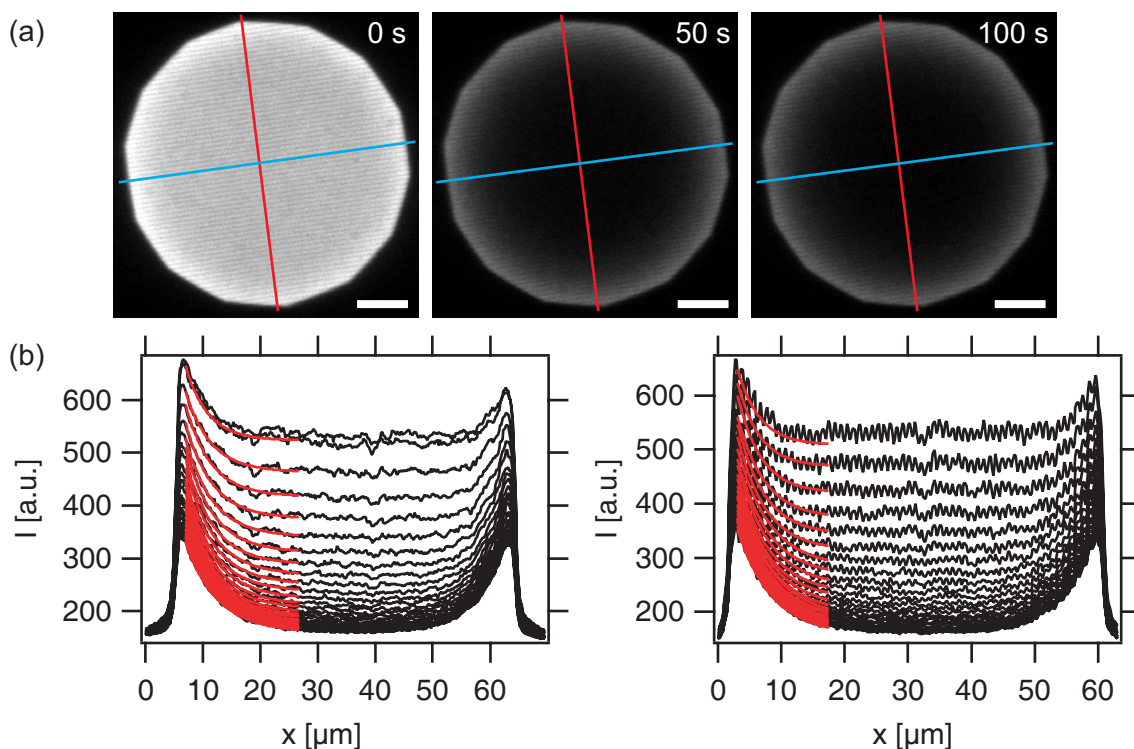


Figure 8.6: Diffusion constant of a COC supported lipid membrane parallel and perpendicular to the grooved surface: (a) Three images taken during continuous illumination. The left picture shows the membrane shortly after the illumination was turned on. The picture in the middle is taken after 50 s of continuous illumination and the right image shows the membrane after 100 s. (b) Intensity line profiles taken along the solid blue line (parallel to the grooves, left graph) and the red line (perpendicular to the grooves, right graph). The diffusion constants D_{\parallel} and D_{\perp} coincide at $2 \mu\text{m}^2/\text{s}$.

DOTAP. Up to 3% DOTAP DNA did attach during the attachment procedure but was washed away when the buffer was exchanged to the salt buffer. This happened even if great care was taken to avoid high flow rates resulting in large shear rates. We therefore conclude that the electrostatic attraction of the lipid membrane is sufficiently screened at 30 mM salt to unbind the DNA. At 5% DOTAP DNA stayed attached and relaxed into shapes expected from a self-avoiding polymer. The diffusion constant was estimated to be around $0.002 \mu\text{m}^2/\text{s}$ coinciding with the diffusion constant measured for λ -DNA on glass supported lipid membranes [102].

Initially, the freshly-adsorbed DNA molecules formed globules with a size of about $1 \mu\text{m}$ and were statistically distributed on the membrane surface. On grooved surfaces, we found a strong dependence of the subsequent DNA dynamics and shapes on the amount of the charged lipid.

We revealed a striking conformational behavior, the DNA stretching phenomenon, which

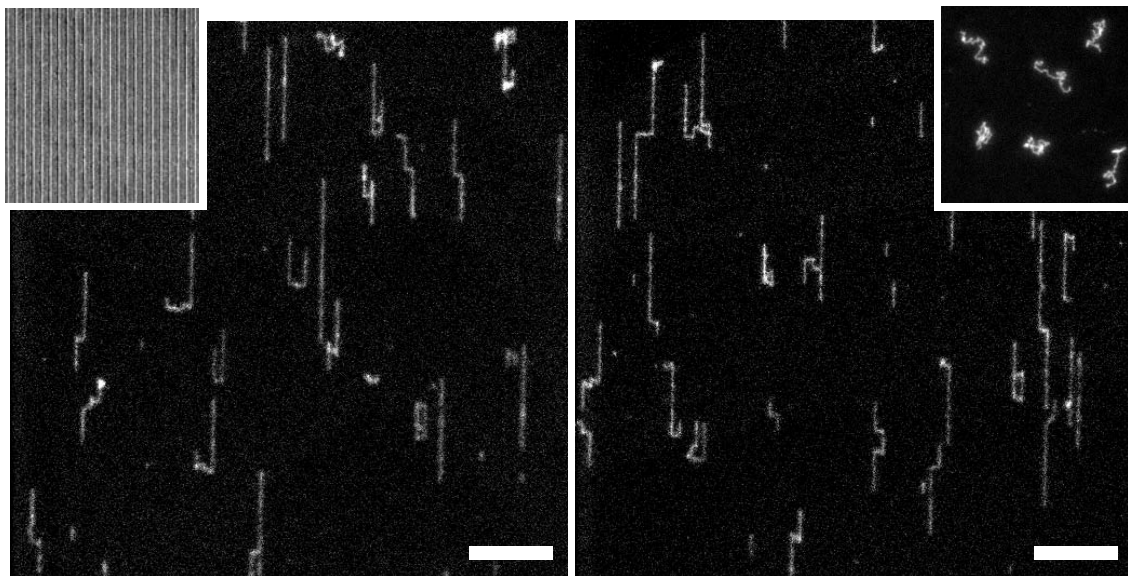


Figure 8.7: Florescence images of DNA aligned on membranes with 5% DOTAP. The inset in the left image shows a SEM image of the foil indicating that the grooves run vertically. The inset in the right image displays a typical fluorescence image of DNA on an unstructured membrane with 5% DOTAP. The bar represents $10\ \mu\text{m}$.

was best seen on membranes with 5% DOTAP at 30°C [Fig. 8.7]: Within the first 15 to 30 minutes, part of the DNA molecules packed into globules got efficiently pulled into nearby grooves. At the end of this process (stage 1), a typical DNA conformation included two long DNA sections (arms) pulled into neighboring surface grooves which were connected through $\sim 1\ \mu\text{m}$ long DNA strands running perpendicular to the channel direction. In Fig. 8.7 the grooves ran vertically as indicated by the left inset in the left image showing a SEM image of the grooved foil with the same scaling as the fluorescence pictures.

After stage 1 the DNA dynamics slowed down. It assumed the character of a 1-D reptation-like diffusion of the DNA molecule, which moves along its contour back and forth directed by the grooves. This diffusional motion eventually lead to a pull-out of one of the two DNA arms that are in the grooves, so the entire DNA molecule eventually slipped into a single groove. After this apparently irreversible extinction of the DNA crossings between grooves which occurred on a time scale of several hours, the entire DNA molecule was completely adsorbed into a single long groove of the periodically structured membrane. This 1-D diffusion limited stage of the DNA dynamics (stage 2) was captured in Fig. 8.7 in which we see some DNA molecules still exhibiting two arms connected by a DNA strand stretched between neighboring grooves as well as other DNA molecules that have already slipped into a single groove. The inset in the right image in Fig. 8.7 shows a control experiment performed under the same conditions except

that a planar membrane was used. The DNA molecules relaxed into a 2-D random coil conformation.

Complete stretching was never observed for our system because experimental restraints limited the observation time to about 6 h. Although buffers were sterile filtered and autoclaved, some DNase proteins still remained active leading to the destruction of the adsorbed DNA molecules after more than 8 h at 30°C.

Note that on the surfaces used during the experiments, DNA molecules can form short crossings between the two edge-traps in the same groove (see Figs. 8.5 and 8.2) with $L_c^s \approx 200$ nm about five times shorter than the length of the long DNA crossings between different grooves with $L_c^l \approx 1000$ nm. Therefore, non-equilibrium and equilibrium densities of the short crossings can be significant and responsible for the fact that the DNA length projected to the grooves direction is smaller than the total DNA contour length of $22 \mu\text{m}$ even for the DNA molecules completely adsorbed into single grooves (Fig. 8.7).

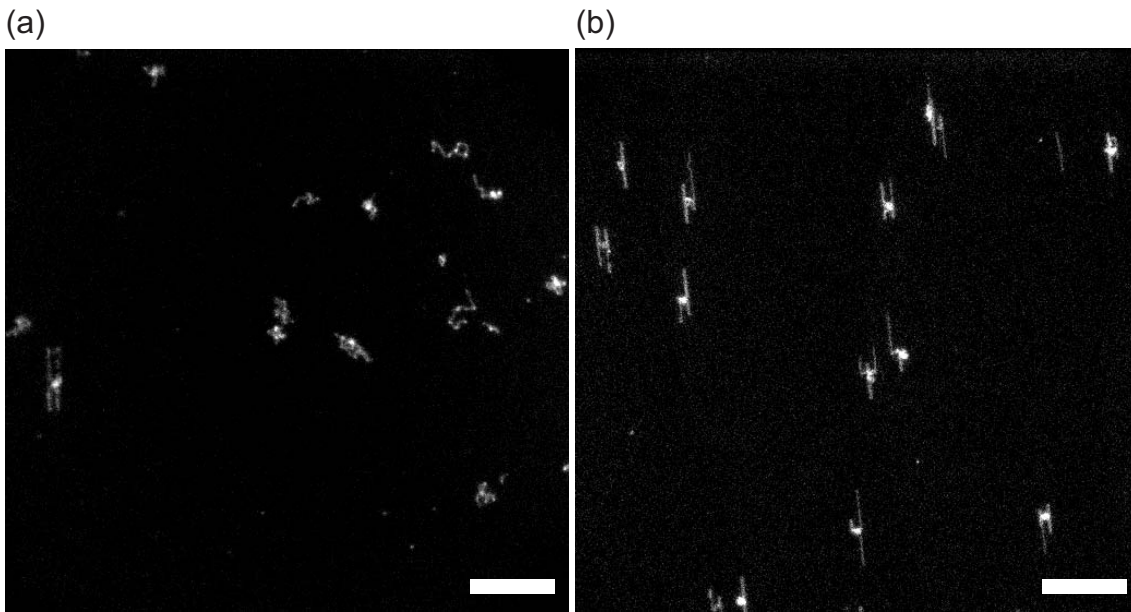


Figure 8.8: Florescence images of DNA aligned on grooved membranes with 3% (a) and 7% DOTAP (b). The bar represents $10 \mu\text{m}$.

The periodically structured charged membranes are thus capable to stretch long DNA molecules. What happened if the charge ratio was changed? Fig. 8.8 (a) presents an image of λ -DNA on a structured surface with 3% DOTAP. The DNA stayed attached while DNA on unstructured membranes with the same charge content detached. The DNA is mostly not oriented although there are some molecules which are at least partially stretched as seen on the left side of the image. It seems that 3% DOTAP is very close to the critical binding constant k_c . Very minor variations of the surface topology could

be responsible that in some parts DNA is pulled into the traps while in other sections it remained free on the membrane.

Intuitively, one would expect that the stretching effect increases with increasing trap attraction potential and therefore with increasing amount of DOTAP in the membrane. Interestingly, by experimenting with 7% DOTAP membranes, we found that the stage 2 was preempted by a halt of the stage 1 process [Fig. 8.8 (b)]: the initially formed small DNA globules released arms growing into grooves but then the arm growth was halted. If a membrane with 10% DOTAP was used, the DNA molecules never relaxed from their globular shape but remained visible as bright spots with a diameter of $\sim 5 \mu\text{m}$ for more than 4 h. This stop appears to be caused by energy barriers clogging the edges for the DNA advance. These barriers can be produced by surface curvature along the direction of the attractive lines (edge-traps), i.e. longitudinal imperfections of (otherwise straight) grooves, see Fig. 8.5 (b). Like the curvature potential of the edge-traps, a weaker curvature potential contributed by the less curved longitudinal imperfections also increases with increasing DOTAP percentage which eventually closes the edges for the DNA passage. Due to this effect, the stretching effect is only enhanced for increasing DOTAP percentage from about 3% up to 5%. 5% DOTAP turns out to be the optimum charged lipid fraction providing the minimum DNA stretching time of a few hours time scale. A further increase of the DOTAP percentage only slows down and eventually halts the DNA stretching.

For the 5% case, the binding parameter k was estimated to be $k \approx k_B T / \Gamma \approx 0.2$. It increases with decreasing amount of charged lipids allowing to cross the DNA unbinding transition at $k_c \approx 1$. Indeed, our experiments showed that DNA efficiently binds to the edges on membranes with 5% DOTAP (Fig. 8.8(b)), while on 3% DOTAP membranes we find that DNA doesn't enter the edges (see Fig. 8.8 (a)).

This effect is demonstrated on a more quantitative basis if the projection of the DNA shape to the direction parallel and perpendicular to the grooves (L_y and L_x) is plotted versus the elapsed time t [Fig. 8.9]. The length of L_y and L_x are determined by averaging over all DNA molecules seen in one image which do not touch the image border. The standard deviation is shown as the error bars. A linear fit is added to guide the eye. For 5% L_y reached $9 \pm 0.9 \mu\text{m}$ after 6 h while L_x remains at $4 \pm 0.5 \mu\text{m}$. For 3% L_x and L_y do not increase and therefore both stay at $4 \mu\text{m}$. For a membrane consisting of 7% DOTAP, L_y increased to $6 \pm 0.6 \mu\text{m}$.

For the following experiments a different master (master 2) was used for imprinting which produced grooves of 40 nm depth and a repetition period of 1000 nm. Interestingly, for this master, DNA molecules relax only very little from globular conformation at 5% after 3 h [Fig. 8.10 (a)] and even after prolonged relaxation time (4 h, [Fig. 8.10 (b)]). All DNA molecules show a distinct orientation along the direction of the grooves yet almost no stretching was achieved. A similar behavior was encountered when using the first master at 7%.

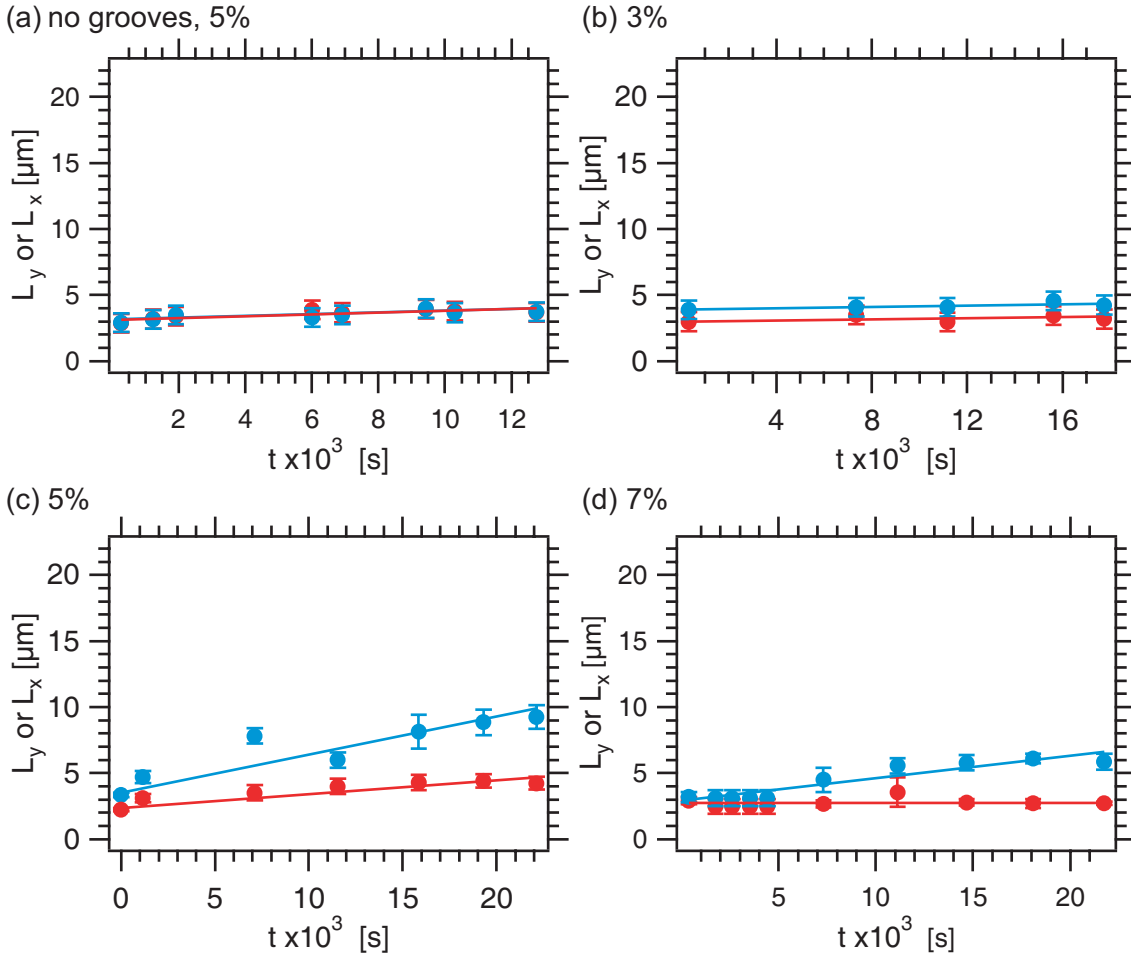


Figure 8.9: Projection of the DNA extension parallel (L_y , blue) and perpendicular (L_x , red) to the channels for a DOTAP ratio of (a) 5% and no grooved and for structured membranes with a content of (b) 3%, (c) 5% and (d) 7% DOTAP. Linear fits are added to guide the eye.

Therefore, we reduced the fraction of the cationic lipid to improve the DNA stretching. For surfaces prepared with master 2 the best stretching effect was achieved at 3% DOTAP while it was 5% when using the first master. With master 2 it was possible to create such strong edge-traps that even though the 3-D unbinding transition at which DNA unbinds from planar membranes was crossed, the DNA was still strongly attracted to the edges which eventually lead to stretching. At 3%, the DNA stretching process occurred in the same three steps as with master 1 at 5%: adsorption as globules, arms being pulled into edge traps (stage 1, Fig. 8.11 (a)), and diffusional motion eventually leading to complete stretching (stage 2, Fig. 8.11 (b)).

The conformations of the DNA molecules can be classified into different categories according to the number of long crossings observed [Fig. 8.12]. Very few molecules were

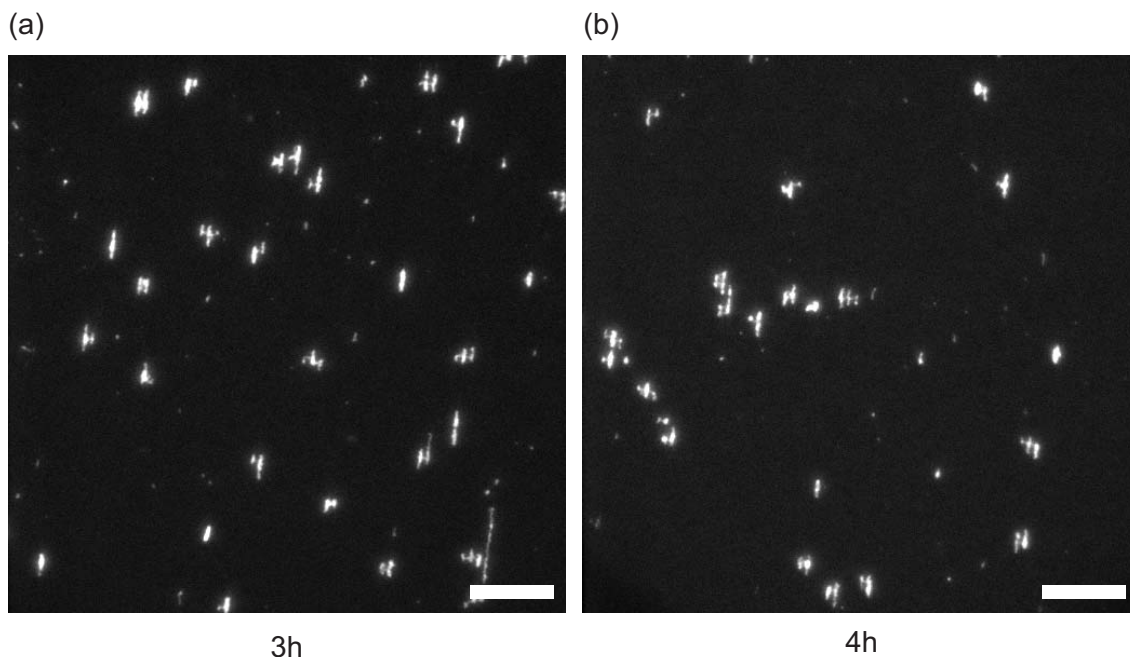


Figure 8.10: Fluorescence images of aligned DNA on a 5% DOTAP membrane supported on a microstructured COC foil. The foil was imprinted with master 2. (a) 3 h after addition of salt (b) 4 h after addition of salt. DNA is not efficiently stretched. The scale bar is $10\ \mu\text{m}$ long.

completely inserted into a single groove [Fig. 8.12 (a)], most molecules feature one or two long crossings [Fig. 8.12 (b) - (c)]. Again very few molecules exhibited three or more long crossings [Fig. 8.12 (d)]. Fig. 8.13 presents a close up view of one molecule with 6 crossings. The attractive and the repulsive lines corresponding to the surface height profile are indicated by red and blue lines respectively. One can see very nicely that most of the DNA was oriented in parallel to the attractive lines. The crossings are $1\ \mu\text{m}$ long and run always perpendicular to the direction of the grooves to minimize the length of the DNA outside the edge traps.

Both masters were prepared the same way except that the time for reactive ion etching was reduced for master 2. Therefore we expected that the curvature and the width of the edge traps remained the same leading to the same results for both masters. Obviously, the DNA stretching phenomenon is very sensitive to even slight changes of the surface topology causing the optimal DOTAP ratio to differ for both masters.

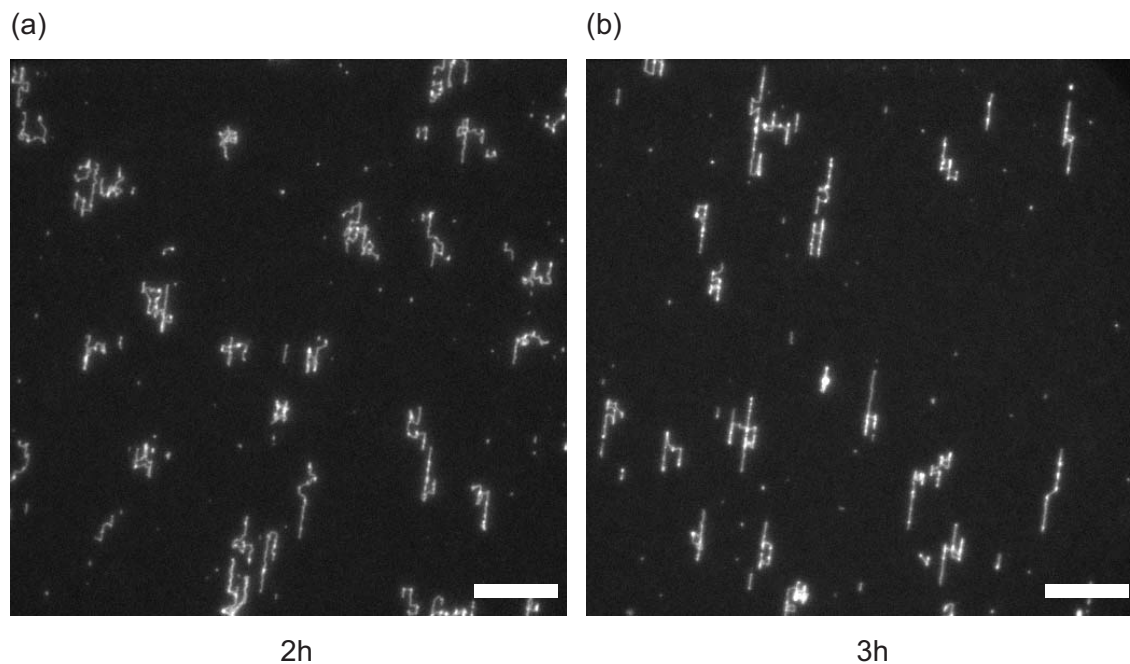


Figure 8.11: DNA on a 3% DOTAP membrane supported on a COC foil microstructured with master 2. (a) 2 h after addition of salt (b) 3 h after addition of salt. The scale bar represents 10 μm

8.4 Conclusion and Outlook

During this study, we showed repeatedly that DNA aligns and stretches on grooved membranes. DNA was stretched to 50% of its contour length on a surface with rectangular grooves and a repetition period of 1200 nm. The effect is strongly dependent on the amount of charge in the supported lipid layer. The optimal percentage of DOTAP for DNA stretching must be determined experimentally for each master separately.

To improve the reproducibility of the results the master should be covered with a protective coating to reduce wearing effects due to the imprinting process. After 20 or more imprinting processes, the microstructured supported membranes tended to have defects and the efficiency of the DNA stretching was reduced.

It would be interesting to calculate how the surface has to be shaped to create optimal DNA stretching. Naturally, the larger the distance between attractive lines, the less likely a single DNA molecule will make jumps and the more likely it is trapped along a single line. However, the probability of a DNA molecule being trapped at all is reduced. Therefore the distance between attractive lines may not be much larger than the 2-D radius of gyration of the DNA. The curvature creating a trap should be large but certainly not too large to immobilize the DNA hindering the reptational movement leading to a complete stretching of the DNA.

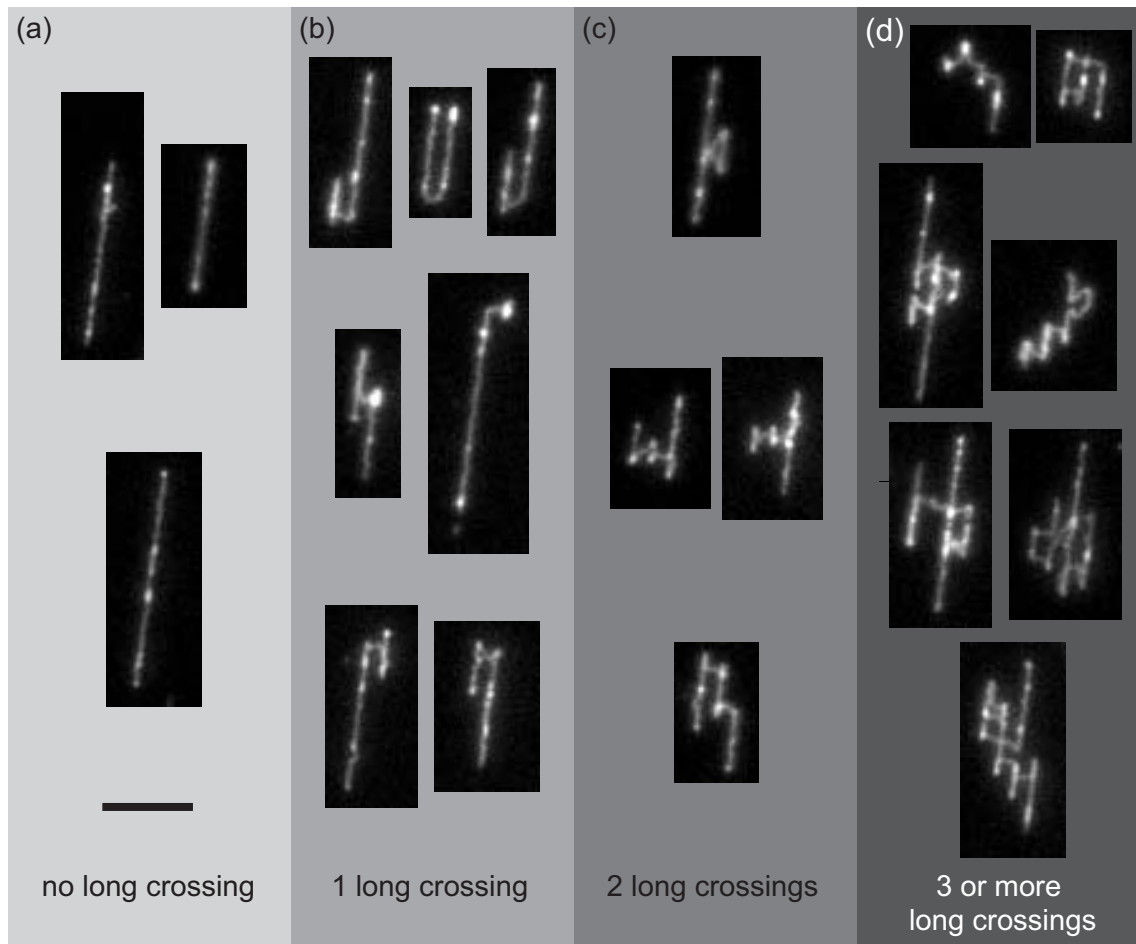


Figure 8.12: Typical conformations of λ -DNA molecules as seen with fluorescence microscopy on a membrane containing 5% DOTAP. The surface was microstructured with master 2. The length of the scale bar is $5\ \mu\text{m}$. The scaling is the same for all images shown here.

Of course, one would expect that triangularly shaped grooves are more efficient for DNA stretching because the competition of attractive lines within one groove is eliminated. For future experiments, it is therefore highly desirable to create a substrate with triangularly shaped grooves and a slightly enlarged repetition period (s. Fig. 8.14). Silicon (100) wafers etch naturally to such grooves if parts of its surface are exposed to potassium hydroxide. Silicon structured in such a way should be a good support for lipid membranes once it is oxidized. We expect DNA to stretch to higher percentages of its contour length, maybe even up to 100%.

Once stage 1 of the DNA stretching process is finished and the DNA has been pulled into a couple of grooves, electric fields could be applied in parallel to the grooves to reduce the time necessary for the completion of stage 2. This should improve the stretching

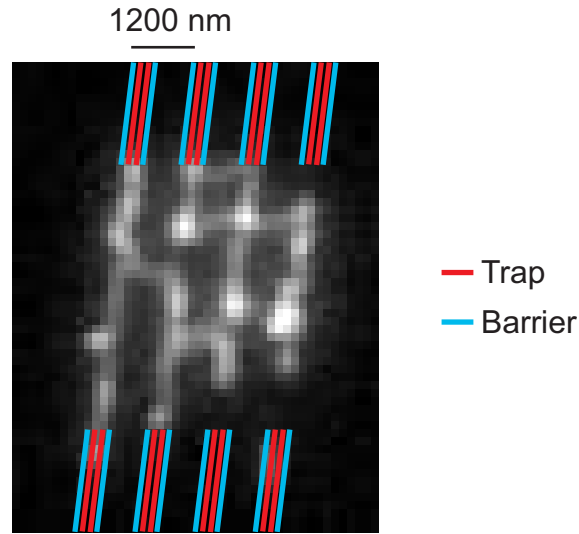


Figure 8.13: DNA on a 3% DOTAP membrane. The red and the blue lines indicate the position of the attractive and repulsive lines respectively.



Figure 8.14: Cross sectional profile of triangularly shaped grooves which are expected to align DNA more efficiently.

effect achievable within the experimental time frame.

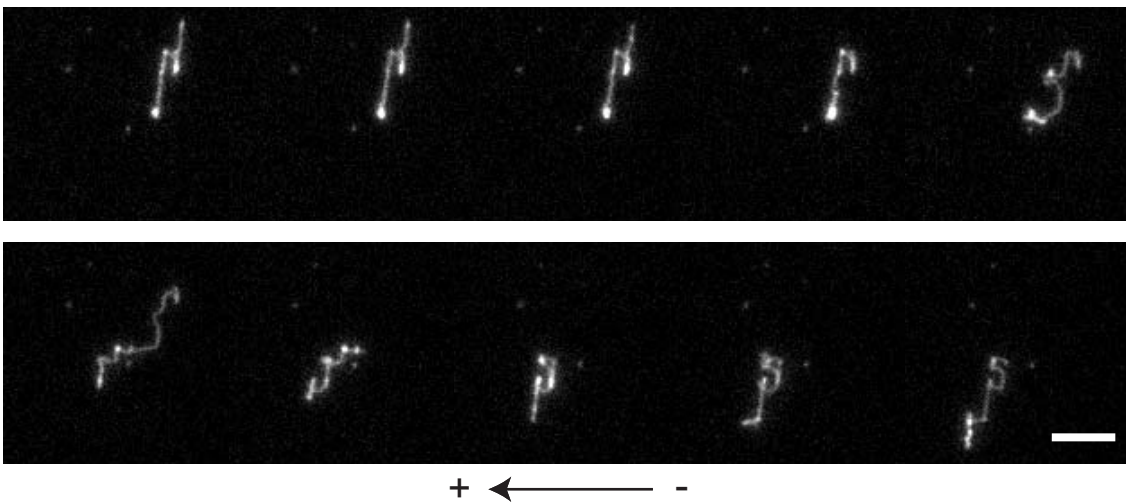


Figure 8.15: Fluorescence images of DNA oriented on a grooved membrane acting on an applied horizontal electric field of 6 V/cm. The time lapse between images is 30 s. The bar size is 5 μm .

Electric fields applied perpendicular to the groove direction should in principle allow to separate DNA molecules of different sizes (s. Fig. 8.15). Such an electrophoresis setup would work for very low amounts of DNA, even up to single DNA molecules.

9 The Future of Supported Lipid Membranes as a Tool for DNA Manipulation

As shown in chapter 8, fluid supported lipid membranes have great potential for biotechnological applications because they facilitate the manipulation of single biomacromolecules such as DNA. In the future this concept of a molecular workbench can be expanded further with the following projects:

9.1 Localization of DNA with Light Induced Surface Charges

A p-n junction is produced very close to the surface of an amorphous silicon substrate. Using such substrates as a support for fluid cationic membranes opens the opportunity to manipulate adsorbed DNA molecules contactlessly. When light above a certain wavelength is focussed onto a certain part of the substrate, charges will be induced and trapped there leading to local electrostatic potentials felt by the adsorbed DNA. This effect could be used to attract DNA to or repel it from certain surface areas (s. Fig. 9.1). Calculations of the expected local electric fields considering the special qualities of membranes (mobility, demixing, flip-flop) would be an interesting challenge.

9.2 Heat Fields

Using a membrane with a transition temperature accessible under experimental conditions such as DMPC/DMTAP mixtures ($T_m \sim 23^\circ\text{C}$) or DPPC/DPTAP ($T_m \sim 41^\circ\text{C}$) the membrane can be switched from an immobile to a mobile state. Local heating of the sample will lead to local phase transitions within the supported bilayer. DNA adsorbed to the membrane is immobile unless located near a heated area. If the heated area is slowly moved across the surface, we expect to see an effect similar to the zone melting process used in the silicon industry. Dirt and imperfections within the silicon move with

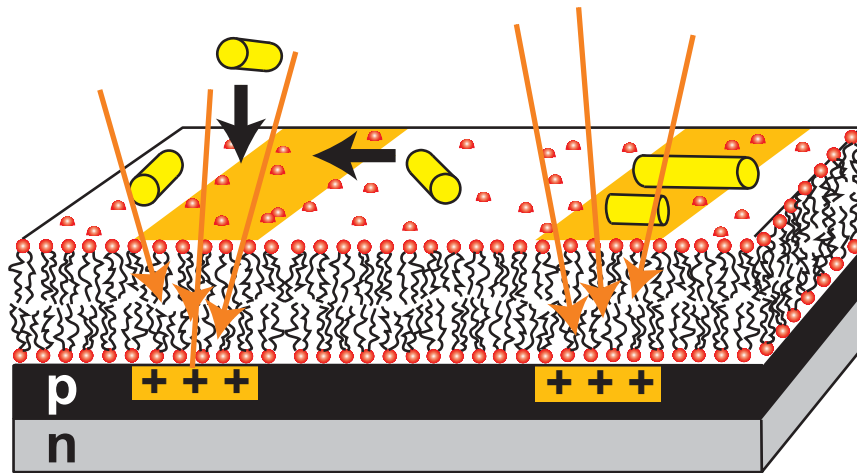


Figure 9.1: DNA (yellow) adsorbed to a fluid cationic membrane is manipulated with local surface charge. The surface charge is induced at a p-n junction in amorphous silicon close to the surface if irradiated with light above a certain wavelength (orange arrows).

the fluid heated zone and are therefore removed from the silicon body. Similar to this effect, we expect DNA to move with the heated, fluid lipid zone. This could be used to accumulate DNA on certain parts of the molecular workbench (s. Fig. 9.2). Similarly,

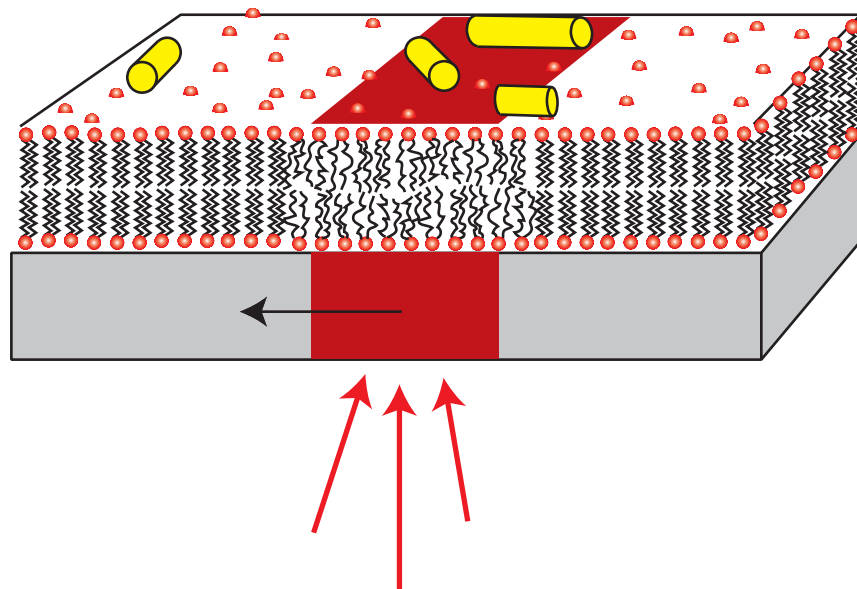


Figure 9.2: An infrared laser locally heats the substrate inducing the main phase transition of the supported cationic membrane. DNA (yellow) tends to follow the fluid part of the membrane.

membrane proteins could be structured laterally in supported membranes. The thermotropic segregation induced by local heat fields could be utilized to inscribe chemical gradients into the membrane. An infrared laser could produce the necessary local heat fields with the aid of optical grids and masks. The achieved structuring of the membrane components could be demonstrated by selective fluorescence labeling. Such structured membranes are ideal to investigate the adhesion behavior of cells. The cells will adapt to the created patterns and will orient themselves according to the peptide gradients.

List of Abbreviations

2-D	two dimensions
3-D	three dimensions
AFM	atomic force microscopy
bp	base pair
COC	cyclic olefin copolymer
DNA	deoxyribose nucleic acid
DMPC	dimyristoyl-phosphocholin
DOPC	dioleoyl-phosphocholine
DOTAP	dioleoyl-trimethylammonium-propane
dsDNA	double stranded DNA
FRAP	fluorescence recovery after photobleaching
H-Si	hydrogen-terminated silicon
k	binding parameter $k = F_{st}/U_0$
L_0	contour length
OG	octyl glycoside
POPC	palmitoyl-oleoyl-phosphocholine
SEM	scanning electron microscopy
SiO _x	silicon oxide
ssDNA	single stranded DNA
TOTO-1	1-1'-[1,3-propanediyl]bis[(dimethyliminio)-3,1-propanediyl] bis[4-[(3-methyl-2(3H)-benzothiazolylidene)methyl]]-tetraiodide
YO-PRO-1	4-[(3-methyl-2(3H)-benzoxazolylidene)methyl]-1-[3- (trimethylammonio)propyl]-,diiodide
ζ_p	persistence length

List of Figures

2.1	3-D View of dsDNA	5
3.1	Force Extension Curve of dsDNA	12
4.1	Schematical Drawing of a Plasma Membrane	17
4.2	Buildup of POPE	19
4.3	Illustration of Different Lipid Bilayer Phases	19
4.4	Coating Possibilities of Lipids on COC	20
5.1	Structure Formula of DOPC and DOTAP	23
5.2	Schematic Drawing of the Microfluidic Chambers Used in this Study	25
5.3	Schematic Illustration of the Imprinting Process	26
5.4	Jablonski Diagram	28
5.5	X-Ray Reflectivity Explained Schematically	32
5.6	Photo and Schematic Drawing of the Microfluidic Chamber Used for X-Ray Studies	34
5.7	Schematic Drawing of the Principles of AFM	34
5.8	Schematic Illustration of the Principles of SEM	35
6.1	Electron Microscopy Image of different Phages	37
6.2	Electron Microscopy Image of a T5 Phage Virion	38
6.3	Schematic Drawing of the Experimental Setup	39
6.4	Fluorescence Images of a Single Phage Particle with partly ejected DNA	41
6.5	Length of Ejected DNA vs. Applied Flow	42
6.6	Estimation of the Applied Force at certain Flow Velocities	43
6.7	Fluorescence Images of the DNA Ejection Process	44
6.8	Length of Ejected DNA vs. Time	45
6.9	Histogram of the Ejected DNA Lengths	46
6.10	Development of the Size Distribution of DNA with Time	47
6.11	Time Resolved Distribution of DNA	47
6.12	Nick Induced Buckling of DNA	49
7.1	Continuous Bleaching of a Membrane on COC	55

7.2	FRAP Curves of Membranes on COC	57
7.3	Diffusion Coefficient vs. Content of DOTAP	58
7.4	X-Ray Reflectivity Curves of COC on Air, under Water and with a DOPC Membrane	59
7.5	Reflectivity Curves of DOPC Membranes on SiO _x and H-Si	60
7.6	Reflectivity Curves of a DOPC Membrane Prepared by VF and SE	61
7.7	Comparison of the Monolayer and the Bilayer Model	63
7.8	Illustration of Possible Bilayer Structures	65
7.9	Comparison of the Trilayer and the Bilayer Model	68
8.1	Schematic Drawing Showing a Molecular Workbench for Single DNA Molecules	72
8.2	Schematic Drawing How Surface Topography translates to Potential Energy	74
8.3	Different Images of the Microstructured Silicon Master	76
8.4	Different Views of the Imprinted Foil	77
8.5	Topological Information about the Imprinted Foil	78
8.6	Continuous Bleaching on Structured Membranes	79
8.7	Fluorescence Images of DNA Aligned on Membranes with 5% DOTAP	80
8.8	Fluorescence Images of Aligned DNA for 3% and 7% DOTAP	81
8.9	Projection of DNA Extension Parallel and Perpendicular to the Grooves	83
8.10	Fluorescence Images of Aligned DNA on a 5% DOTAP Membrane Microstructured with Master 2	84
8.11	Fluorescence Images of Aligned DNA on a 3% DOTAP Membrane Microstructured with Master 2	85
8.12	Typical Conformations of λ -DNA on a Membrane Microstructured with Master 2	86
8.13	Fluorescence Image of a Single DNA Molecule and Marked Attractive and Repulsive Lines	87
8.14	Cross Sectional Profile of Triangularly Shaped Grooves	87
8.15	Fluorescence Images of DNA Oriented on a Grooved Membrane Acting on an Applied Electric Field	87
9.1	Manipulation of Adsorbed 2-D DNA with Light Induced Charges	90
9.2	Manipulation of Adsorbed 2-D DNA with Heat Fields	90

List of Tables

- 6.1 Position of nicks and peaks along the T5 wt and T5 st(0) DNA. 48
- 7.1 Parameters extracted from x-ray reflectivity measurements for DOPC membranes on different supports. 64

Bibliography

- [1] BENSON, S. D. ; BAMFORD, J. K. H. ; BAMFORD, D. H. ; BURNETT, R. M.: Does common architecture reveal a viral lineage spanning all three domains of life? In: *Molecular Cell* 16 (2004), Nr. 5, S. 673–685
- [2] CERRITELLI, M. E. ; CHENG, N. Q. ; ROSENBERG, A. H. ; MCPHERSON, C. E. ; BOOY, F. P. ; STEVEN, A. C.: Encapsidated conformation of bacteriophage T7 DNA. In: *Cell* 91 (1997), Nr. 2, S. 271–280
- [3] KINDT, J. ; TZLIL, S. ; BEN-SHAUL, A. ; GELBART, W. M.: DNA packaging and ejection forces in bacteriophage. In: *Proceedings of the National Academy of Sciences of the United States of America* 98 (2001), Nr. 24, S. 13671–13674
- [4] ARSUAGA, J. ; TAN, R. K. Z. ; VAZQUEZ, M. ; SUMNERS, D. W. ; HARVEY, S. C.: Investigation of viral DNA packaging using molecular mechanics models. In: *Biophysical Chemistry* 101 (2002), S. 475–484
- [5] TZLIL, S. ; KINDT, J. T. ; GELBART, W. M. ; BEN-SHAUL, A.: Forces and pressures in DNA packaging and release from viral capsids. In: *Biophysical Journal* 84 (2003), Nr. 3, S. 1616–1627
- [6] PUROHIT, P. K. ; INAMDAR, M. M. ; GRAYSON, P. D. ; SQUIRES, T. M. ; KONDEV, J. ; PHILLIPS, R.: Forces during bacteriophage DNA packaging and ejection. In: *Biophysical Journal* 88 (2005), Nr. 2, S. 851–866
- [7] ARSUAGA, J. ; VAZQUEZ, M. ; MCGUIRK, P. ; TRIGUEROS, S. ; SUMNERS, D. W. ; ROCA, J.: DNA knots reveal a chiral organization of DNA in phage capsids. In: *Proceedings of the National Academy of Sciences of the United States of America* 102 (2005), Nr. 26, S. 9165–9169
- [8] SMITH, D. E. ; TANS, S. J. ; SMITH, S. B. ; GRIMES, S. ; ANDERSON, D. L. ; BUSTAMANTE, C.: The bacteriophage phi 29 portal motor can package DNA against a large internal force. In: *Nature* 413 (2001), Nr. 6857, S. 748–752
- [9] RIEMER, S. C. ; BLOOMFIELD, V. A.: Packaging of DNA in Bacteriophage Heads - Some Considerations on Energetics. In: *Biopolymers* 17 (1978), Nr. 3, S. 785–794

- [10] EARNSHAW, W. C. ; CASJENS, S. R.: DNA Packaging by the Double-Stranded DNA Bacteriophages. In: *Cell* 21 (1980), Nr. 2, S. 319–331
- [11] GABASHVILI, I. S. ; GROSBERG, A. Y.: Dynamics of Double-Stranded DNA Reptation from Bacteriophage. In: *Journal of Biomolecular Structure & Dynamics* 9 (1992), Nr. 5, S. 911–920
- [12] SMITH, S. B. ; FINZI, L. ; BUSTAMANTE, C.: Direct Mechanical Measurements of the Elasticity of Single DNA-Molecules by Using Magnetic Beads. In: *Science* 258 (1992), Nr. 5085, S. 1122–1126
- [13] SMITH, D. E. ; PERKINS, T. T. ; CHU, S.: Dynamical scaling of DNA diffusion coefficients. In: *Macromolecules* 29 (1996), Nr. 4, S. 1372–1373
- [14] CLUZEL, P. ; LEBRUN, A. ; HELLER, C. ; LAVERY, R. ; VIOVY, J. L. ; CHATENAY, D. ; CARON, F.: DNA: An extensible molecule. In: *Science* 271 (1996), Nr. 5250, S. 792–794
- [15] PERKINS, T. T. ; SMITH, D. E. ; LARSON, R. G. ; CHU, S.: Stretching of a Single Tethered Polymer in a Uniform-Flow. In: *Science* 268 (1995), Nr. 5207, S. 83–87
- [16] SMITH, D. E. ; BABCOCK, H. P. ; CHU, S.: Single-polymer dynamics in steady shear flow. In: *Science* 283 (1999), Nr. 5408, S. 1724–1727
- [17] DOYLE, P. S. ; LADOUX, B. ; VIOVY, J. L.: Dynamics of a tethered polymer in shear flow. In: *Physical Review Letters* 84 (2000), Nr. 20, S. 4769–4772
- [18] LADOUX, B. ; DOYLE, P. S.: Stretching tethered DNA chains in shear flow. In: *Europhysics Letters* 52 (2000), Nr. 5, S. 511–517
- [19] RÄDLER, J. O. ; KOLTOVER, I. ; SALDITT, T. ; SAFINYA, C. R.: Structure of DNA-cationic liposome complexes: DNA intercalation in multilamellar membranes in distinct interhelical packing regimes. In: *Science* 275 (1997), Nr. 5301, S. 810–814
- [20] ARTZNER, F. ; ZANTL, R. ; RAPP, G. ; RADLER, J. O.: Observation of a rectangular columnar phase in condensed lamellar cationic lipid-DNA complexes. In: *Physical Review Letters* 81 (1998), Nr. 22, S. 5015–5018
- [21] GROVES, J. T. ; BOXER, S. G. ; MCCONNELL, H. M.: Electric field-induced reorganization of two-component supported bilayer membranes. In: *Proceedings of the National Academy of Sciences of the United States of America* 94 (1997), Nr. 25, S. 13390–13395

-
- [22] GROVES, J. T. ; BOXER, S. G. ; MCCONNELL, H. M.: Electric field-induced critical demixing in lipid bilayer membranes. In: *Proceedings of the National Academy of Sciences of the United States of America* 95 (1998), Nr. 3, S. 935–938
- [23] KHANARIAN, G. ; CELANESE, H.: Optical properties of cyclic olefin copolymers. In: *Optical Engineering* 40 (2001), Nr. 6, S. 1024–1029
- [24] CORNELL, B. A. ; BRAACHMAKSVYTIS, V. L. B. ; KING, L. G. ; OSMAN, P. D. J. ; RAGUSE, B. ; WIECZOREK, L. ; PACE, R. J.: A biosensor that uses ion-channel switches. In: *Nature* 387 (1997), Nr. 6633, S. 580–583
- [25] SACKMANN, E.: Supported membranes: Scientific and practical applications. In: *Science* 271 (1996), Nr. 5245, S. 43–48
- [26] JOHNSON, S. J. ; BAYERL, T. M. ; MCDERMOTT, D. C. ; ADAM, G. W. ; RENNIE, A. R. ; THOMAS, R. K. ; SACKMANN, E.: Structure of an Adsorbed Dimyristoylphosphatidylcholine Bilayer Measured with Specular Reflection of Neutrons. In: *Biophysical Journal* 59 (1991), Nr. 2, S. 289–294
- [27] KOENIG, B. W. ; KRUGER, S. ; ORTS, W. J. ; MAJKRZAK, C. F. ; BERK, N. F. ; SILVERTON, J. V. ; GAWRISCH, K.: Neutron reflectivity and atomic force microscopy studies of a lipid bilayer in water adsorbed to the surface of a silicon single crystal. In: *Langmuir* 12 (1996), Nr. 5, S. 1343–1350
- [28] FRAGNETO, G. ; BELLET-AMALRIC, E. ; CHARITAT, T. ; DUBOS, P. ; GRANER, F. ; PERINO-GALICE, L.: Neutron and X-Ray reflectivity studies at solid-liquid interfaces: the interaction of a peptide with model membranes. In: *Physica B* 276 (2000), S. 501–502
- [29] KRUEGER, S. ; MEUSE, C. W. ; MAJKRZAK, C. F. ; DURA, J. A. ; BERK, N. F. ; TAREK, M. ; PLANT, A. L.: Investigation of hybrid bilayer membranes with neutron reflectometry: Probing the interactions of melittin. In: *Langmuir* 17 (2001), Nr. 2, S. 511–521
- [30] MENNICKE, U. ; SALDITT, T.: Preparation of solid-supported lipid bilayers by spin-coating. In: *Langmuir* 18 (2002), Nr. 21, S. 8172–8177
- [31] BURGESS, I. ; LI, M. ; HORSWELL, S. L. ; SZYMANSKI, G. ; LIPKOWSKI, J. ; MAJEWSKI, J. ; SATIJA, S.: Electric field-driven transformations of a supported model biological membrane - An electrochemical and neutron reflectivity study. In: *Biophysical Journal* 86 (2004), Nr. 3, S. 1763–1776
- [32] YAMAZAKI, V. ; SIRENKO, O. ; SCHAFER, R. J. ; GROVES, J. T.: Lipid mobility and molecular binding in fluid lipid membranes. In: *Journal of the American Chemical Society* 127 (2005), Nr. 9, S. 2826–2827

- [33] LENZ, P. ; AJO-FRANKLIN, C. M. ; BOXER, S. G.: Patterned supported lipid bilayers and monolayers on poly(dimethylsiloxane). In: *Langmuir* 20 (2004), Nr. 25, S. 11092–11099
- [34] ELLIOTT, J. T. ; BURDEN, D. L. ; WOODWARD, J. T. ; SEHGAL, A. ; DOUGLAS, J. F.: Phospholipid monolayers supported on spun cast polystyrene films. In: *Langmuir* 19 (2003), Nr. 6, S. 2275–2283
- [35] RETZINGER, G. S. ; MEREDITH, S. C. ; LAU, S. H. ; KAISER, E. T. ; KEZDY, F. J.: A Method for Probing the Affinity of Peptides for Amphiphilic Surfaces. In: *Analytical Biochemistry* 150 (1985), Nr. 1, S. 131–140
- [36] HAMLEY, I. W.: *Introduction to Soft Matter*. Chichester New York Weinheim Brisbane Singapore Toronto : John Wiley &Son, Ltd, 2000
- [37] PARRA, I. ; WINDLE, B.: High-Resolution Visual Mapping of Stretched DNA by Fluorescent Hybridization. In: *Nature Genetics* 5 (1993), Nr. 1, S. 17–21
- [38] SCHWARTZ, D. C. ; LI, X. J. ; HERNANDEZ, L. I. ; RAMNARAIN, S. P. ; HUFF, E. J. ; WANG, Y. K.: Ordered Restriction Maps of *Saccharomyces-Cerevisiae* Chromosomes Constructed by Optical Mapping. In: *Science* 262 (1993), Nr. 5130, S. 110–114
- [39] SAMAD, A. H. ; CAI, W. W. ; HU, X. H. ; IRVIN, B. ; JING, J. P. ; REED, J. ; MENG, X. ; HUANG, J. ; HUFF, E. ; PORTER, B. ; SHENKAR, A. ; ANANTHARAMAN, T. ; MISHRA, B. ; CLARKE, V. ; DIMALANTA, E. ; EDINGTON, J. ; HIORT, C. ; RABBAH, R. ; SKIADA, J. ; SCHWARTZ, D. C.: Mapping the Genome One Molecule at a Time - Optical Mapping. In: *Nature* 378 (1995), Nr. 6556, S. 516–517
- [40] SCHWARTZ, D. C. ; SAMAD, A.: Optical mapping approaches to molecular genomics. In: *Current Opinion in Biotechnology* 8 (1997), Nr. 1, S. 70–74
- [41] LIN, J. Y. ; QI, R. ; ASTON, C. ; JING, J. P. ; ANANTHARAMAN, T. S. ; MISHRA, B. ; WHITE, O. ; DALY, M. J. ; MINTON, K. W. ; VENTER, J. C. ; SCHWARTZ, D. C.: Whole-genome shotgun optical mapping of *Deinococcus radiodurans*. In: *Science* 285 (1999), Nr. 5433, S. 1558–1562
- [42] ALLEMAND, J. F. ; BENSIMON, D. ; CROQUETTE, V.: Stretching DNA and RNA to probe their interactions with proteins. In: *Current Opinion in Structural Biology* 13 (2003), Nr. 3, S. 266–274
- [43] BUSTAMANTE, C. ; MARKO, J. F. ; SIGGIA, E. D. ; SMITH, S.: Entropic Elasticity of Lambda-Phage DNA. In: *Science* 265 (1994), Nr. 5178, S. 1599–1600

-
- [44] KRATKY, O. ; POROD, G.: Rontgenuntersuchung Geloster Fadenmolekule. In: *Recueil Des Travaux Chimiques Des Pays-Bas-Journal of the Royal Netherlands Chemical Society* 68 (1949), Nr. 12, S. 1106–1122
- [45] MARKO, J. F. ; SIGGIA, E. D.: Stretching DNA. In: *Macromolecules* 28 (1995), Nr. 26, S. 8759–8770
- [46] ODIJK, T.: Stiff Chains and Filaments under Tension. In: *Macromolecules* 28 (1995), Nr. 20, S. 7016–7018
- [47] BAUMANN, C. G. ; SMITH, S. B. ; BLOOMFIELD, V. A. ; BUSTAMANTE, C.: Ionic effects on the elasticity of single DNA molecules. In: *Proceedings of the National Academy of Sciences of the United States of America* 94 (1997), Nr. 12, S. 6185–6190
- [48] WANG, M. D. ; YIN, H. ; LANDICK, R. ; GELLES, J. ; BLOCK, S. M.: Stretching DNA with optical tweezers. In: *Biophysical Journal* 72 (1997), Nr. 3, S. 1335–1346
- [49] RIEF, M. ; CLAUSEN-SCHAUMANN, H. ; GAUB, H. E.: Sequence-dependent mechanics of single DNA molecules. In: *Nature Structural Biology* 6 (1999), Nr. 4, S. 346–349
- [50] WILLIAMS, M. C. ; WENNER, J. R. ; ROUZINA, L. ; BLOOMFIELD, V. A.: Effect of on on the overstretching transition of double-stranded DNA: Evidence of force-induced DNA melting. In: *Biophysical Journal* 80 (2001), Nr. 2, S. 874–881
- [51] BUSTAMANTE, C. ; SMITH, S. B. ; LIPHARDT, J. ; SMITH, D.: Single-molecule studies of DNA mechanics. In: *Current Opinion in Structural Biology* 10 (2000), Nr. 3, S. 279–285
- [52] MAIER, B. ; SEIFERT, U. ; RADLER, J. O.: Elastic response of DNA to external electric fields in two dimensions. In: *Europhysics Letters* 60 (2002), Nr. 4, S. 622–628
- [53] BENSIMON, A. ; SIMON, A. ; CHIFFAUDEL, A. ; CROQUETTE, V. ; HESLOT, F. ; BENSIMON, D.: Alignment and Sensitive Detection of DNA by a Moving Interface. In: *Science* 265 (1994), Nr. 5181, S. 2096–2098
- [54] BENSIMON, D. ; SIMON, A. J. ; CROQUETTE, V. ; BENSIMON, A.: Stretching DNA with a Receding Meniscus - Experiments and Models. In: *Physical Review Letters* 74 (1995), Nr. 23, S. 4754–4757
- [55] WANG, W. N. ; LIN, J. Y. ; SCHWARTZ, D. C.: Scanning force microscopy of DNA molecules elongated by convective fluid flow in an evaporating droplet. In: *Biophysical Journal* 75 (1998), Nr. 1, S. 513–520

- [56] TEGENFELDT, J. O. ; PRINZ, C. ; CAO, H. ; CHOU, S. ; REISNER, W. W. ; RIEHN, R. ; WANG, Y. M. ; COX, E. C. ; STURM, J. C. ; SILBERZAN, P. ; AUSTIN, R. H.: The dynamics of genomic-length DNA molecules in 100-nm channels. In: *Proceedings of the National Academy of Sciences of the United States of America* 101 (2004), Nr. 30, S. 10979–10983
- [57] DE GENNES, P. G.: *Scaling Concepts in Polymer Physics*. New York : Cornell University Press, 1979
- [58] ODIJK, T.: On the Statistics and Dynamics of Confined or Entangled Stiff Polymers. In: *Macromolecules* 16 (1983), Nr. 8, S. 1340–1344
- [59] DIJKSTRA, M. ; FRENKEL, D. ; LEKKERKERKER, H. N. W.: Confinement Free-Energy of Semiflexible Polymers. In: *Physica A* 193 (1993), Nr. 3-4, S. 374–393
- [60] REISNER, W. ; MORTON, K. J. ; RIEHN, R. ; WANG, Y. M. ; YU, Z. N. ; ROSEN, M. ; STURM, J. C. ; CHOU, S. Y. ; FREY, E. ; AUSTIN, R. H.: Statics and dynamics of single DNA molecules confined in nanochannels. In: *Physical Review Letters* 94 (2005), Nr. 19
- [61] GUO, L. J. ; CHENG, X. ; CHOU, C. F.: Fabrication of size-controllable nanofluidic channels by nanoimprinting and its application for DNA stretching. In: *Nano Letters* 4 (2004), Nr. 1, S. 69–73
- [62] STRYER, L.: *Biochemie*. 4. Heidelberg, Berlin, Oxford : Spektrum Akademischer Verlag, 1985
- [63] LIPOWSKY, R. (Hrsg.) ; SACKMANN, E. (Hrsg.): *Handbook of Biological Physics*. Bd. 1 A: *Structure and Dynamics of Membranes*. Amsterdam, Lausanne, New York, Oxford, Shannon, Tokyo : Elsevier, 1995
- [64] SINGER, S. J. ; NICOLSON, G. L.: Fluid Mosaic Model of the Structure of Cell-Membranes. In: *Science* 175 (1972), Nr. 4023, S. 720
- [65] HUANG, C. H. ; LI, S. S.: Calorimetric and molecular mechanics studies of the thermotropic phase behavior of membrane phospholipids. In: *Biochimica Et Biophysica Acta-Reviews on Biomembranes* 1422 (1999), Nr. 3, S. 273–307
- [66] PLANT, A. L.: Supported hybrid bilayer membranes as rugged cell membrane mimics. In: *Langmuir* 15 (1999), Nr. 15, S. 5128–5135
- [67] SALDITT, T.: Thermal fluctuations and stability of solid-supported lipid membranes. In: *Journal of Physics-Condensed Matter* 17 (2005), Nr. 6, S. R287–R314

-
- [68] TRISTRAM-NAGLE, S. ; PETRACHE, H. I. ; NAGLE, J. F.: Structure and interactions of fully hydrated dioleoylphosphatidylcholine bilayers. In: *Biophysical Journal* 75 (1998), Nr. 2, S. 917–925
- [69] KERN, W. ; PUOTINEN, D. A.: Cleaning Solutions Based on Hydrogen Peroxide for Use in Silicon Semiconductor Technology. In: *Rca Review* 31 (1970), Nr. 2, S. 187
- [70] REICH, C. ; HOCHREIN, M. ; KRAUSE, B. ; NICKEL, B.: A Microfluidic Chamber for X-ray Reflectivity at the Solid-Liquid Interface. In: *Review of Scientific Instruments* 76 (2005), S. 095103
- [71] POMPE, T. ; FERY, A. ; HERMINGHAUS, S. ; KRIELE, A. ; LORENZ, H. ; KOTTHAUS, J. P.: Submicron contact printing on silicon using stamp pads. In: *Langmuir* 15 (1999), Nr. 7, S. 2398–2401
- [72] NIELSEN, T. ; NILSSON, D. ; BUNDGAARD, F. ; SHI, P. ; SZABO, P. ; GESCHKE, O. ; KRISTENSEN, A.: Nanoimprint lithography in the cyclic olefin copolymer, Topas((R)), a highly ultraviolet-transparent and chemically resistant thermoplast. In: *Journal of Vacuum Science and Technology B* 22 (2004), Nr. 4, S. 1770–1775
- [73] MONKKONEN, K. ; LAUTANEN, J. ; KETTUNEN, V. ; LEPPANEN, V. P. ; PAKKANEN, T. T. ; JAASKELAINEN, T.: Replication of an antireflecting element in COC plastics using a hot embossing technique. In: *Journal of Materials Chemistry* 10 (2000), Nr. 12, S. 2634–2636
- [74] BARENHOLZ, Y. ; GIBBES, D. ; LITMAN, B. J. ; GOLL, J. ; THOMPSON, T. E. ; CARLSON, F. D.: Simple Method for Preparation of Homogeneous Phospholipid Vesicles. In: *Biochemistry* 16 (1977), Nr. 12, S. 2806–2810
- [75] BONHIVERS, M. ; GHAZI, A. ; BOULANGER, P. ; LETELLIER, L.: FhuA, a transporter of the *Escherichia coli* outer membrane, is converted into a channel upon binding of bacteriophage T5. In: *Embo Journal* 15 (1996), Nr. 8, S. 1850–1856
- [76] BOULANGER, P. ; LEMAIRE, M. ; BONHIVERS, M. ; DUBOIS, S. ; DESMADRIL, M. ; LETELLIER, L.: Purification and structural and functional characterization of FhuA, a transporter of the *Escherichia coli* outer membrane. In: *Biochemistry* 35 (1996), Nr. 45, S. 14216–14224
- [77] DIETRICH, C. ; MERKEL, R. ; TAMPE, R.: Diffusion Measurement of Fluorescence-Labeled Amphiphilic Molecules with a Standard Fluorescence Microscope. In: *Biophysical Journal* 72 (1997), S. 1701–1710
- [78] AXELROD, D. ; KOPPEL, D. E. ; SCHLESSINGER, J. ; ELSON, E. ; WEBB, W. W.: Mobility measurements by analysis of fluorescence photobleaching recovery kinetics. In: *Biophysical Journal* 16 (1976), S. 1055–1069

- [79] SOUMPASIS, D. M.: Theoretical analysis of fluorescence photobleaching recovery experiments. In: *Biophysical Journal* 41 (1983), S. 95–97
- [80] PARRATT, L. G.: Surface Studies of Solids by Total Reflection of X-Rays. In: *Physical Review* 95 (1954), Nr. 2, S. 359–369
- [81] BALTER, M.: Virology - Evolution on life's fringes. In: *Science* 289 (2000), Nr. 5486, S. 1866–1867
- [82] CASJENS, S. ; HENDRIX, R.W.: Control mechanisms in dsDNA bacteriophage assembly. In: CALENDAR, R. (Hrsg.): *The Bacteriophages* Bd. 1. New York : Plenum Press, 1988, S. 15–90
- [83] LETELLIER, L. ; BOULANGER, P. ; DE FRUTOS, M. ; JACQUOT, P.: Channeling phage DNA through membranes: from in vivo to in vitro. In: *Research in Microbiology* 154 (2003), Nr. 4, S. 283–287
- [84] LETELLIER, L. ; BOULANGER, P. ; PLANCON, L. ; JACQUOT, P. ; SANTAMARIA, M.: Main features on tailed phage, host recognition and DNA uptake. In: *Frontiers in Bioscience* 9 (2004), S. 1228–1239
- [85] LAMBERT, O. ; PLANCON, L. ; RIGAUD, J. L. ; LETELLIER, L.: Protein-mediated DNA transfer into liposomes. In: *Molecular Microbiology* 30 (1998), Nr. 4, S. 761–765
- [86] LAMBERT, O. ; LETELLIER, L. ; GELBART, W. M. ; RIGAUD, J. L.: DNA delivery by phage as a strategy for encapsulating toroidal condensates of arbitrary size into liposomes. In: *Proceedings of the National Academy of Sciences of the United States of America* 97 (2000), Nr. 13, S. 7248–7253
- [87] GURRIERI, S. ; WELLS, K. S. ; JOHNSON, I. D. ; BUSTAMANTE, C.: Direct visualization of individual DNA molecules by fluorescence microscopy: Characterization of the factors affecting signal/background and optimization of imaging conditions using YOYO. In: *Analytical Biochemistry* 249 (1997), Nr. 1, S. 44–53
- [88] STRICK, T. R. ; ALLEMAND, J. F. ; BENSIMON, D. ; CROQUETTE, V.: Stress-induced structural transitions in DNA and proteins. In: *Annual Review of Biophysics and Biomolecular Structure* 29 (2000), S. 523–543
- [89] SCHEIBLE, P. P. ; RHOADES, E. A. ; RHOADES, M.: Localization of Single-Chain Interruptions in Bacteriophage-T5 DNA .1. Electron-Microscopic Studies. In: *Journal of Virology* 23 (1977), Nr. 3, S. 725–736
- [90] MCCORQUODALE, J.D. ; WARNER, H.R.: Bacteriophage T5 and Related Phages. In: CALENDAR, R. (Hrsg.): *The Viruses* Bd. 1. New York : Plenum Press, 1988, S. 439–476

-
- [91] LABEDAN, B. ; CROCHET, M. ; LEGAULTD.J ; STEVENS, B. J.: Location of First Step Transfer Fragment and Single-Strand Interruptions in T5sto Bacteriophage DNA. In: *Journal of Molecular Biology* 75 (1973), Nr. 2, S. 213
- [92] SAIGO, K.: New Bacteriophage-T5 Particle with a DNA Lacking Terminal Repe-tition at Right-Hand End. In: *Journal of Molecular Biology* 107 (1976), Nr. 3, S. 369–378
- [93] SHAW, A. R. ; DAVISON, J.: Polarized Injection of the Bacteriophage-T5 Chro-mosome. In: *Journal of Virology* 30 (1979), Nr. 3, S. 933–935
- [94] DE FRUTOS, M. ; LETELLIER, L. ; RASPAUD, E.: DNA ejection from bacterio-phage T5: Analysis of the kinetics and energetics. In: *Biophysical Journal* 88 (2005), Nr. 2, S. 1364–1370
- [95] NICHOLS, B. P. ; DONELSON, J. E.: Sequence-Analysis of Nicks and Termini of Bacteriophage-T5 DNA. In: *Journal of Virology* 22 (1977), Nr. 2, S. 520–526
- [96] LE CAM, E. ; FACK, F. ; MENISSIERDEMURCIA, J. ; COGNET, J. A. H. ; BARBIN, A. ; SARANTOGLOU, V. ; REVET, B. ; DELAIN, E. ; DEMURCIA, G.: Conformational-Analysis of a 139 Base-Pair DNA Fragment Containing a Single-Stranded Break and Its Interaction with Human Poly(Adp-Ribose) Polymerase. In: *Journal of Molecular Biology* 235 (1994), Nr. 3, S. 1062–1071
- [97] EVILEVITCH, A. ; LAVELLE, L. ; KNOBLER, C. M. ; RASPAUD, E. ; GELBART, W. M.: Osmotic pressure inhibition of DNA ejection from phage. In: *Proceedings of the National Academy of Sciences of the United States of America* 100 (2003), Nr. 16, S. 9292–9295
- [98] ROGERS, S. G. ; GODWIN, E. A. ; SHINOSKY, E. S. ; RHOADES, M.: Interruption-Deficient Mutants of Bacteriophage-T5 .1. Isolation and General Properties. In: *Journal of Virology* 29 (1979), Nr. 2, S. 716–725
- [99] FRAGNETO, G. ; CHARITAT, T. ; BELLET-AMALRIC, E. ; CUBITT, R. ; GRANER, F.: Swelling of phospholipid floating bilayers: The effect of chain length. In: *Langmuir* 19 (2003), Nr. 19, S. 7695–7702
- [100] VOGEL, M. ; MUNSTER, C. ; FENZL, W. ; SALDITT, T.: Thermal unbinding of highly oriented phospholipid membranes. In: *Physical Review Letters* 84 (2000), Nr. 2, S. 390–393
- [101] ZIEGLER, C. ; GOPEL, W.: Biosensor development. In: *Current Opinion in Chemical Biology* 2 (1998), Nr. 5, S. 585–591

- [102] MAIER, B. ; RÄDLER, J. O.: Conformation and self-diffusion of single DNA molecules confined to two dimensions. In: *Physical Review Letters* 82 (1999), Nr. 9, S. 1911–1914
- [103] MAIER, B. ; RÄDLER, J. O.: DNA on fluid membranes: A model polymer in two dimensions. In: *Macromolecules* 33 (2000), Nr. 19, S. 7185–7194
- [104] OLSON, D. J. ; JOHNSON, J. M. ; PATEL, P. D. ; SHAQFEH, E. S. G. ; BOXER, S. G. ; FULLER, G. G.: Electrophoresis of DNA adsorbed to a cationic supported bilayer. In: *Langmuir* 17 (2001), Nr. 23, S. 7396–7401
- [105] CREMER, P. S. ; BOXER, S. G.: Formation and spreading of lipid bilayers on planar glass supports. In: *Journal of Physical Chemistry B* 103 (1999), Nr. 13, S. 2554–2559
- [106] KALB, E. ; FREY, S. ; TAMM, L. K.: Formation of Supported Planar Bilayers by Fusion of Vesicles to Supported Phospholipid Monolayers. In: *Biochimica Et Biophysica Acta* 1103 (1992), Nr. 2, S. 307–316
- [107] PUU, G. ; GUSTAFSON, I.: Planar lipid bilayers on solid supports from liposomes - factors of importance for kinetics and stability. In: *Biochimica Et Biophysica Acta-Biomembranes* 1327 (1997), Nr. 2, S. 149–161
- [108] REIMHULT, E. ; HOOK, F. ; KASEMO, B.: Temperature dependence of formation of a supported phospholipid bilayer from vesicles on SiO₂. In: *Physical Review E* 66 (2002), Nr. 5
- [109] MOU, J. X. ; YANG, J. ; SHAO, Z. F.: Atomic-Force Microscopy of Cholera-Toxin B-Oligomers Bound to Bilayers of Biologically Relevant Lipids. In: *Journal of Molecular Biology* 248 (1995), Nr. 3, S. 507–512
- [110] ROHR, T. ; OGLETTREE, D. F. ; SVEC, F. ; FRECHET, J. M. J.: Surface functionalization of thermoplastic polymers for the fabrication of microfluidic devices by photoinitiated grafting. In: *Advanced Functional Materials* 13 (2003), Nr. 4, S. 264–270
- [111] GENEROSI, J. ; CASTELLANO, C. ; POZZI, D. ; CASTELLANO, A. C. ; FELICI, R. ; NATALI, F. ; FRAGNETO, G.: X-ray and neutron reflectivity study of solid-supported lipid membranes prepared by spin coating. In: *Journal of Applied Physics* 96 (2004), Nr. 11, S. 6839–6844
- [112] CLAUSEN-SCHAUMANN, H. ; GAUB, H. E.: DNA adsorption to laterally structured charged lipid membranes. In: *Langmuir* 15 (1999), Nr. 23, S. 8246–8251

-
- [113] CAMPBELL, R. B. ; BALASUBRAMANIAN, S. V. ; STRAUBINGER, R. M.: Phospholipid-cationic lipid interactions: influences on membrane and vesicle properties. In: *Biochimica Et Biophysica Acta-Biomembranes* 1512 (2001), Nr. 1, S. 27–39
- [114] SYMIETZ, C. ; SCHNEIDER, M. ; BREZESINSKI, G. ; MOHWALD, H.: DNA alignment at cationic lipid monolayers at the air/water interface. In: *Macromolecules* 37 (2004), Nr. 10, S. 3865–3873
- [115] BRIAN, Adrienne A. ; MCCONNELL, Harden M.: Allogeneic stimulation of cytotoxic T cells by supported planar membranes. In: *Proceedings of the National Academy of Science* 81 (1984), S. 6159–6163
- [116] MILLER, C. ; CUENDET, P. ; GRÄTZEL, M.: K⁺ sensitive bilayer supporting electrodes. In: *Journal of Electroanalytical Chemistry* 278 (1990), S. 175–192
- [117] KÖCHY, T. ; BAYERL, T. M.: Lateral Diffusion-Coefficients of Phospholipids in Spherical Bilayers on a Solid Support Measured by H-2-Nuclear-Magnetic-Resonance Relaxation. In: *Physical Review E* 47 (1993), Nr. 3, S. 2109–2116
- [118] TAMM, L. K. ; MCCONNELL, H. M.: Supported Phospholipid-Bilayers. In: *Biophysical Journal* 47 (1985), Nr. 1, S. 105–113
- [119] HENKE, B. L. ; GULLIKSON, E. M. ; DAVIS, J. C.: X-Ray Interactions - Photoabsorption, Scattering, Transmission, and Reflection at E=50-30,000 Ev, Z=1-92. In: *Atomic Data and Nuclear Data Tables* 54 (1993), Nr. 2, S. 181–342
- [120] BARRY, J. A. ; GAWRISCH, K.: Direct Nmr Evidence for Ethanol Binding to the Lipid-Water Interface of Phospholipid-Bilayers. In: *Biochemistry* 33 (1994), Nr. 26, S. 8082–8088. – BIOCHEMISTRY-USA
- [121] BARRY, J. A. ; GAWRISCH, K.: Effects of Ethanol on Lipid Bilayers Containing Cholesterol, Gangliosides, and Sphingomyelin. In: *Biochemistry* 34 (1995), Nr. 27, S. 8852–8860. – BIOCHEMISTRY-USA
- [122] LIU, Y. F. ; NAGLE, J. F.: Diffuse scattering provides material parameters and electron density profiles of biomembranes. In: *Physical Review E* 69 (2004), Nr. 4. – Part 1
- [123] SCHALKE, M. ; LOSCHE, M.: Structural models of lipid surface monolayers from X-ray and neutron reflectivity measurements. In: *Advances in Colloid and Interface Science* 88 (2000), Nr. 1-2, S. 243–274. – Sp. Iss. SI
- [124] GLIOZZI, A. ; RELINI, A. ; CHONG, P. L. G.: Structure and permeability properties of biomimetic membranes of bolaform archaeal tetraether lipids. In: *Journal of Membrane Science* 206 (2002), Nr. 1-2, S. 131–147. – Sp. Iss. SI

- [125] MOU, J. X. ; YANG, J. ; HUANG, C. ; SHAO, Z. F.: Alcohol Induces Interdigitated Domains in Unilamellar Phosphatidylcholine Bilayers. In: *Biochemistry* 33 (1994), Nr. 33, S. 9981–9985
- [126] HOLLINSHEAD, C. M. ; HANNA, M. ; BARLOW, D. J. ; DE BIASI, V. ; BUCKNALL, D. G. ; CAMILLERI, P. ; HUTT, A. J. ; LAWRENCE, M. J. ; LU, J. R. ; SU, T. J.: Neutron reflection from a dimyristoylphosphatidylcholine monolayer adsorbed on a hydrophobised silicon support. In: *Biochimica Et Biophysica Acta-Biomembranes* 1511 (2001), Nr. 1, S. 49–59
- [127] RÄDLER, U. ; KAHL, V.: 2005. – Ibidi GmbH, Munich, private communications
- [128] HOCHREIN, M. ; LEIERSEDER, J. ; RÄDLER, J. ; GOLUBOVIC, L.: DNA Localization and Coil Stretching on Periodically Micro-structured Lipid Membranes. In: *Physical Review Letters* . – accepted
- [129] PERINO-GALLICE, L. ; FRAGNETO, G. ; MENNICKE, U. ; SALDITT, T. ; RIEUTORD, F.: Dewetting of solid-supported multilamellar lipid layers. In: *European Physical Journal E* 8 (2002), Nr. 3, S. 275–282
- [130] SPANGENBERG, T. ; DE MELLO, N. F. ; CRECZYNSKI-PASA, T. B. ; PASA, A. A. ; NIEHUS, H.: AFM in-situ characterization of supported phospholipid layers formed by solution spreading. In: *Physica Status Solidi a-Applied Research* 201 (2004), Nr. 5, S. 857–860
- [131] CHARITAT, T. ; BELLET-AMALRIC, E. ; FRAGNETO, G. ; GRANER, F.: Adsorbed and free lipid bilayers at the solid-liquid interface. In: *European Physical Journal B* 8 (1999), Nr. 4, S. 583–593
- [132] MERKEL, R. ; SACKMANN, E. ; EVANS, E.: Molecular Friction and Epitactic Coupling between Monolayers in Supported Bilayers. In: *Journal De Physique* 50 (1989), Nr. 12, S. 1535–1555
- [133] MILLER, CE ; MAJEWSKI, J ; GOG, T ; KUHL, T L.: Characterization of biological thin films at the solid-liquid interface by x-ray reflectivity. In: *Physical Review Letters* 94 (2005)
- [134] GOLUBOVIC, L.: 2002. – private communications
- [135] MULLINS, W. W.: Theory of Thermal Grooving. In: *Journal of Applied Physics* 28 (1957), Nr. 3, S. 333–339
- [136] BURKHARDT, T. W.: Free energy of a semiflexible polymer in a tube and statistics of a randomly-accelerated particle. In: *Journal of Physics a-Mathematical and General* 30 (1997), Nr. 7, S. L167–L172

- [137] LANDAU, L.D ; LIFSHITS, E. M.: *Statistical Physics*. Oxford : Pergamon, 1969

Lebenslauf

Marion Birgit Hochrein

Geburtstag	10.02.1976
Geburtsort	München
Familienstand	ledig
1996	Abitur, Note: 1.3
11/1996 - 10/2001	Studium Diplom Physik an der Technischen Universität München
10/2000 - 10/2001	Diplomarbeit bei Professor Dr. E. Sackmann Titel: "Immobilization of Native Cell Membranes on Soft Polymer Cushions"
11/2001	Diplom in Allgemeiner Physik, Note: 1.2 (mit Auszeichnung)
11/2001 - 12/2001	wissenschaftliche Angestellte and der Technischen Universität München
01/2002 - 11/2005	Promotion an der Ludwigs-Maximilians-Universiät München bei Professor Dr. J. O. Rädler Titel: "From Single DNA Molecules to an Entire Virus: an Investigation with Quantitative Fluorescence Microscopy and X-Ray Reflectivity"

Publications

MANGENOT, S. ; HOCHREIN, M. B. ; RÄDLER, J. O. ; LETELLIER, L.: Real-time imaging of DNA ejection from single phage particles In: *Current Biology* 15 (2005), Nr. 5, S. 430–435

REICH, C. D. ; HOCHREIN, M. B. ; KRAUSE, B. ; NICKEL, B.: A Microfluidic Chamber for X-ray Reflectivity at the Solid-Liquid Interface In: *Review of Scientific Instruments* 76 (2005), 095103

HOCHREIN, M. B. ; REICH, C. ; KRAUSE, B. ; RÄDLER, J. O. ; NICKEL, B.: Structure and Mobility of Lipid Membranes on a Thermoplastic Substrate In: *Langmuir*, in press

HOCHREIN, M. B. ; LEIERSEDER, J. ; GOLUBOVIC, L. ; RÄDLER, J. O.: DNA Localization and Coil Stretching on Periodically Micro-structured Lipid Membranes In: *Physical Review Letters*, accepted